

NUMERICAL MODELING AND OPTIMIZATION OF HgCdTe INFRARED
PHOTODETECTORS FOR THERMAL IMAGING

A THESIS SUBMITTED TO
THE GRADUATE SCHOOL OF NATURAL AND APPLIED SCIENCES
OF
MIDDLE EAST TECHNICAL UNIVERSITY

BY

HASAN KOÇER

IN PARTIAL FULFILLMENT OF THE REQUIREMENTS
FOR
THE DEGREE OF DOCTOR OF PHILOSOPHY
IN
ELECTRICAL AND ELECTRONICS ENGINEERING

MARCH 2011

Approval of the thesis:

**NUMERICAL MODELING AND OPTIMIZATION OF HgCdTe INFRARED
PHOTODETECTORS FOR THERMAL IMAGING**

submitted by **HASAN KOÇER** in partial fulfillment of the requirements for the
degree of **Doctor of Philosophy in Electrical and Electronics Engineering**
Department, Middle East Technical University by,

Prof. Dr. Canan Özgen
Dean, Graduate School of **Natural and Applied Sciences**

Prof. Dr. İsmet Erkmén
Head of Department, **Electrical and Electronics Engineering**

Prof. Dr. Cengiz Beşikci
Supervisor, **Electrical and Electronics Engineering Dept., METU**

Examining Committee Members:

Prof. Dr. Tayfun Akın
Electrical and Electronics Engineering Dept., METU

Prof. Dr. Cengiz Beşikci
Electrical and Electronics Engineering Dept., METU

Prof. Dr. Ekmel Özbay
Electrical and Electronics Engineering Dept., Bilkent University

Prof. Dr. Mehmet Parlak
Physics Dept., METU

Assoc. Prof. Dr. Haluk Kùlah
Electrical and Electronics Engineering Dept., METU

Date: 17.03.2011

I hereby declare that all information in this document has been obtained and presented in accordance with academic rules and ethical conduct. I also declare that, as required by these rules and conduct, I have fully cited and referenced all material and results that are not original to this work.

Name, Last Name: HASAN KOÇER

Signature :

ABSTRACT

NUMERICAL MODELING AND OPTIMIZATION OF HgCdTe INFRARED PHOTODETECTORS FOR THERMAL IMAGING

KOÇER, Hasan

Ph.D., Department of Electrical and Electronics Engineering

Supervisor: Prof. Dr. Cengiz BEŞİKÇİ

March 2011, 101 pages

This thesis presents a detailed investigation of the performance limiting factors of long wavelength infrared (LWIR) and very long wavelength infrared (VLWIR) p on n HgCdTe detectors through numerical simulations at 77 K incorporating all considerable generation-recombination mechanisms including trap assisted tunneling (TAT), Shockley-Read-Hall (SRH), Auger and radiative processes. Numerical simulations under dark and illuminated conditions were performed with different absorber layer thicknesses, material compositions (cut-off wavelengths), trap density, and trap energy level. The results identify the relative strength of the dark current generation mechanisms by numerically extracting the contribution of each G-R mechanism on the detector characteristics with various cut off wavelengths (λ_c) and practically achievable material parameters.

While the provided information can be used as a guide for optimizing the device processing conditions and detector structure, it also enlightens the importance of various intrinsic mechanisms on the detector sensitivity.

The results show that the dominant sensitivity degrading trap level depends on the detector cut-off wavelength being $\sim 0.7E_g$ for LWIR HgCdTe sensors ($\lambda_c \sim 10 \mu\text{m}$) instead of $0.5E_g$ which is generally believed to be the most efficient R-G level. TAT related $1/f$ noise dominates the sensor noise even under small reverse bias voltages at a trap density as low as $1 \times 10^{14} \text{ cm}^{-3}$ for sensors with $\lambda_c > 11 \mu\text{m}$. Considering the fact that trap densities below this level are rarely reported for HgCdTe material, exceptionally trap-free material is required to achieve desirable imaging performance with these sensors.

Simulation results show that Auger mechanism has twofold effect on the sensitivity of the sensor by increasing the dark current and decreasing the photo current of the detector.

As to our knowledge, this work is one of the most comprehensive simulation based investigations of the HgCdTe detector performance providing important results that can be used as a guide for optimization of the detector performance in order to meet the demanding requirements of the third generation thermal imagers.

Keywords: HgCdTe, photodetector, numerical simulation, TAT

ÖZ

TERMAL GÖRÜNTÜLEME AMAÇLI HgCdTe KIZILÖTESİ FOTODEDEKTÖRLERİN SAYISAL MODELLEME VE OPTİMİZASYONU

KOÇER, Hasan

Doktora, Elektrik Elektronik Mühendisliği Bölümü

Tez Danışmanı: Prof. Dr. Cengiz BEŞİKCİ

Mart 2011, 101 sayfa

Bu tez çalışmasında, termal görüntülemede kullanılan uzun dalga (LWIR) ve çok uzun dalga (VLWIR) kızılötesi bölgede çalışan p-n HgCdTe (Civa Kadmiyum Tellürüt) kızılötesi dedektörlerin sayısal simülasyonları yapılarak 77 K sıcaklıkta performansına etki eden parametreler çok yönlü olarak araştırılmaktadır. Simülasyonlarda Auger, Shockley-Read-Hall (SRH), ışıma ve tuzak yardımıyla tünelleme (TAT) mekanizmaları etkileşimli olarak kullanılmaktadır. Sayısal simülasyonlar karanlık ve kızılötesi ışıma altında yapılmaktadır. Bu sayede, dedektörün aktif bölge kalınlığı, malzeme kompozisyonu, kesim dalga boyu, tuzak yoğunluğu ve tuzak enerji seviyesindeki değişimlerin sensor performansına olan etkileri detaylı olarak gözlenmektedir. Sayısal simülasyon sonucu elde edilen sonuçlar, karanlık akım oluşturan G-R mekanizmalarının bağlı güçlerinin kesim dalga boyu ve pratik olarak erişilebilen malzeme parametrelerine göre dedektör karakteristiğine olan etkilerini açıklamaktadır.

Elde edilen bilgi, dedektör tasarım ve üretim prosesinin optimizasyonunda kullanılabilir. Ayrıca, sözkonusu bilgi dedektör hassasiyetine yönelik içsel mekanizmaların önemini de aydınlatmaktadır.

LWIR HgCdTe sensörler ($\lambda_c \sim 10 \mu\text{m}$) için dedektör hassasiyetini en çok bozan tuzak seviyesinin orta bandta ($0.5E_g$) olduğuna inanılmasına rağmen, bu tez çalışmasının simülasyon sonuçlarıyla valans banttan yaklaşık $0.7E_g$ enerji seviyesi uzaklıktaki tuzak enerji seviyelerinin LWIR HgCdTe ($\lambda_c \sim 10 \mu\text{m}$) hassasiyetini en çok bozduğu gösterilmiştir. TAT sebebiyle meydana gelen I/f gürültüsünün düşük ters öngerilimleme ve $1 \times 10^{14} \text{ cm}^{-3}$ seviyesindeki tuzak yoğunluklarında sensor performansına, $11 \mu\text{m}$ üzerindeki kesim dalga boylarından sonra dominant etki yaptığı gösterilmiştir. Söz konusu tuzak yoğunluğunun altındaki tuzak yoğunlukları HgCdTe için çok nadir rapor edildiği bilinmelidir. Bu sebeple, istenen termal görüntüleme kalitesini bu sensörlerle sağlamak için istisnai de olsa tuzak olmayan malzeme gerekmektedir.

Auger mekanizmasının sensor hassasiyetine yönelik iki tip etkisinin olduğu simülasyonlarla gösterilmiştir. Bu etkiler, Auger mekanizmasının karanlık akımı artırması ve foto akımı azaltmasıdır.

Bildiğimiz kadarıyla, bu çalışma HgCdTe dedektör performans parametrelerini en detaylı araştıran, bir simülasyon tabanlı araştırmadır. Elde edilen sonuçlar, HgCdTe sensör optimizasyon yeteneği kazandırmakta ve üçüncü nesil termal kameraların ihtiyaçlarının ve performans parametrelerinin gerçeğe yakın belirlenmesine imkan sağlamaktadır.

Anahtar Kelimeler: HgCdTe, fotodedektör, sayısal simülasyon, TAT

To my wife Halime, my daughter Nilüfer Beyza and my son Burak Ali

ACKNOWLEDGMENTS

I would like to thank to my thesis advisor Prof. Dr. Cengiz Beşikci for his guidance, supervision and providing me the possibility to work in such a sophisticated laboratory. It was not possible to complete this study without his continuous support and motivation.

I would like to thank Prof. Dr. Tayfun Akın and Prof. Dr. Ekmel Özbay for being in my thesis progress comitee. I would also like to thank to Dr. Seliş Önel for her useful lecture on numerical programming with MATLAB.

I would like to thank Prof. Dr. Mehmet Parlak and Assoc. Prof. Dr Haluk Külâh for being in my thesis committee.

I would like to thank Dr. Süleyman Umut Eker, Dr. Oray Orkun Cellek, Dr. Selçuk Özer, Dr. Sema Memiş, Mr. Yetkin Arslan, Mr. Alp Tolunguç, Mr. Ümid Tümkaya and Ms. Özlem Ersagun for sharing with me their knowledge about semiconductor physics and manufacturing, for their valuable comments and opinions and their friendship.

I would like to thank Mr. Burak Aşıcı for the discussions and his opinions, his efforts to help me in our work and his friendship.

I would like to thank Mr. Özgür Şen for the extraordinary energy and effort that he has produced in order to keep the laboratory running and for his friendship.

I would like to thank all of the past and present members of our research group for their friendship.

Last but not the least, I want to express my deep love and gratitude to my wife Halime, my daughter Nilüfer Beyza and my son Burak Ali for their never ending support.

TABLE OF CONTENTS

ABSTRACT	iv
ÖZ	vi
ACKNOWLEDGMENTS	ix
TABLE OF CONTENTS	x
LIST OF TABLES	xiii
LIST OF FIGURES	xiv
LIST OF ABBREVIATIONS	xviii
CHAPTERS	
1. INTRODUCTION	1
1.1 Basics of Infrared Detection.....	1
1.1.1 Planck’s Radiation Law	2
1.1.2 Atmospheric Transmission.....	3
1.2 Basic Principles of IR Imaging Systems.....	6
1.2.1 Optics for IR Systems	6
1.2.2 Principles of Scanning and Staring Systems.....	6
1.3 Infrared Photon Detector Types	7
1.3.1 Low Bandgap Semiconductor Photodetectors	10
1.3.2 Quantum Well Infrared Photodetectors (QWIPs)	11
1.3.3 Quantum Dot Infrared Photodetectors (QDIPs).....	13
1.3.4 Superlattice Detectors	14
1.4 Figures of Merit for IR Photon Detectors	15
1.4.1 Responsivity.....	15
1.4.2 Noise	15
1.4.3 Detectivity	17
1.5 Applications of Infrared Imaging.....	17
1.6 Objective and Presentation of the Thesis Work.....	20

2. HgCdTe DETECTORS: STATE OF THE ART AND MODELING	23
2.1 State of the Art in HgCdTe Detector Technology	23
2.1.1 History of HgCdTe.....	23
2.1.2 Material Properties of HgCdTe	24
2.1.3 Growth of HgCdTe	28
2.1.4 HgCdTe Photodetector Structures.....	30
2.2 Literature Survey on the HgCdTe Detector Modeling.....	33
2.3 Contributions of This Work	37
3. MODELING APPROACH	40
3.1. Introduction to Semiconductor Modeling and Simulation.....	41
3.2 Drift-Diffusion (DD) Model	44
3.2.1 Poisson's Equation	44
3.2.2 Continuity Equations.....	44
3.2.3 Current Equations.....	45
3.3 Transport Equations and Material Parameters for HgCdTe Device Modeling	46
3.4 Recombination-Generation Mechanisms	48
3.4.1 SRH Recombination	48
3.4.2 Radiative Recombination	50
3.4.3 Auger Recombination	52
3.4.4 Mathematical Modeling of Trap Assisted Tunneling (TAT).....	53
3.4.5 Lifetime Modeling	57
3.4.6 Mathematical Modeling of Photogeneration Rate	58
3.5 MCTsim Numerical Solver for HgCdTe Photodiode Simulation.....	59
3.5.1 Boundary Value Problem.....	59
3.5.2 Scaling Transport Equations for MCTsim	60
3.5.3 Ordinary Differential Equations of MCTsim	62
3.5.4 Program Architecture of MCTsim	63
3.5.5 Purpose of hk1ode.....	63
3.5.6 Purpose of hk1init	64
3.5.7 Study of Boundary Conditions for MCTsim.....	65
3.5.8 Program Validation	66

4. SIMULATION RESULTS AND DISCUSSION	67
4.1 Material Parameters and Simulation Strategy.....	67
4.2 Effects of G-R Mechanisms versus Cut-Off Wavelength.....	72
4.3 Dependence on Trap Characteristics.....	77
4.4 Effects of the Auger R-G Mechanism.....	82
4.5 Numerical Fit to the Experimental Data	87
5. CONCLUSION AND FURTHER WORK.....	89
REFERENCES.....	91
CURRICULUM VITAE	100

LIST OF TABLES

TABLES

Table 3.1 Scaling values [63].....	61
Table 4.1 Simulation parameters.....	68

LIST OF FIGURES

FIGURES

Figure 1.1 IR and visible ranges in electromagnetic spectrum	2
Figure 1.2 Blackbody spectral photon exitance at different temperatures	3
Figure 1.3 Atmospheric transmission spectrum and absorbing molecules [5]	4
Figure 1.4 Block diagram of an IR imaging system [9].....	6
Figure 1.5 Block diagrams of (a) scanning and (b) staring system [4].....	7
Figure 1.6 Basic optical excitation processes in the semiconductors: (a) intrinsic absorption, (b) extrinsic absorption, and (c) free carrier absorption [5]	8
Figure 1.7 Ideal detectivity (D^*) spectra of various IR detectors looking at 300K background through 180° field of view (FOV) [4]	9
Figure 1.8 Geometry (a), and I-V curve (b) of a photovoltaic p-n diode [4].....	10
Figure 1.9 QWIP energy band diagram [4].....	12
Figure 1.10 A simple QDIP structure	13
Figure 1.11 Schematic structure of the Type-II SLS band structure [3].....	14
Figure 1.12 Civil applications of thermal imaging [21].....	18
Figure 1.13 Military land applications of thermal imaging [21].....	18
Figure 1.14 Military airborne and marine applications of thermal imaging [21]	19
Figure 2.1 Energy band gap of HgCdTe as a function of CdTe mole fraction	24
Figure 2.2 Cut-off wavelength of $\text{Hg}_{1-x}\text{Cd}_x\text{Te}$ as a function of CdTe mole fraction .	25
Figure 2.3 Lattice constant of HgCdTe versus Cd mole fraction	26

Figure 2.4 Optical absorption coefficient (α) of HgCdTe as a function of CdTe mole fraction	27
Figure 2.5 Intrinsic carrier concentration of HgCdTe versus CdTe mole fraction	27
Figure 2.6 Diagram of a general MBE growth chamber.....	29
Figure 2.7 Photograph of METU MBE reactor for HgCdTe	29
Figure 2.8 Cross section of a planar HgCdTe photodiode structure [29]	30
Figure 2.9 Schematic energy band diagram of p^+-n homojunction HgCdTe photodiode structure.....	31
Figure 2.10 Schematic of DLHJ HgCdTe photodetector [34]	32
Figure 2.11 Loophole detector structure [26]	32
Figure 3.1 Design sequence to achieve simulation need [62].....	41
Figure 3.2 Description of the device simulation sequence [62].....	42
Figure 3.3 Transport models (the dotted-boxes are the semi-classical approaches and the solid-boxes are the quantum approaches) [62].....	43
Figure 3.4 Macroscopic water flow similar to microscopic drift-diffusion continuity equations [62].....	45
Figure 3.5 Analogy of water flow [62]	45
Figure 3.6 Schematic of SRH recombination [68].....	49
Figure 3.7 Illustration of radiative recombination [66].....	51
Figure 3.8 Dominant Auger processes in HgCdTe [41]	52
Figure 3.9 Schematic of tunneling mechanisms [3].....	54
Figure 3.10 Simulated structure and the possible thermal and thermal assisted tunneling transitions [71] in different portions of the depletion region of the device. Dashed and solid arrows represent thermal and tunnel transitions, respectively.....	56
Figure 3.11 MCTsim numerical solver	60
Figure 3.12 MCTsim architecture	63

Figure 3.13 Purpose of hk1ode	64
Figure 3.14 Purpose of hk1nit.....	65
Figure 3.15 Purpose of hk1bc	65
Figure 3.16 Boundaries of photodiode (V_a is the applied bias voltage).....	66
Figure 4.1 Simulated device geometry.....	70
Figure 4.2 Workflow of the simulations	71
Figure 4.3 Contribution of various G-R mechanisms to the dark current under reverse bias voltages of 25 and 100 mV ($\lambda_c=10\text{ }\mu\text{m}$, $N_t=10^{14}\text{ cm}^{-3}$, $d_{abs}=8\text{ }\mu\text{m}$, $T=77\text{ K}$).....	73
Figure 4.4 Squared magnitude of the noise current spectral density due to TAT and other g-r (including photon noise) mechanisms under 25 mV reverse bias ($N_t=10^{14}\text{ cm}^{-3}$, $E_t=0.5E_g$, $d_{abs}=8\text{ }\mu\text{m}$, $T=77\text{ K}$, f/2 optics, 300 K background).....	74
Figure 4.5 R_dA with respect to cut-off wavelength (λ_c) and applied bias (V_a) voltage ($N_t=10^{14}\text{ cm}^{-3}$, $E_t=0.5E_g$, $d_{abs}=8\text{ }\mu\text{m}$, $T=77\text{ K}$).....	75
Figure 4.6 Current responsivity with respect to cut-off wavelength (λ_c) and applied bias (V_a) voltage ($N_t=10^{14}\text{ cm}^{-3}$, $E_t=0.5E_g$, $d_{abs}=8\text{ }\mu\text{m}$, $T=77\text{ K}$, f/2 optics, 300 K background).....	76
Figure 4.7 Specific detectivity (D^*) with respect to cut-off wavelength (λ_c) and applied bias (V_a) voltage ($N_t=10^{14}\text{ cm}^{-3}$, $E_t=0.5E_g$, $d_{abs}=8\text{ }\mu\text{m}$, $T=77\text{ K}$, f/2 optics, 300)	77
Figure 4.8 Specific detectivity of 10 μm cut-off sensor ($d_{abs}=8\text{ }\mu\text{m}$) biased near zero (10 mV reverse) bias	79
Figure 4.9 Specific detectivity of 14 μm cut-off sensor ($d_{abs}=8\text{ }\mu\text{m}$) biased near zero (10 mV reverse) bias	79
Figure 4.10 Variation of the dominant detectivity degrading trap level with the bias voltage on the detector ($T=77\text{ K}$)	80

Figure 4.11 Energy band diagram of the 10 μm cut-off sensor under (a) small and (b) large reverse bias. The dashed and dotted lines show the traps at $E_t=0.7E_g$ and $0.5E_g$, respectively	81
Figure 4.12 Responsivity versus absorber layer thickness (10 μm cutoff, $N_t=10^{14} \text{ cm}^{-3}$, $E_t=0.5E_g$, $V_a=-0.1 \text{ V}$, $T=77 \text{ K}$). The inset shows the variation of the photocurrent when the Auger mechanism is turned on and off in the simulation ($ F_1F_2 =0.2$, $d_{abs}=8 \mu\text{m}$)	83
Figure 4.13 R-Gs under IR photon illumination ($V_a=-25 \text{ mV}$)	84
Figure 4.14 R-Gs under dark condition ($V_a=-25 \text{ mV}$)	85
Figure 4.15 Profile of $np-n_i^2$ under IR photon illumination ($V_a=-25 \text{ mV}$)	86
Figure 4.16 Profile of $np-n_i^2$ under dark condition ($V_a=-25 \text{ mV}$)	86
Figure 4.17 Experimental and numerical fit currents under dark and illuminated conditions	87

LIST OF ABBREVIATIONS

ABBREVIATIONS

BBT	Band to Band Tunneling
BLIP	Background Limited Performance
DD	Drift-Diffusion
FPA	Focal Plane Array
GaAs	Gallium Arsenide
G-R	Generation Recombination
HgCdTe	Mercury Cadmium Telluride
InAs	Indium Arsenide
InGaAs	Indium Gallium Arsenide
InP	Indium Phosphide
IR	Infrared
LWIR	Long-Wavelength Infrared
MBE	Molecular Beam Epitaxy
MCT	Mercury Cadmium Telluride
MCTsim	Mercury Cadmium Telluride Simulator
METU	Middle East Technical University
MWIR	Mid-Wavelength Infrared
NEP	Noise Equivalent Power
NETD	Noise Equivalent Temperature Difference
NIR	Near Infrared
ODE	Ordinary Differential Equation

QDIP	Quantum Dot Infrared Photodetector
QW	Quantum Well
QWIP	Quantum Well Infrared Photodetector
ROIC	Read-Out Integrated Circuit
SRH	Shockley-Read Hall
SLS	Strained Layer Superlattice
SNR	Signal-To-Noise Ratio
SWIR	Short-Wavelength Infrared
TAT	Trap-Assisted Tunneling
TCR	Temperature Coefficient Of Resistance
VLWIR	Very Long-Wavelength Infrared

CHAPTER 1

INTRODUCTION

1.1 Basics of Infrared Detection

Infrared radiation was discovered by Sir William Herschel in 1800. He used a prism to separate sunlight into its spectral components. Then, he put a thermometer for different colored rays to observe the energy distribution of the spectrum of sunlight. He observed an interesting phenomenon that the temperature increased beyond the red end of the visible spectrum. By this way, he found that spectrum of light also contains some form of invisible rays [1].

Fig. 1.1 shows the infrared (IR) spectral region in the electromagnetic spectrum. IR region just starts where human eye stops seeing. The first IR region is called Near IR (NIR) or Short Wave IR (SWIR). In this region, Night Vision Googles (NVG) using image intensifier tubes (I^2T) and some lasers (wavelength of $1.064\text{ }\mu\text{m}$ and $1.54\text{ }\mu\text{m}$) are operated. Imaging principles in the NIR or SWIR region are basically similar to visible region because both regions use reflected rays for detection. On the other hand, radiated IR rays are detected in mid-wave IR (MWIR), long-wave IR (LWIR), very long-wave IR (VLWIR) and far IR [2].

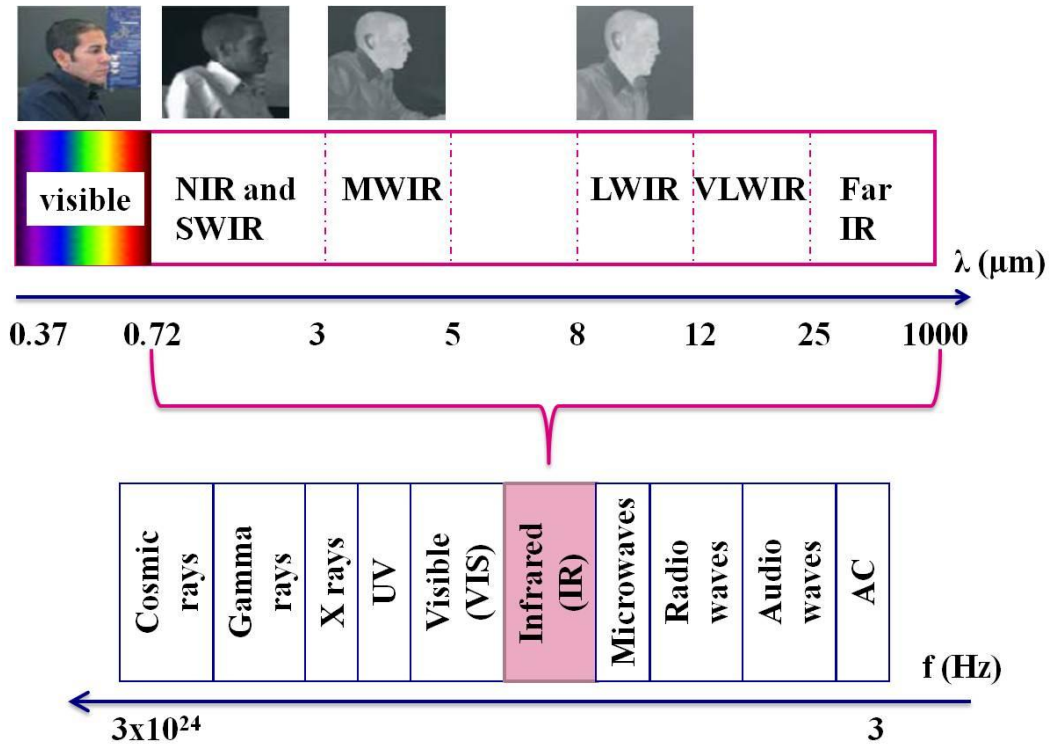


Figure 1.1 IR and visible ranges in electromagnetic spectrum

1.1.1 Planck's Radiation Law

All objects having temperatures larger than 0 Kelvin (absolute temperature) emit IR energy, and this radiation was formulated by Max Planck. If an object is defined as a blackbody, it absorbs all radiation coming at every wavelength. Kirchhoff's Law states that the emissivity of a body or a surface must be equal to its absorptivity at thermal equilibrium. Hence, emissivity (ϵ) of a blackbody is 1. Emissivity is the ratio of total energy emitted by a material at temperature T to the total energy emitted by an equivalent blackbody at the same temperature. Planck's Law describes the spectral photon exitance (M_p) of a blackbody at a specific temperature by

$$M_p = \frac{2\pi hc^2}{\lambda^5 (e^{\frac{hc}{\lambda kT}} - 1)} \quad (1.1)$$

where c is the speed of light, h is the Planck's constant and k is the Boltzmann's constant. Fig. 1.2 shows the spectral photon exitance of blackbody at different temperatures. As seen from the figure, the higher the temperature of the blackbody,

the shorter is the wavelength of the peak radiation. Also, photon exitance increases as the temperature increases. The peak radiation wavelength is given by Wien's Displacement Law. When Planck's Law is differentiated with respect to λ , the maximum radiation wavelength is obtained as

$$\lambda_{max}(\mu m) = \frac{2898}{T(K)}. \quad (1.2)$$

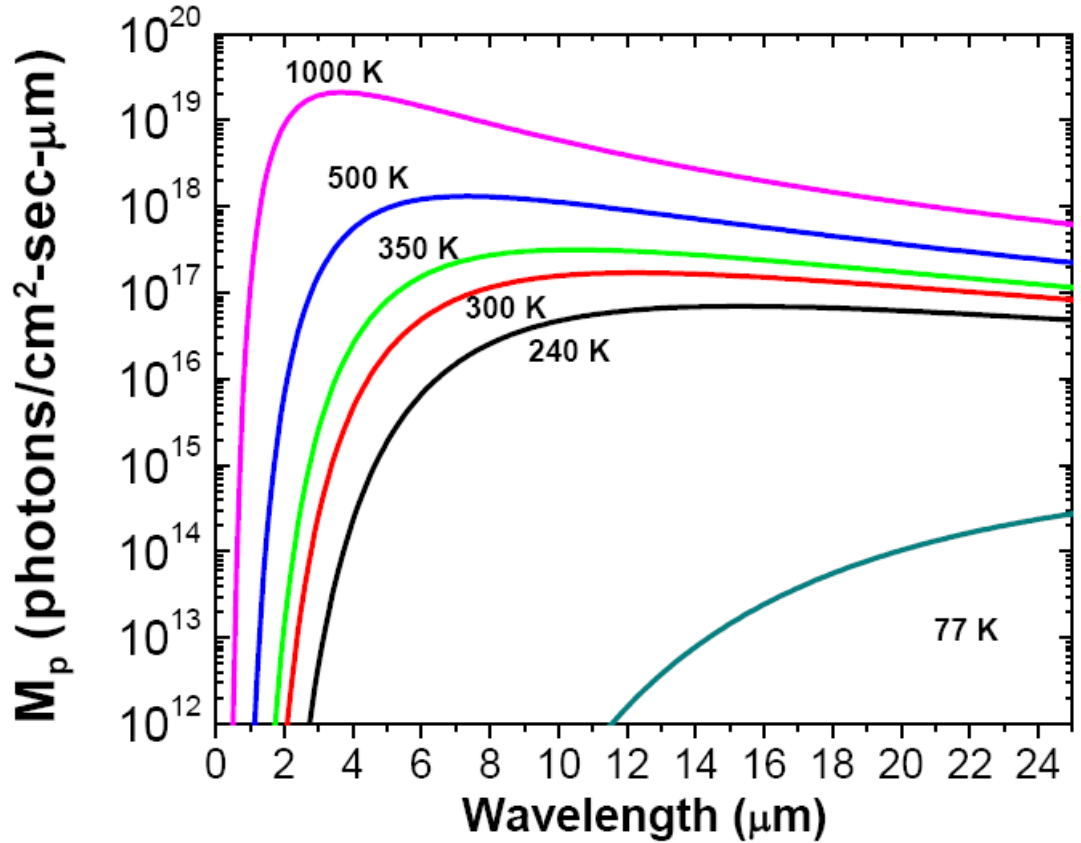


Figure 1.2 Blackbody spectral photon exitance at different temperatures [3]

1.1.2 Atmospheric Transmission

For thermal imaging applications, atmosphere plays an important role in the detection of IR radiation. Atmosphere is also a source of IR radiation forming a background for the target. It attenuates the radiation coming from the object in two different mechanisms: scattering of IR rays by atmospheric particles and absorption by the atmospheric gas molecules. Both mechanisms result in attenuation of IR.

Fundamental IR absorbing molecules in the atmosphere are H_2O , O_3 , N_2O , CO , CH_4 , and N_2 . Absorption by these molecules may occur either due to electronic transitions in constituent atoms or vibrational states of atoms in the gas molecules. A common atmospheric transmission spectrum is given in Figure 1.3. As seen from the figure, atmosphere transmits several spectral regions. These regions are called “atmospheric transmission windows”. These windows are generally named as follows [4]:

- NIR (Near Infrared): 0.7 to 1.5 μm .
- SWIR (Short Wavelength Infrared): 1.5 to 3 μm .
- MWIR (Mid Wavelength Infrared): 3 to 5 μm .
- LWIR (Long Wavelength Infrared): 8 to 12 μm .
- VLWIR (Very Long Wavelength Infrared): 12 to 25 μm .
- FIR (Far Infrared): greater than 25 μm .

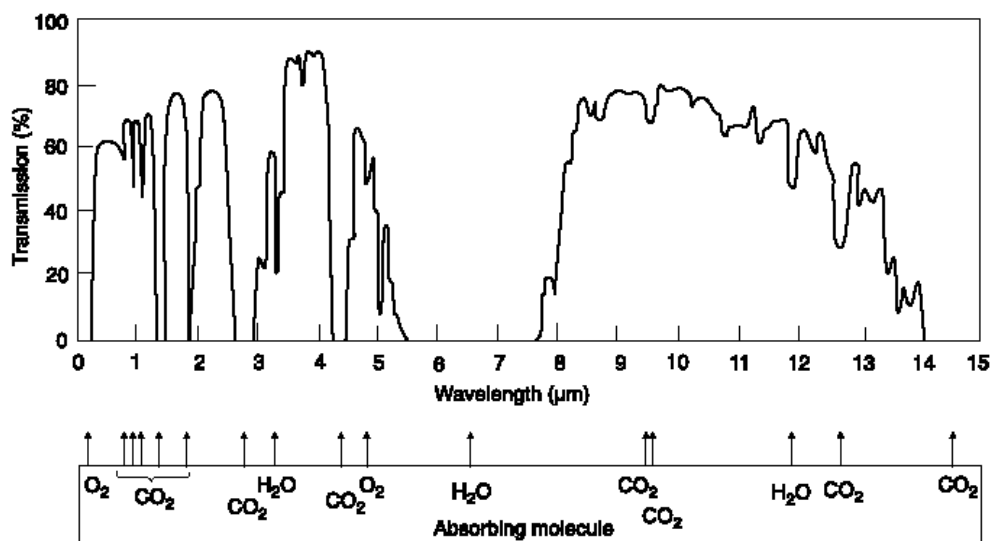


Figure 1.3 Atmospheric transmission spectrum and absorbing molecules [5]

The atmospheric transmission spectrum given in Figure 1.3 depends on the environmental conditions like altitude, relative humidity, climate, and gas content [6]. Besides, the atmosphere is an inhomogeneous medium and its refractive index is a complex function of time and position, depending on winds, thermal convection currents, the gravitational field, and humidity. Additionally, battlefield obscurants

like artillery round dust, fog oil, and white phosphorus scatter the light and significantly reduce the transmission.

The MWIR and LWIR spectral windows are widely used for land, marine, and airborne thermal imaging, where imaging is performed by directly sensing the photons emitted by the objects. Each spectrum has advantages and disadvantages with respect to other. At near room temperature, the photon flux of objects is much higher in the LWIR band compared to MWIR band. Also, LWIR window is less sensitive to scattering from molecules as scattering rate is inversely proportional to the radiation wavelength [7]. On the other hand, hot targets such as missiles and exhaust gases emit more photons in the MWIR band. Also, IR radiation is less absorbed by water vapor in the MWIR band as compared to the LWIR band.

Spectral window selection depends on the target signature (target versus background), atmospheric transmission, and sensor response (optics and detector). For example, for maritime applications, where the humidity is relatively high, MWIR is suitable whereas LWIR is more appropriate in low humidity and cold environments. In battlefield conditions, LWIR is more suitable because longer wavelength radiation penetrates the obscurants more effectively [8]. Also, there are several high intensity sources like muzzle flash on a battle ground scene resulting in partially saturated images. MWIR imagers are more deeply affected by such sources because of the very large difference in the exitance of the hot and room temperature objects in this band.

MWIR and LWIR windows may not be satisfactory alone. Combination of both windows, called dual band, or splitting one window to two windows, called dual color, are very important for enhancing the capability of the thermal imaging system. As a result, depending on the environmental conditions, sometimes MWIR band sometimes LWIR band becomes more useful for thermal imaging.

1.2 Basic Principles of IR Imaging Systems

The performance of an infrared imaging system depends on target signature, environmental conditions, and building components of the imager [9]. A basic block diagram of an IR imager is given in Figure 1.4.

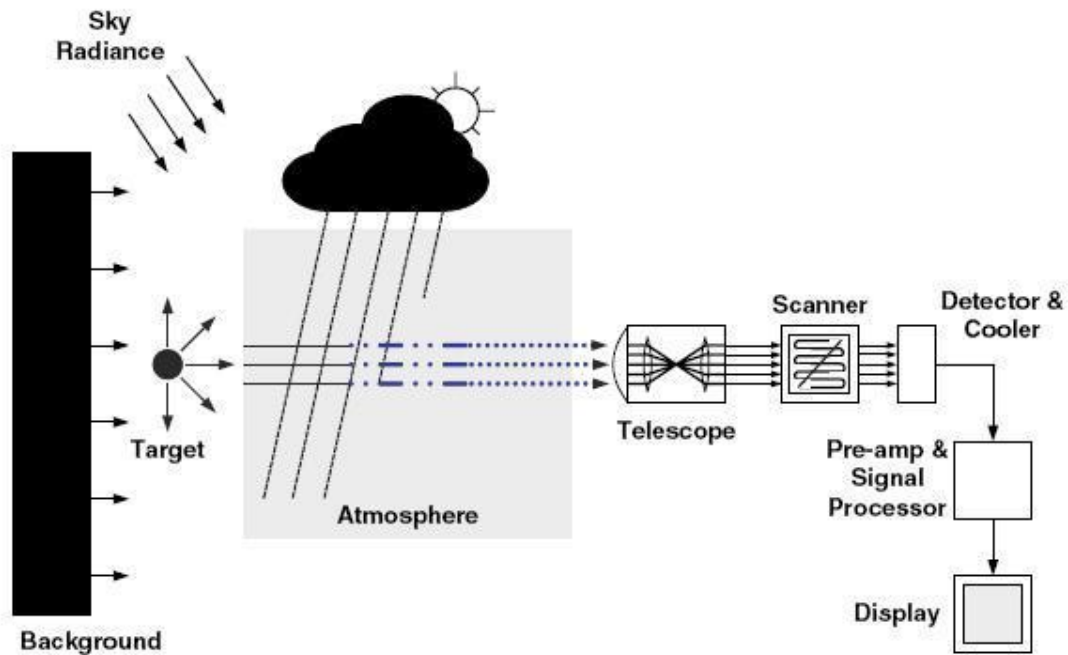


Figure 1.4 Block diagram of an IR imaging system [9]

1.2.1 Optics for IR Systems

Either focusing lenses or reflective mirrors may be used to obtain the image of a target on detectors. Spectral characteristics of optical parts are mainly determined by the material type and anti-reflection coatings. In MWIR and LWIR bands, Ge, ZnS and ZnSe are most widely used lens materials for IR detection.

1.2.2 Principles of Scanning and Staring Systems

A thermal imaging system can be classified into scanning and staring optics depending on the number of pixels on the detector array. A thermal imager may have a single pixel detector, a line array or a two-dimensional staring array. Figure 1.5 shows these systems. In scanning systems, rotating mirrors, or refracting prisms are

driven mechanically to get the segments of the target scene onto detector elements sequentially. In linear array detectors (60x1, 120x1, 288x4, 480x6, 576x7 pixels etc.), scanning is performed in only one direction. On the other hand, single-pixel sensors utilize both horizontal and vertical scanning directions.

A staring array system is similar to human eye. It consists of a 2-D array of detector pixels and does not require mechanical scanning. Scanning arrays require bulky mechanical scanning systems and are generally used when it is not easy to produce large format, uniform 2-D detector arrays.

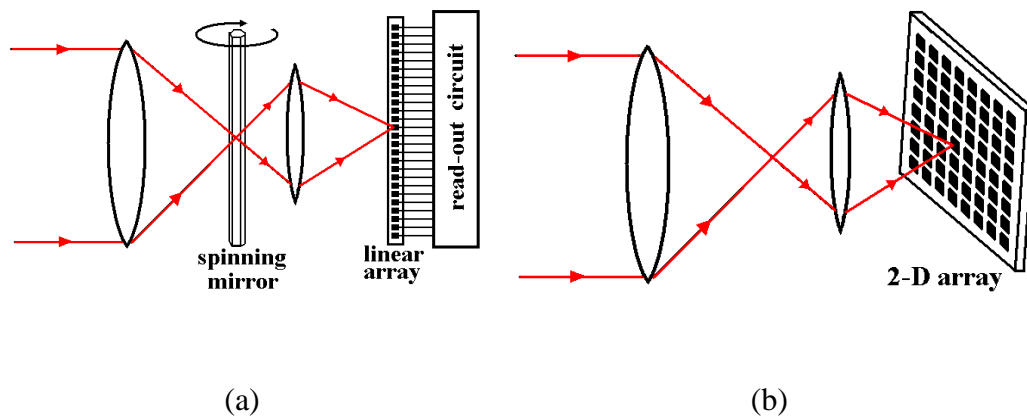


Figure 1.5 Block diagrams of (a) scanning and (b) staring system [4]

2-D arrays should have very high uniformity, which is not so easy to realize with some material systems. On the other hand, scanning arrays (line arrays) are carried out on a small wafer area, therefore the uniformity problem is not very important. Some scanning systems include additional signal processing methods to increase the signal-to-noise ratio like time-delay integration (TDI) and signal processing in the element (SPRITE) techniques [10].

1.3 Infrared Photon Detector Types

In photon detectors, IR radiation is absorbed due to the interaction of incident photons with electrons, either bound to lattice atoms, or impurity atoms or with free

electrons. These mechanisms are shown in Figure 1.6 [11]. Photon detectors have high detectivity, as well as small response time, and the responsivity of photon detectors displays wavelength dependence. Photon detectors are separated into different types with respect to the nature of the electron-photon interaction as intrinsic, extrinsic, free carriers, and quantum well detectors. Another way to classify photon detectors is with respect to electrical output of the detector as photoconductive, photovoltaic, capacitance, and photoelectromagnetic. The most significant ones with respect to electrical output classification are photoconductive and photovoltaic detectors.

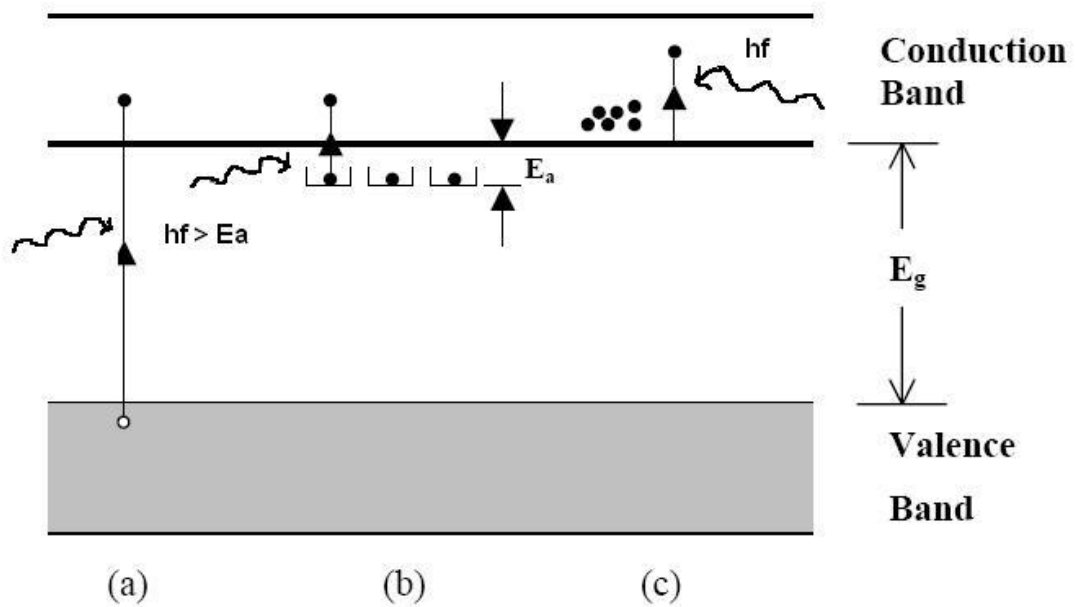


Figure 1.6 Basic optical excitation processes in the semiconductors: (a) intrinsic absorption, (b) extrinsic absorption, and (c) free carrier absorption [5]

In intrinsic detectors, photons having energy greater than fundamental band gap of the detector material are converted into electron-hole pairs. HgCdTe, InSb, and InAs are the most widely used intrinsic detector materials. Spectral characteristics of various infrared detectors are given in Figure 1.7. Response of the detector decays very rapidly for photons with energy lower than the energy band gap of the detector material. Intrinsic type detectors can be photoconductive or photovoltaic in relation to the electrical output of the detector.

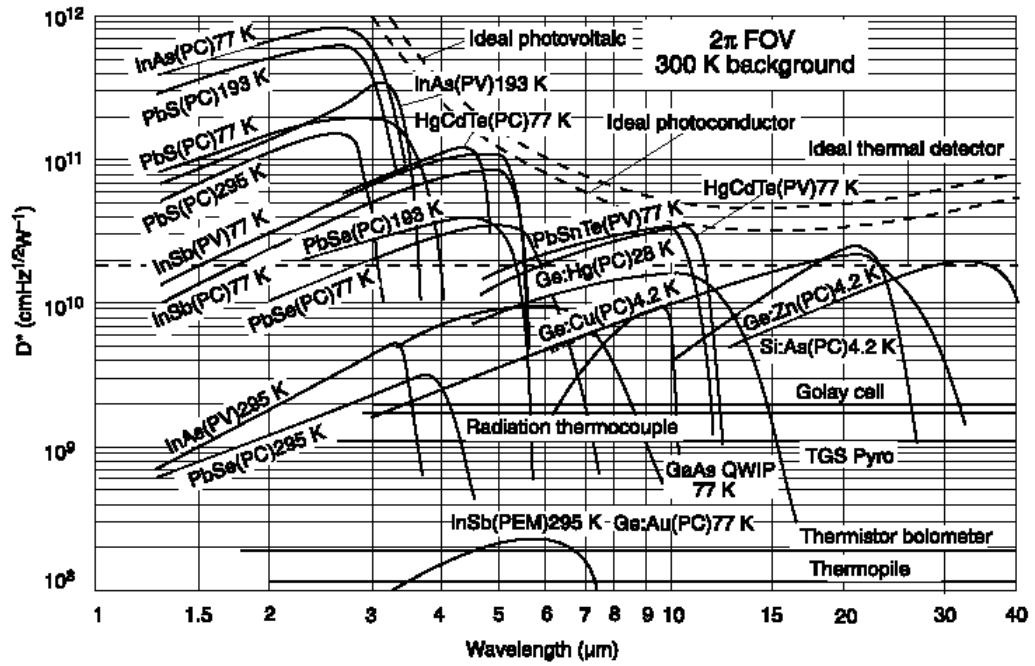


Figure 1.7 Ideal detectivity (D^*) spectra of various IR detectors looking at 300K background through 180° field of view (FOV) [4]

Photoconductive devices operate with photo-generation of charge carriers. The conductivity of the semiconductor increases due to photo-generated charge carriers. In order to eliminate the recombination of the photo-generated charge carriers, sufficiently large bias voltage must be applied to the photoconductive detector. Although photoconductive type detectors may yield high responsivity, they are not suitable for large format focal plane arrays (FPA) due to large bias and current levels required [5].

Photovoltaic detectors are most widely used. They have an internal potential barrier with a built-in electric field. Basic photovoltaic detectors are p-n or p-i-n diodes, heterostructure diodes, Schottky barrier diodes, and metal-insulator-semiconductor (MIS) photo-capacitor devices. Fig. 1.8 shows the geometry and operation of a simple photodiode. Incident radiation creates electron-hole pairs in p and n type regions. These electrons and holes diffuse towards the junction and are swept to the opposite side by strong electric field of the depletion region.

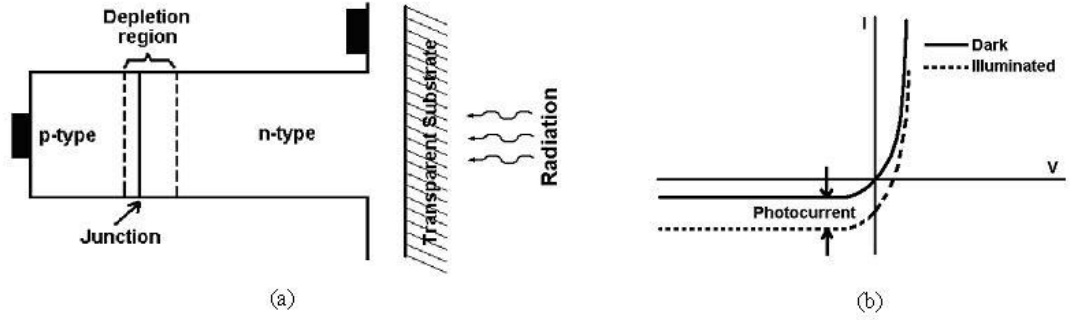


Figure 1.8 Geometry (a), and I-V curve (b) of a photovoltaic p-n diode [4]

By this way, the following photocurrent is produced in the device.

$$I_{ph} = \eta q A \Phi \quad (1.3)$$

where η is the quantum efficiency, q is the charge of electron, A is the area of the photodiode, and Φ is the incident photon flux density.

In extrinsic detectors, photonic transition takes place from impurity states to the valence band or the conduction band. Energy levels of the doped impurities (such as silicon or germanium) determine the limit on the detection wavelength. Extrinsic detectors operate as photoconductors. The main disadvantage of extrinsic type detectors is the requirement of cooling down to very low temperatures such as the liquid helium temperature in order to achieve reasonably low noise levels.

1.3.1 Low Bandgap Semiconductor Photodetectors

In order to sense IR radiation in the MWIR and LWIR spectral regions, low energy bandgap materials are used. Most widely used of these kinds of semiconductors are HgCdTe, InSb and InAsSb.

Hg_{1-x}Cd_xTe (Mercury Cadmium Telluride-MCT): It is one of the most important semiconductors for IR detection. HgCdTe is a direct bandgap material. Its absorption coefficient is very high which provides high quantum efficiency. x represents CdTe mole fraction in the HgCdTe alloy. Cutoff wavelength of HgCdTe can be adjusted from 0.7 to 20 μm by changing the CdTe mole fraction. More details about HgCdTe

are given in Chapter 2. Old generation thermal imaging equipments have photoconductive HgCdTe sensors with 30x1, 60x1, 120x1 and 180x1 FPA formats. New IR imagers have photovoltaic HgCdTe sensors with 288x4, 480x6, 576x7, 128x128, 256x256, and larger FPA formats.

InSb (Indium Antimonide): It is a III-V compound semiconductor. InSb is an important semiconductor for the detection of IR in the MWIR region. The cutoff wavelength is 5.5 μm at 77 K. Like HgCdTe, it is a direct bandgap material. Since InSb has high electron mobility [12], it has been used in IR imaging systems, magnetoresistive sensors, high-speed photodetectors and free space communication. InSb has strong covalent bonding, and large area InSb wafers (128x128, 256x256 etc.) are commercially available for MWIR applications [13].

In_{1-x}As_xSb (Indium Arsenide Antimonide): It is a ternary alloy for MWIR and LWIR applications. InAsSb is a direct bandgap material and its bandgap can be changed by varying the antimony mole fraction (x). The cutoff wavelength is tunable from 3.1 μm ($x = 0.0$) to 9.0 μm ($x \approx 0.6$). The longest cutoff wavelength of InAsSb is 9 μm at 77 K. High quality InAsSb photodetectors for MWIR region have been developed during the last decades [11].

1.3.2 Quantum Well Infrared Photodetectors (QWIPs)

In intrinsic IR photodetectors, interband absorption takes place in low bandgap semiconductors. On the other hand, processing of low-bandgap materials is rather difficult when compared with those of large bandgap materials like GaAs. It was discovered that IR detection is possible by using larger bandgap materials after Esaki and Sakaki proposed AlGaAs/GaAs quantum well structures for IR detection in 1977 [14]. Levine *et al.* demonstrated the first QWIPs in 1987. Since then, this technology has been researched so extensively that large format MWIR and LWIR QWIP FPAs (1024x1024), which show comparable performance to state-of-the-art HgCdTe detectors are available today [15].

As shown in Fig. 1.9, the quantum well is formed by sandwiching a well material (dark green) between larger bandgap barrier materials (gray). Electrons (blue) or holes (light green) are excited to the second subband under illumination. Quantized states in the potential well are used, and the energy difference between the first two quantized state energy levels adjusts the peak absorption wavelength of the structure. Fortunately, the energy gap between quantized energy levels (subbands) can be varied by adjusting the compositional and dimensional parameters of the quantum well and barrier. This gives great flexibility to designer, and it becomes possible to detect IR light even in the VLWIR ($>12\text{ }\mu\text{m}$) range. AlGaAs/GaAs is the most commonly used material system. AlGaAs/GaAs QWIPs have some advantages over narrow bandgap intrinsic photodetectors. These are higher yield, radiation hardness, and lack of $1/f$ noise till very low frequencies [4]. In addition to AlGaAs/GaAs material system, there are other material systems used to realize QWIP structures such as InGaAs/InP, InGaAs/InAlAs, GaAs/GaInP, GaAs/AlInP, and InGaAs/GaAs.

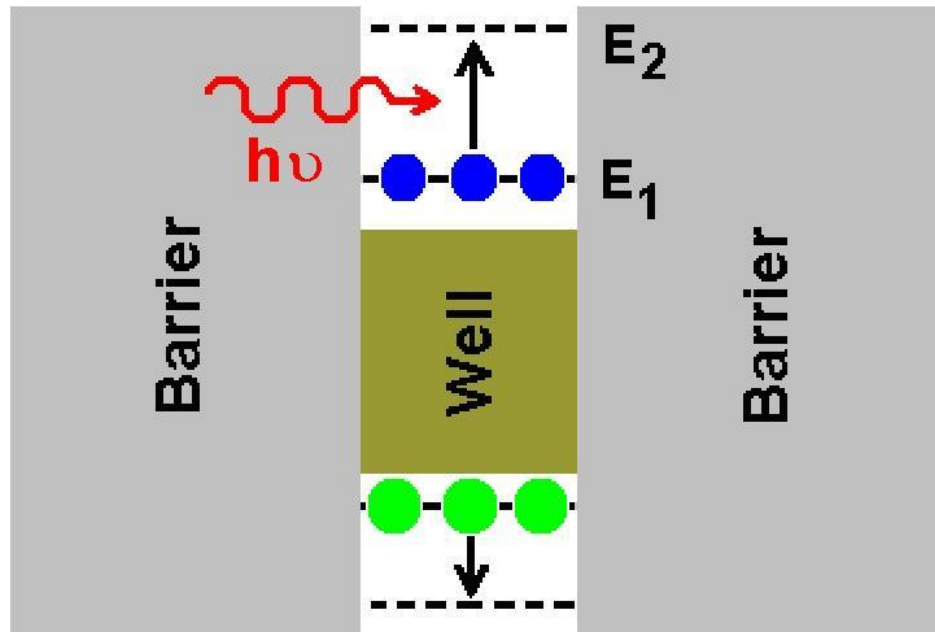


Figure 1.9 QWIP energy band diagram [4]

1.3.3 Quantum Dot Infrared Photodetectors (QDIPs)

QDIPs work on the basis of intersubband transition like QWIPs. Generically, QDIPs are very similar to QWIPs. If quantum wells in QWIPs are replaced with quantum dots, QDIPs occur. A basic QDIP structure is shown in Fig. 1.10.

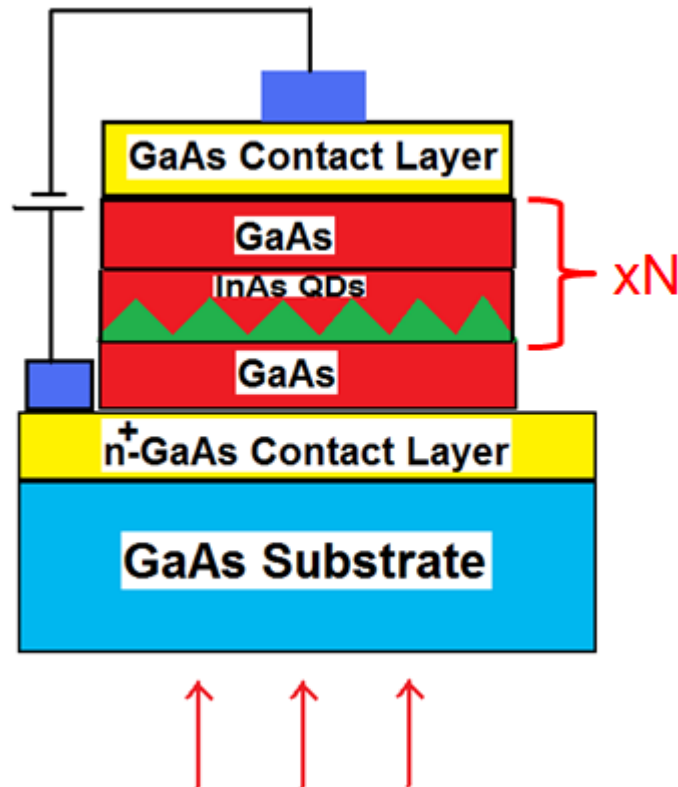


Figure 1.10 A simple QDIP structure [3]

Some advantages of QDIPs over QWIPs can be given as follows [7]

- QDIPs detect normal incidence radiation which eliminates the need for the fabrication of grating coupler.
- In theory, dark current of QDIPs is less than both HgCdTe and QWIP.
- Thermionic emission is reduced as a result of confinement in all three dimensions. Therefore, electron relaxation time increases due to phonon bottleneck. Hence, signal to noise ratio of QDIPs is expected to be larger than that of QWIPs.

QDIPs are expected to have superior characteristics compared to HgCdTe detectors in theory. In terms of detector performance, QDIPs and Type-II SLS can theoretically compete with HgCdTe photodetectors. But, the measured 77 K detectivities of QDIPs are less than the QWIP and HgCdTe detector performances because of the difficulties faced with the growth of the QDIP structures [16]. Control of the dot size and the dot shape is difficult with the current epitaxial growth techniques. Enhancing the growth, doping and fabrication conditions may result in a better QDIP detector performance [17].

1.3.4 Superlattice Detectors

Recently, a InAs/Ga(In)Sb material system based Type-II Strained Layer Superlattice (SLS) detectors have been researched as an alternative to the standard HgCdTe and QWIP detector technology. Type-II SLS detectors have an interlaced band structure such that the conduction band of the InAs layer is lower than the valence band of the Ga(In)Sb layer, thus forming a virtual bandgap. The schematic structure of the Type-II SLS band structure is given in Fig. 1.11.

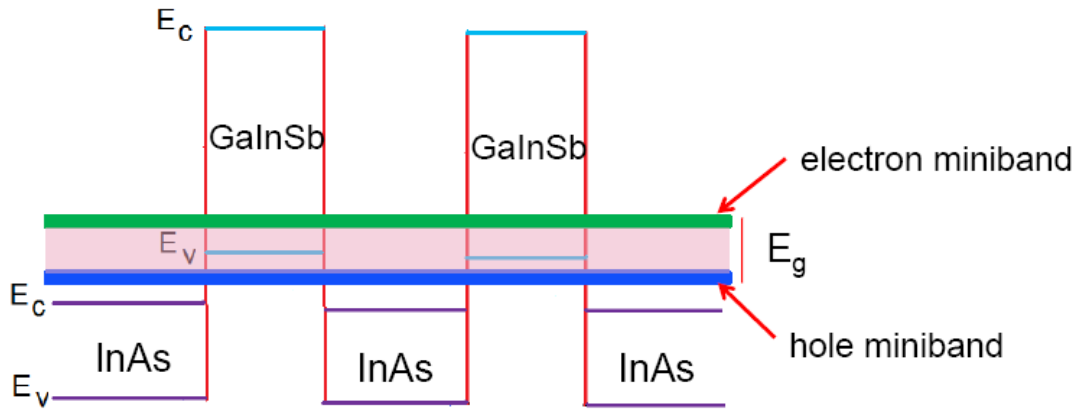


Figure 1.11 Schematic structure of the Type-II SLS band structure [3]

As shown in Fig. 1.11, heavy holes are mostly restricted to the GaInSb layers, while electron wave functions overlap considerably between adjacent InAs layers by the help of very thin barriers. This overlap causes the formation of an electron miniband in the conduction band. Spatially indirect transition between the localized heavy

holes and the electron miniband defines the IR detection capability of Type-II SLS structures [18].

1.4 Figures of Merit for IR Photon Detectors

IR photon detectors are assessed according to certain figures of merit. These parameters are briefly discussed below.

1.4.1 Responsivity

Responsivity is the change of detector output signal with respect to incoming IR radiation.

$$R_I = \frac{\text{Photocurrent (A)}}{\text{Photon Power (W)}} = \frac{I_{ph}}{P_{det}} = \frac{I_{ph}}{A_d \times H} = \frac{J_{ph}}{H} \quad (1.4)$$

where A_d is the detector area (cm^2), P_{det} is power of incoming infrared (IR) radiation (W), and H is IR photon incidence (W/cm^2).

1.4.2 Noise

Noise is unwanted fluctuations at the output. There are several noise mechanisms for photodetectors such as $1/f$ noise, Johnson noise, shot noise, and generation-recombination (g-r) noise.

Johnson (Nyquist or Thermal) Noise: It is due to thermally generated carriers. Thermal fluctuations exist when the temperature is above 0 K resulting in thermal noise observed in a conductor. It is **WHITE** noise.

$$i_{n-thermal}^2 = \frac{4kT\Delta f}{R} \quad (1.5)$$

where $R = \left(\frac{\partial I}{\partial V} \right)^{-1}$ is dynamic resistance. In terms of the resistance-area product,

Equation (1.5) becomes

$$i_{n-thermal}^2 = \frac{4kT\Delta fA}{R_dA} \quad (1.6)$$

where A is the detector-pixel area.

g-r (shot) Noise: It is due to photo-generated carriers. Electrons and photons are quantized (can not be divided) causing fluctuations in the current in an electronic or optical device. The shot noise may appear in a photodetector due to the random arrival of photons. It may also appear in a p-n junction diode where the charge carriers cross potential energy barrier. It is important at low current levels where the fluctuation is at considerable level with respect to the average current. It differs from the Johnson noise in the sense that a bias voltage must be applied to the device to observe the g-r noise [3].

$$i_{n-gr}^2 = 2q(I_{dark} + I_{ph})\Delta f = 2qI_{total}\Delta f \quad (1.7)$$

where I_{ph} is the photocurrent due to absorbed IR photons, I_{dark} is the detector dark current when IR illumination does not occur, and Δf is the bandwidth.

$1/f$ (Pink) Noise: This noise has been observed in many different physical systems with difficulties in identifying the exact origin leading to an unsolved problem. $1/f$ noise causes fluctuations in the signal with noise spectral density proportional to $1/f$ over a wide range of frequencies limiting the low frequency detectivity.

In the low frequency range, considerable $1/f$ noise occurs in the HgCdTe photodiodes. TAT component of the total dark current is related to the $1/f$ noise current [19]. Nemirovsky and Unikovsky [20] reported an empirical relationship between tunnelling leakage current of HgCdTe photodiode and $1/f$ noise with a trend given as

$$i_{n1/f} = \frac{\alpha I_{TAT}^\beta}{f^{0.5}} \quad (1.8)$$

$$i_{n1/f}^2 = \left[\frac{\alpha I_{TAT}^\beta}{f^{0.5}} \right]^2 \Delta f \quad (1.9)$$

where α and β are device-dependent variables. $i_{n1/f}$ is $1/f$ noise current spectral density in $A/Hz^{0.5}$. I_{TAT} is the trap-assisted tunneling (TAT) contributed dark current. For HgCdTe photodiodes, experimental leakage current from the TAT mechanism results in β values close to 0.5 and α taking a value of 1×10^{-6} ($A^{0.5}$) for a wide range of temperatures and reverse bias voltages, where the TAT is the dominant tunneling mechanism [20].

Total Noise: Total noise is the square root of sum of squares of individual noises.

$$i_n = \sqrt{(i_{n-thermal}^2 + i_{n-gr}^2 + i_{n1/f}^2)} \quad (1.10)$$

1.4.3 Detectivity

The detectivity is defined as the inverse of noise equivalent power (NEP), where NEP is the minimum amount of signal power in order to obtain unity signal-to-noise ratio. However, as the square of the noise current is directly proportional to the detector area and the measurement bandwidth, a sensitivity parameter which is independent from the detector area and measurement bandwidth should be defined, so called specific detectivity D^* expressed as

$$D^* = \frac{R_I \sqrt{A_d \Delta f}}{i_n} \left[\frac{cm \sqrt{Hz}}{W} \right] \quad (1.11)$$

where R_I is the current responsivity and i_n is the total noise current.

1.5 Applications of Infrared Imaging

IR imaging is widely used both in civil and military areas. Civil applications include driver vision enhancement, security systems, industrial process control, fire alarms, medical imaging, and satellite instruments. Military applications cover land, airborne and marine thermal sight systems, mine detection, search and track, reconnaissance, IR guided missiles, and fire control systems. Some civil and military applications are presented in Figs. 1.12 to 1.14.



Figure 1.12 Civil applications of thermal imaging [21]



Figure 1.13 Military land applications of thermal imaging [21]



Figure 1.14 Military airborne and marine applications of thermal imaging [21]

Fire fighting: IR imaging can be used for fighting against the forest fires. In normal visible region, it is impossible to see hot spots or flames from the air due to the dense smoke above the region. But, smoke is transparent to the IR light, and firefighters can see and concentrate on the critical points on the fire region [4]

Medicine: IR imaging is an alternative technique for screening and diagnosing purposes in medicine. Medical trials using an IR imager have been discussed by Fauci *et al.* [22]. In medical applications, desired features are high sensitivity, small number of dead pixels, high thermal and spatial resolution, short acquisition time, compatibility with large focal depth optics, and low cost FPAs [23]. A QWIP based IR medical imager system has been utilized which accumulates hundredths of successive IR images and performs fast Fourier transform (FFT) analysis of the skin temperature homogeneity [4]. This system may also be used in the determination of breast/skin tumor and brain surgery.

Defense: In military applications, temperature of the target and background may vary drastically. Highly sensitive FPAs are required for discrimination of the target from the background when warm targets with high background irradiance are observed. The need for very high performance, multispectral, uniform and high yield

FPA becomes more significant when strategic applications are considered. Degraded or dead pixels may cause a target to be missed completely. Missile seeker systems need higher operating temperatures, and lower cooldown times. On the other hand, reconnaissance systems need medium to large format FPAs, and use closed-cycle cooling to reach operating temperatures of 77 K. IR detection of cold launch vehicles requires utilization of LWIR band because temperature difference between the body and hot plume of the vehicle is quite high (250K and 950K, respectively) during initial stages of launch [4]. Blackbody flux ratios of these temperatures are 25000 for $\lambda=4\text{ }\mu\text{m}$ and 115 for $\lambda=8.5\text{ }\mu\text{m}$. Therefore, higher detection wavelength is preferred to get a cold body and hot plume together within dynamic range. As a result, specific applications determine the requirements for the IR imaging system.

In addition, it was shown that multispectral IR detectors can be used to detect buried land mines [24]. If the soil is disturbed to bury a mine, emission spectrum of the quartz in the soil differs, and returns to its steady state radiation after several weeks. Most important change in the emissivity occurs in a narrow band between 8-9 μm requiring two-color narrow-band detection [4].

1.6 Objective and Presentation of the Thesis Work

HgCdTe is a significant material for detection of infrared radiation. HgCdTe is generally used as a p-n diode structure to sense VLWIR, LWIR, and/or MWIR radiation. Fabrication of a HgCdTe IR photodetector device is complicated and expensive. In order to improve the device performance, its photoelectrical properties need to be deeply understood and optimized using the device simulators. Up until now, limited amount of work has been realized in HgCdTe photodiode numerical device simulation.

$\text{p}^+\text{-n}$ HgCdTe photodiode performance at 77K needs to be investigated in a more comprehensive way. The effects of various current generating mechanisms could be more realistically extracted by considering the interactions of IR photogeneration with other R-G mechanisms since real HgCdTe photodetectors which are used in various military and civil thermal imaging systems operate under IR illuminated

conditions. Therefore, effective R-G mechanisms such as TAT, SRH and Auger should be investigated considering the impacts of these interactions. In our study, a numerical solver is developed to simulate p^+-n homojunction HgCdTe LWIR and VLWIR photodiodes. It solves Poisson and continuity equations in one dimension. All important recombination-generation mechanisms including TAT are well incorporated into the code to evaluate the performance of the HgCdTe device at 77K. The solver isolates numerically the dark current contributions of different recombination-generation mechanisms. We perform several simulations to understand the behavior of p^+-n HgCdTe photodiode performance at 77K in the LWIR and VLWIR bands.

The main objective of this work is to identify the individual and combined effects of various material/detector parameters on the sensitivity of HgCdTe detectors. With this objective in mind, the numerical simulator is constructed with all possibly dominant g-r mechanisms (Auger, radiative, SRH and TAT) and detector noise sources (Johnson, g-r and $1/f$). The level of detail incorporated into the simulator, as well as the calculations carried up to the sensor detectivity level yield important observations enlightening some critical issues that should be taken into consideration by the detector designer. Therefore, we believe that the results presented in this thesis will complement the relevant information in the literature toward establishing the guides for the design of HgCdTe sensors.

Chapter 2 presents detailed information on HgCdTe detector technology along with the material properties, the growth technology and HgCdTe photodetector structures. This chapter will also include a literature survey on HgCdTe detector modeling.

In Chapter 3, simulation work is described in all aspects. This chapter will explain steady-state physical modeling of p^+-n HgCdTe homojunction photodetector. The mathematical model consists of two current density equations, two continuity equations and Poisson's equation. Simultaneous solution of these five nonlinear equations in one dimensional space is achieved using a numerical solver which is developed in MATLAB environment. Continuity equations include all dominant

recombination-generation processes in HgCdTe. These processes employed in the mathematical modeling are also explained in this chapter.

Chapter 4 is dedicated to the simulation results and discussion. This chapter will present the results of various numerical simulations with the solver under dark and IR-illuminated conditions. Simulation results are post-processed and discussed to reach the main objectives described above.

Finally, Chapter 5 lists of the important conclusions of this thesis work as well as a summary of future work.

CHAPTER 2

HgCdTe DETECTORS: STATE OF THE ART AND MODELING

2.1 State of the Art in HgCdTe Detector Technology

Mercury cadmium telluride (MCT, $\text{Hg}_{1-x}\text{Cd}_x\text{Te}$) is a ternary alloy formed with HgTe (mercury telluride) and CdTe (cadmium telluride). $\text{Hg}_{1-x}\text{Cd}_x\text{Te}$ has been the most significant semiconductor for mid-wavelength and long-wavelength IR imaging applications.

2.1.1 History of HgCdTe

The first investigations on HgCdTe were reported by Lawson and colleagues in 1958 and 1959 [25]. After they prepared HgCdTe alloys with different CdTe and HgTe mole fractions, they saw that by changing the mole fractions it is possible to obtain HgCdTe alloys with energy band gap values changing continuously from the energy band gap value of CdTe to that of HgTe. They also reported the photoconductive and photovoltaic response of HgCdTe alloys at wavelengths extending to 12 μm [26]. The 50-year history of $\text{Hg}_{1-x}\text{Cd}_x\text{Te}$ has seen the three generations of IR detector devices: the first, the second and the third generations. The first generation of devices is photoconductive linear arrays (like 30x1, 60x1, and 120x1) which have been produced in large quantities and are still in widespread use. The second generation devices are photovoltaic two dimensional arrays which are today in high production rate. The third generation devices are two-color detectors, avalanche photodiodes, and hyper-spectral arrays.

2.1.2 Material Properties of HgCdTe

MCT is the only well-behaved intrinsic semiconductor with an energy band gap of around 0.1 eV (for $x \approx 0.2$), which makes this alloy very significant for IR imaging at LWIR band [27]. CdTe and HgTe have zinc-blende structures. $\text{Hg}_{1-x}\text{Cd}_x\text{Te}$ has also zinc-blende structure for all x values. At 77 K, CdTe has an energy band gap value of 1.6088 eV and HgTe has an energy band gap value of -0.2608 eV. $\text{Hg}_{1-x}\text{Cd}_x\text{Te}$ has a direct energy band gap changing from energy band gap value of CdTe to that of HgTe as x varies from 1 to 0. There exist some equations expressing the energy band gap value of $\text{Hg}_{1-x}\text{Cd}_x\text{Te}$ in terms of x and temperature. The expression given by Seiler *et al.* is as follows [28]

$$E_g = -0.302 + 1.93x - 0.81x^2 + 0.832x^3 + 5.35 \times 10^{-4}(1-2x)(-1882 + T^3) / (255.2 + T^2) \quad (2.1)$$

where E_g is the energy band gap of $\text{Hg}_{1-x}\text{Cd}_x\text{Te}$ in eV and x is the mole fraction of CdTe. T is the temperature in Kelvin. Energy band gap of $\text{Hg}_{1-x}\text{Cd}_x\text{Te}$ for x between 0 and 0.30 is given in Fig. 2.1 for three different temperatures with respect to Eq. (2.1).

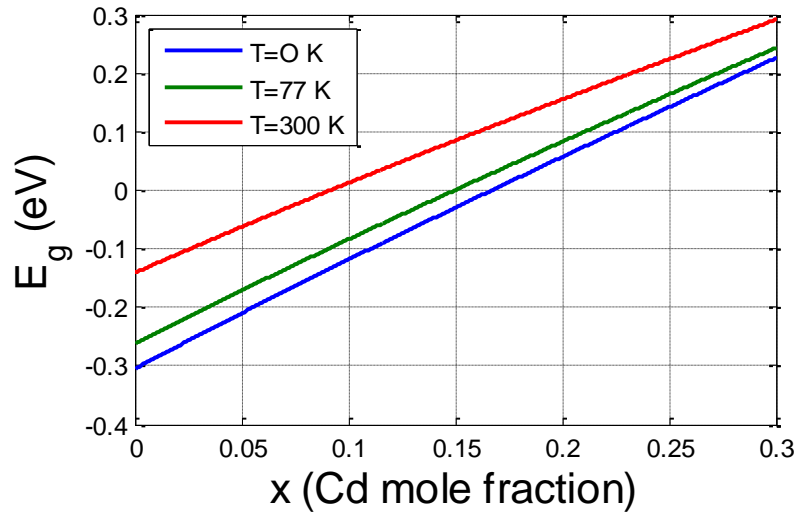


Figure 2.1 Energy band gap of HgCdTe as a function of CdTe mole fraction

Cut-off wavelength can be calculated from the energy band gap values by using the simple equation

$$\lambda_{cut-off}(\mu m) = \frac{1.24}{E_g(eV)} \quad (2.2)$$

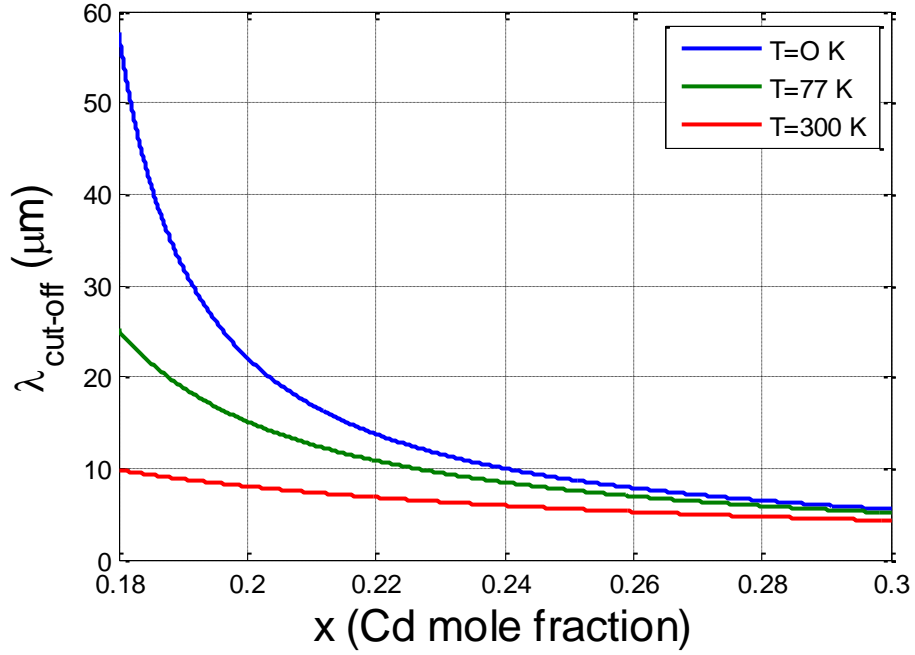


Figure 2.2 Cut-off wavelength of $Hg_{1-x}Cd_xTe$ as a function of CdTe mole fraction

Energy band gap of $Hg_{1-x}Cd_xTe$ is adjustable from 0.7 μm ($x = 1$) to 25 μm ($x \approx 0.18$ at 77 K). The problem related to large format LWIR HgCdTe FPAs is well depicted by Figure 2.2. In The LWIR band (8-12 μm), small variation in CdTe mole fraction causes large variation in the cut-off wavelength of $Hg_{1-x}Cd_xTe$. This situation results in considerable nonuniformity over a large area. Therefore, very large format LWIR staring FPAs are not yet available [5].

HgCdTe is the rare semiconductor covering the entire IR region of the electromagnetic spectrum with a small change in the lattice constant [27]. The lattice constant (a) of HgCdTe as a function of x is given by Higgins [11]

$$a = 6.4614 + 0.0084x + 0.01168x^2 - 0.0057x^3 \quad (2.3)$$

where “ a ” is in terms of angstroms (Å). Eq. (2.3) is plotted in Fig. 2.3. As seen in this figure, the lattice constant of CdTe ($x=1$) is only 0.3 % larger than that of HgTe ($x=0$). This is very important since small variation of lattice constant permits the fabrication of new devices based on lattice matched high quality complex epitaxial layers.

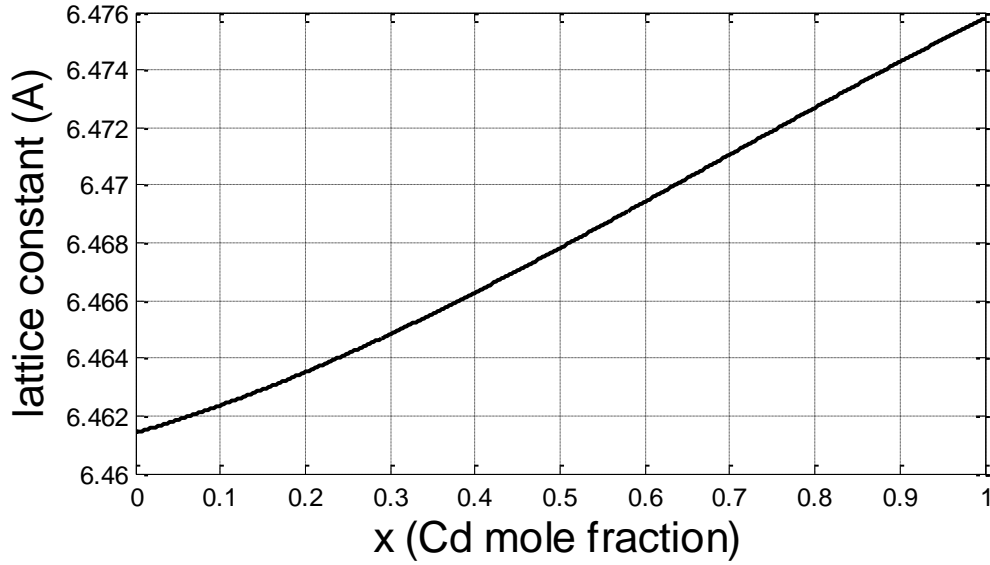


Figure 2.3 Lattice constant of HgCdTe versus Cd mole fraction

HgCdTe is a direct energy band gap material, and it has a very sharp optical absorption characteristic. Optical absorption coefficient of $\text{Hg}_{1-x}\text{Cd}_x\text{Te}$ as a function of x is given in Fig. 2.4 [29]. As a result of the strong optical absorption of HgCdTe, relatively thin layer of HgCdTe about 8–20 μm is sufficient for absorption of high percentage of the IR flux yielding high quantum efficiency. Hougen [28] formula for absorption coefficient is given by

$$\alpha = 100 + 5000x \quad (2.4)$$

where x is the Cd mole fraction. In Fig. 2.4, absorption coefficient is plotted according to Hougen formula in a range of $x=0.1$ to 0.3.

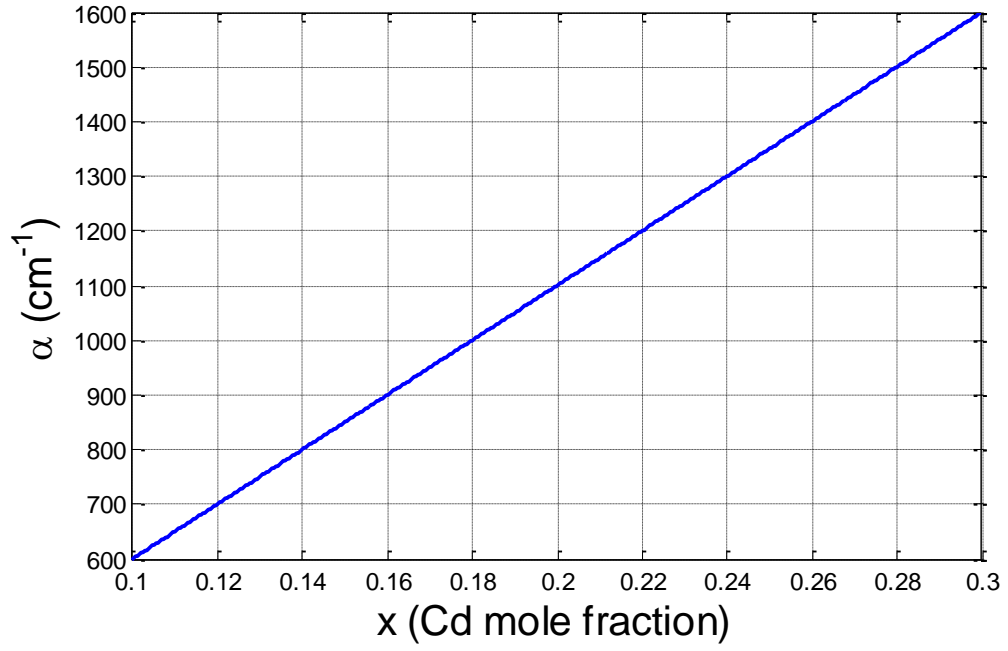


Figure 2.4 Optical absorption coefficient (α) of HgCdTe as a function of CdTe mole fraction

The intrinsic carrier concentration of HgCdTe can be calculated using the following expression [19]

$$n_i = (5.24256 - 3.57290x - 4.74019 \times 10^{-4}T + 1.25942 \times 10^{-2}xT - 5.77046x^2 - 4.24123 \times 10^{-6}T^2) 10^{14} E_g^{3/4} T^{3/2} \exp(-E_g / (2kT)) \quad (2.5)$$

where T is in Kelvin and k is Boltzmann's constant. n_i is plotted in Fig. 2.5.

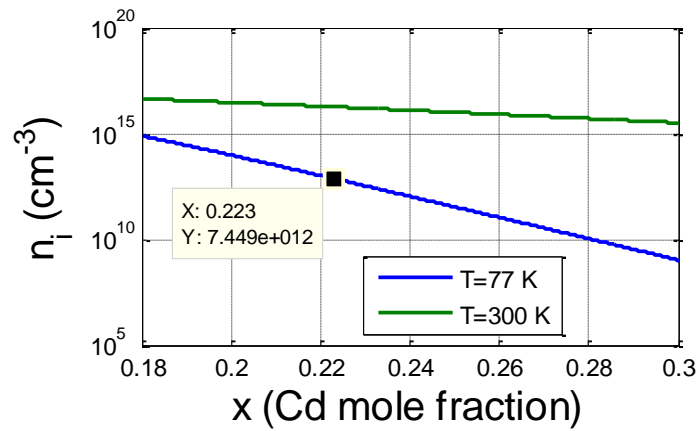


Figure 2.5 Intrinsic carrier concentration of HgCdTe versus CdTe mole fraction

2.1.3 Growth of HgCdTe

High quality epitaxial growth of HgCdTe on a sufficiently large area is needed for the fabrication of large format staring arrays. CdZnTe is the standard substrate for HgCdTe. It provides good lattice match with the HgCdTe epilayers. Liquid phase epitaxy (LPE), metal organic vapor phase epitaxy (MOVPE) or molecular beam epitaxy (MBE) techniques can be used for the epitaxial growth of HgCdTe. Although the conventional epitaxial growth technique for HgCdTe is LPE, important progress has been made on the growth of HgCdTe with MBE and MOVPE, which permit the fabrication of advanced and complex detector structures such as two-color detectors by providing good control of composition, layer thickness and doping. MCT detector manufacturers have started to utilize MBE or MOVPE for the improvement of the detector performance and/or lower the cost of fabrication through the use of new detector structures and large Si or GaAs substrates [5]. More detailed information discussing the growth of HgCdTe with the above techniques is available in references [30] and [31].

MBE technique was developed in the early 1970s as a process of growing high-purity epitaxial layers of compound semiconductors [32]. Since that time it has evolved into a popular technique for growing III-V and II-VI compound semiconductors as well as several other materials. MBE can yield high-quality layers with very abrupt interfaces and good control of thickness, doping, and composition. Because of the high degree of control possible with MBE, it is an important tool in the development of sophisticated electronic and optoelectronic devices [33]. A general diagram of MBE chamber and the photograph of the METU HgCdTe MBE reactor are given in Fig. 2.6 and Fig. 2.7, respectively.

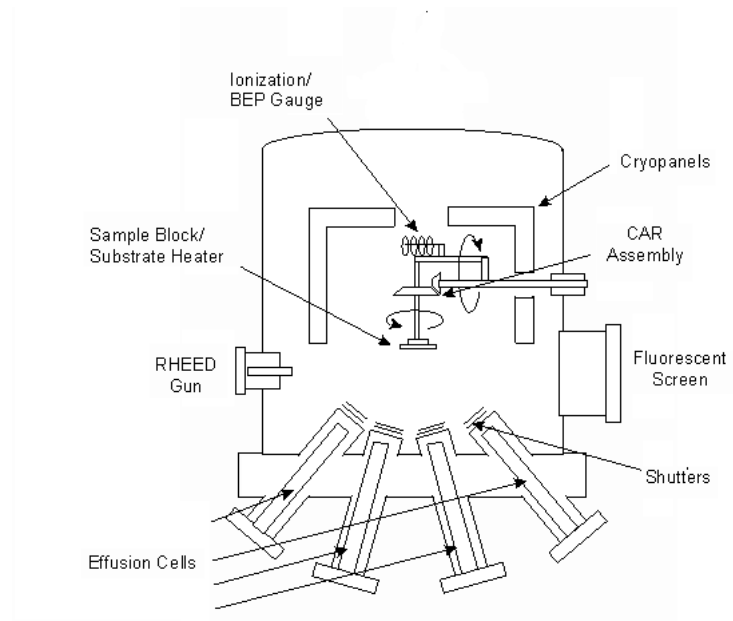


Figure 2.6 Diagram of a general MBE growth chamber [33]

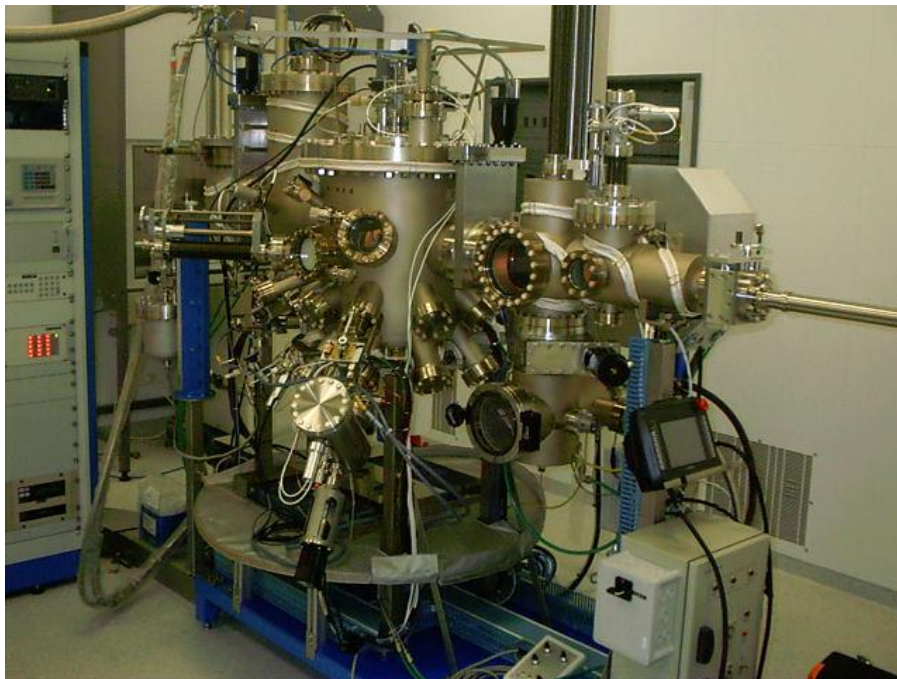


Figure 2.7 Photograph of METU MBE reactor for HgCdTe

2.1.4 HgCdTe Photodetector Structures

Several HgCdTe detector structures have been adopted by the detector manufacturers and considerable amount of research work is carried out on the new structures. The most widely used structures are described below.

Planar HgCdTe Detectors: The planar device structure is illustrated in Fig. 2.8. It is the simplest device structure currently used. It is consistent with a number of junction forming processes, e.g. ion implantation, diffusion and ion milling [34]. The pn junction is mass connected to a silicon ROIC multiplexer using indium bumps. The device shown in Fig. 2.8 is backside-illuminated, i. e. it is illuminated through the substrate. Careful control of the junction geometry is required to avoid crosstalk due to the diffusion of minority carriers into adjacent pixels, especially in the case of small pixel sizes. The thermal expansion mismatch between the HgCdTe/CdZnTe substrate combination and the silicon ROIC is another important consideration in this device structure and this can restrict the practical size of the array unless the CdZnTe substrate is thinned.

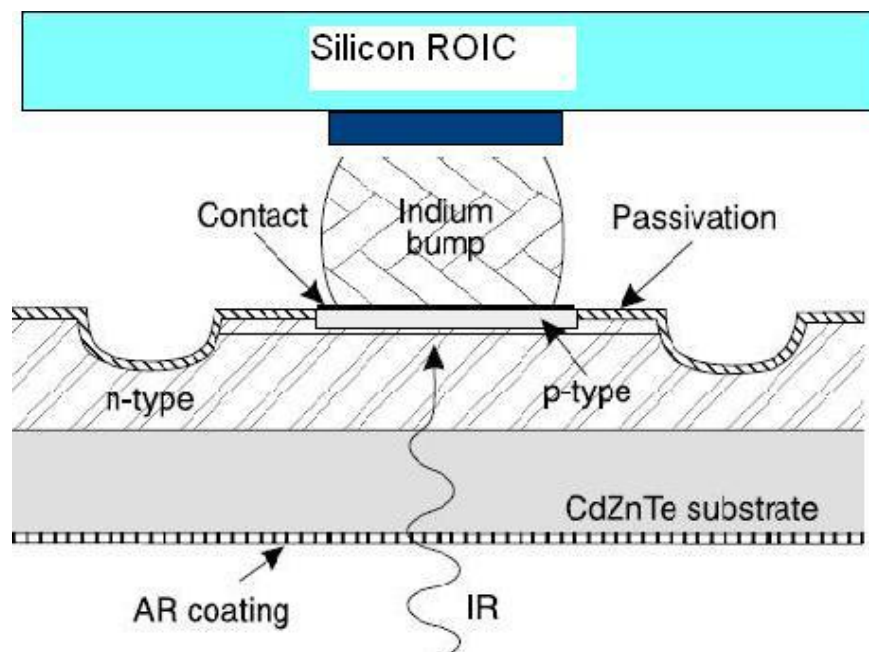


Figure 2.8 Cross section of a planar HgCdTe photodiode structure [29]

Energy band diagram of p^+-n homojunction HgCdTe photodiode is illustrated in Fig. 2.9.

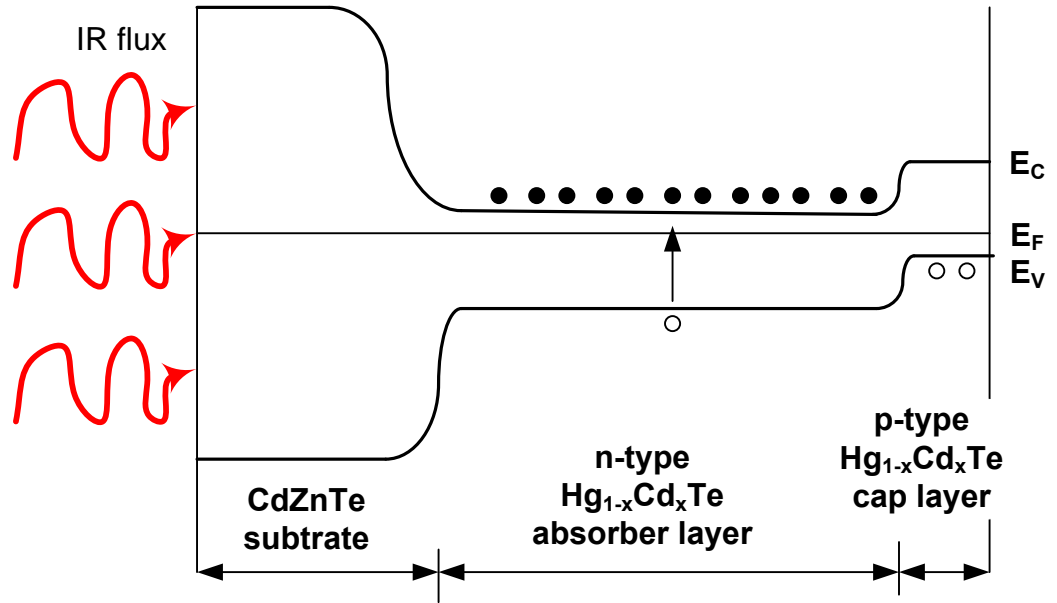


Figure 2.9 Schematic energy band diagram of p^+-n homojunction HgCdTe photodiode structure

Double Layer Heterojunction (DLHJ) HgCdTe Detectors: P-n (where capital P designates the wide energy band gap layer, and the lower case n designates the narrow energy gap layer) double layer heterojunction HgCdTe photodiode structures became more popular than the planar n^+-p or p^+-n homojunctions due to the following advantages [26]:

- It is easier to control the low carrier concentration in n-type base layer than p-type base layer for HgCdTe,
- Passivation of n-type base (absorber) layer is easier than p-type base layer,
- n-type HgCdTe is relatively free of Shockley-Read centers that limit the lifetime in p-type material.

The schematic of DLHJ HgCdTe is shown in Fig. 2.10.

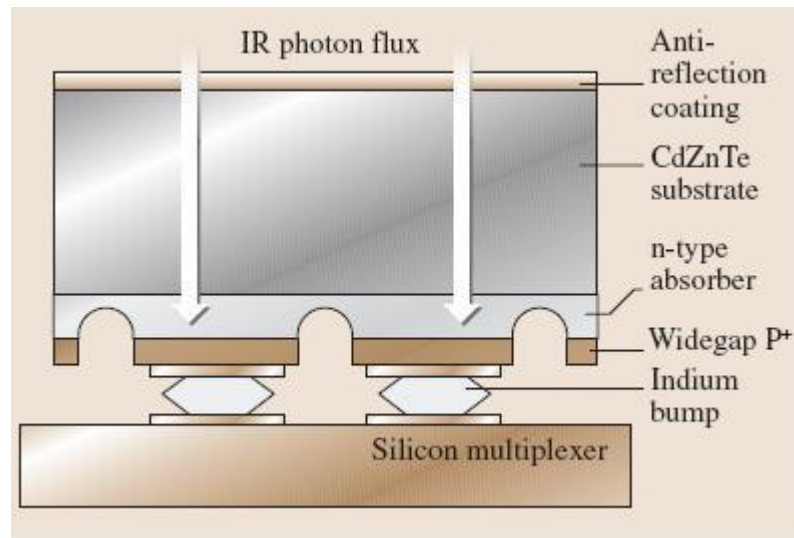


Figure 2.10 Schematic of DLHJ HgCdTe photodetector [34]

Double-layer heterojunction devices have been developed mainly in the United States for LWIR detectors with low thermal leakage currents (or high R_0A values). A number of device structures have been reported with R_0A values that are an order of magnitude higher than those of via-hole or planar diodes. The backside-illuminated mesa P^+-n heterojunction, illustrated in Fig. 2.10, is a widely used device, and has been reported from both LPE and MBE material [34].

Loophole HgCdTe Detectors: In this approach, HgCdTe material is glued to the ROIC and then the substrate is thinned to 10-20 μm thickness. After the substrate thinning, via holes are drilled to form electrical contacts between pixels of the FPA and the pixels of ROIC [26]. Figure 2.11 shows the loophole structure.

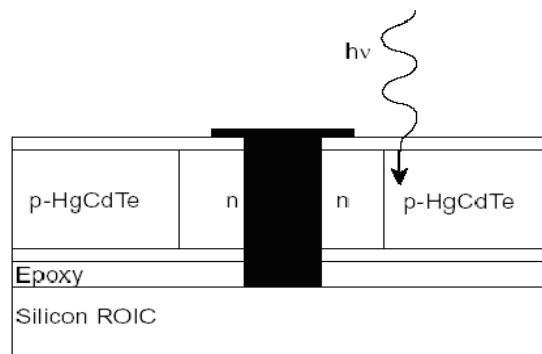


Figure 2.11 Loophole detector structure [26]

2.2 Literature Survey on the HgCdTe Detector Modeling

In order to improve the HgCdTe device performance, its photoelectrical properties need to be deeply understood and optimized using modeling and simulations. In this section, studies on HgCdTe detector modeling reported in the literature are presented.

There exist various reports in the literature on the numerical simulation of HgCdTe photodetectors. While some studies utilized commercial device simulators [35], [36], [37], [38], [39] and [40], most of the other approaches utilized the drift-diffusion model including the current and continuity equations coupled with the Poisson equation. Summers *et al.* [41] used the drift-diffusion model in 1-D incorporating the Shockley-Read-Hall (SRH), Auger, radiative and avalanche g-r mechanisms to simulate n^+pp^+ , n^+np and pin LWIR detector structures and enlightened the importance of Auger 1 and 7 mechanisms in limiting the carrier lifetime. Their model was based on the complete ionization of dopant atoms, nondegenerate Maxwell-Boltzmann statistics and a midband-gap trap energy level. The computation of carrier concentrations and particularly the minority carrier concentrations were considered to be the advantages of the numerical simulations over the analytical ones for the evaluation of recombination and generation mechanisms along the device by Summers *et al.* [41].

Rogalski *et al.* [42] followed a similar modeling approach with the objective of comparing p on n and n on p HgCdTe detectors. They have demonstrated the superiority of the p on n detectors in terms of providing larger R_oA products in the LWIR band in agreement with the experimental results. Williams and Wames [36] compared the efficiency of analytical and numerical models for different applications. They summarized the HgCdTe device models.

Karimi *et al.* [43] studied the optimization of the detectivity of LWIR n^+pp^+ HgCdTe detectors using Auger and photoexcitation as g-r mechanisms and including Johnson, g-r and shot noises in the calculation of detectivity. They found that photodiode with lightly doped absorber layer has greatest current responsivity and detectivity. They explained the reason as better depletion of the absorber region due to extraction-

exclusion phenomena for a lightly doped absorber layer. The current responsivity reaches a maximum value at certain absorber region thickness. They attributed this behavior to the increasing of quantum efficiency by increasing the absorber thickness and the decreasing of junction collection efficiency when the absorber thickness becomes greater than the diffusion length. So, they optimized detectivity at 8 μm absorber layer thickness. They explained that increasing reverse bias causes current responsivity to increase and reach to a maximum value, then decrease and saturate. They attributed this behavior to the depletion of absorber region by the extraction-exclusion phenomena and resulting suppression of Auger generation. They optimized the detectivity at 0.14 V reverse bias voltage.

Hu *et al.* [35] utilized a commercial software to investigate the effects of absorption layer thickness (d_{abs}) on the responsivity of LWIR detectors. They used SRH, Auger and radiative recombination terms in the numerical solution. They showed that the photoresponse (responsivity, R_I) increases with the increase of d_{abs} first, and then decreases. They demonstrated that the maximum photoresponse, which is the consequence of competing effects of the absorption and diffusion, is at $d_{\text{abs}} = 11\mu\text{m}$.

Wenus *et al.* [44] utilized a commercial software to investigate the effects of lateral collection of carriers and the position of the p-n junction in the heterostructure on the detector performance. Jozwikowski [45] performed numerical analysis of LWIR multijunction HgCdTe photodiodes. Results were presented in the form of 3D plots illustrating the spatial distributions of electrical potential and responsivity.

Yoo *et al.* [46] emphasized the importance of including the degeneracy and nonparabolicity in the simulators in order to achieve reliable results. They presented the results of 2D simulations incorporating SRH, Auger, radiative, optical and tunneling mechanisms with the indirect (trap) tunneling modeled in the form of a SRH g-r rate. They implemented a simulation based comparison of homojunction and heterostructure devices as well as proposing a structure for cross talk reduction. The authors adopted a simple tunneling rate expression incorporated into the continuity equations. In their study, n-p⁺ homojunction (Cd mole fraction =0.225) and n-P⁺ (Cd mole fraction of n-side=0.225 and p-side=0.3) heterojunction HgCdTe photodiode

simulation results were obtained with the trap density of $1 \times 10^{14} \text{ cm}^{-3}$ and the trap energy of $0.6E_g$.

Hu *et al.* [37] numerically investigated the characteristics of n on p LWIR HgCdTe detectors by extracting the detector parameters from measurements through an improved fitting process. The authors used a commercial software with the tunneling mechanisms inserted into the continuity equation as g-r processes. In this study [37], the 1D analytical model for LWIR HgCdTe photodiode has been improved and validated according to self-consistent numerical results. The measured $R-V$ curves were investigated using a simultaneous-mode data-processing technique over wide voltage and temperature ranges. The extracted parameters were subsequently substituted into their solver for numerical simulations by developing the tunneling models. They found that the simulated dark-current characteristics were in good agreement with measured data over wide voltage and temperature ranges.

Gumenjuk-Sichevskaja *et al.* [47], [48] investigated the HgCdTe detectors using the balance equations including the SRH and trap-assisted tunneling (TAT) as the g-r mechanisms. Jozwikowski *et al.* [49] has recently numerically investigated the current-voltage characteristics of n on p LWIR HgCdTe photodiodes. Radiative, Auger, SRH, TAT, band-to-band tunneling (BTB), and impact ionization mechanisms were included in the solver. Bellotti and D'Orsogna [50] implemented a 3D simulation of two color HgCdTe detectors by including the SRH, Auger and radiative mechanisms as g-r processes.

Saxena and Chakrabarti [51] simulated the performance of $p^+-n^0-n^+$ homojunction $\text{Hg}_{0.78}\text{Cd}_{0.22}\text{Te}$ ($\lambda_c=10.6 \text{ }\mu\text{m}$) using a commercial simulator (ATLAS software of SILVACO) at 77 K. They included SRH, Auger and radiative recombination mechanisms. In the other study of Saxena *et al.*, an abrupt heterojunction photodetector based on HgCdTe has been simulated for mid-infrared (2-5 μm) applications using commercial ATLAS (BLAZE-2D) software package from Silvaco International at room temperature [39]. A source code was written for optical characterization (R_0A product, Responsivity, Detectivity etc.) of the device with the help of MATLAB. They reported that the dark current at room temperature is

dominated by Auger recombination mechanism which in turn produces unwanted noise. In Saxena's recent study [38], the performance of p^+-n-n^+ HgCdTe LWIR homojunction photodetector ($x \approx 0.22$) has been analyzed theoretically and simulated numerically using commercial ATLAS software from SILVACO. The author included Johnson-Nyquist and shot noises in the calculation of the detectivity. In the study of Niedziela *et al.* [52], detection properties of HgCdTe homojunction photodiodes were investigated numerically for 10.6 μm spectral region operating at near-room temperatures. At these temperatures, they consider only Auger 1 and Auger 7 recombination processes. g-r noise was used for detectivity calculation. Their continuity and Poisson's equations were solved with iterative Newton procedure. They reported that the current responsivity (R_I) increases initially with the absorber region thickness (d_{abs}), reaches a maximum for the d_{abs} slightly higher than the diffusion length of minority carriers, then, for higher thicknesses, decreases. In their calculations, only the Johnson-Nyquist noise, dominating in these conditions, has been taken into account. The optimum thickness was found to be close to the diffusion length of minority carriers.

Chekanova *et al.* [53] simulated the HgCdTe structures by considering Johnson-Nyquist and dark current shot noises in the reverse bias case. They have discussed two design concepts of extended LWIR photovoltaic (PV) FPA based on MBE-grown HgCdTe multi-layer structures: Photodiode (PD) with traditional n^+-p junction and novel PD with p-n junction. Their estimation has shown that extended LWIR PD with p-n junction would be potentially of 4-5 times lower dark current value than PD with n^+-p junction at $T=77\text{ K}$.

Kosai [54] explained the historical developments on the HgCdTe device simulations. He summarized the properties of the solvers like one-dimensional HgCdTe detector model HET III and the 2D model SABIR which were being used by a number of Department of Defense laboratories and contractors.

In the study of W. D. Hu *et al.* [55], they realized 2D numerical simulations of spectral photoresponse characteristic for two-color HgCdTe infrared photovoltaic detector. Effects of thickness of absorption layer and doping profiles on the

photoresponse, quantum efficiency and crosstalk were explored. Optimal thickness of absorption layers and doping profiles were numerically evaluated for the n-p-P-P-N HgCdTe two-color heterostructure photodetectors at 77 K. Gopal and Dhar [56] reported the numerical simulations of n^+ on p HgCdTe photodiodes by considering the effect of the perimeter-to-area ratio on the resistance-area product. Keasler *et al.* [57] presented three-dimensional numerical simulation of HgCdTe photodiodes in MWIR and LWIR bands. They used the commercial multi-dimensional device simulator incorporated with Auger, SRH and radiative recombination mechanisms. Dhar *et al.* [58] studied the effect of the surface charges due to the passivant on the R_0A for LWIR HgCdTe photodiodes at 77 K. Ariel and Bahir [59] reported a different approach to the simulation of the heterojunction HgCdTe photodiodes based on an approximation for the nonparabolic Fermi-Dirac integral. Jozwikowska *et al.* [60], [61] numerically investigated the effect of an abrupt CdTe/HgCdTe passivation heterointerface on the generation-recombination and the dark currents for n-on p MWIR HgCdTe photodiodes.

2.3 Contributions of This Work

HgCdTe detector technology is still the dominating alternative for thermal imaging in the long wavelength infrared (LWIR) band. While the performance of these sensors is considerably affected by processing techniques, the ultimate performance of the detector is generally limited by the intrinsic material properties mostly depending on the material composition and growth conditions. In many aspects, it is crucial for the detector designer to estimate the ultimate detector performance with a specific cut-off wavelength based on the practically achievable material properties, as well as predicting the dependence of its performance on various detector parameters. This information would serve as an invaluable guide for optimizing the processing conditions and the sensor structure. While the current literature includes some guiding data, optimum detector design calls for substantial amount of information on the dependence of sensor performance on some intrinsic and growth/processing introduced material properties. This work complements the data in the literature in this sense through a detailed numerical analysis including all of

the dominant mechanisms contributing to the detector current, as well as their interactions.

HgCdTe detector performance and the performance limiting mechanisms have extensively been investigated using experimental results and analytical techniques. As is the case with the other detector technologies, a common approach to assess the HgCdTe detector performance by identifying the individual effects of various dark current generation mechanisms is to fit the expressions of the dark current (resistance) components to the measured detector current (resistance). While this approach is useful for identifying the dominant sensitivity limiting mechanisms for a combination of a particular detector structure and material properties, the large number of curve fitting parameters make reliable data extraction difficult. Furthermore, this technique does not allow enlightening the exact dependence of the sensor performance on intrinsic material properties and estimating the ultimate sensor performance due to the possible presence of processing related (additional) dark current components. Analytical approximations, on the other hand, do not allow accurate predictions of the carrier and E-field distribution throughout the device which may result in the estimation of generation-recombination rates and device currents with insufficient accuracy [41]. Therefore, numerical simulation techniques should be preferred for a thorough investigation and optimization of these sensors, as well as a better understanding of the relation between the device/material parameters and the obtained characteristics.

The main objective of this work is to identify the individual and combined effects of various material/detector parameters on the sensitivity of HgCdTe detectors. With this objective in mind, the numerical simulator, called MCTsim, is constructed with all possibly dominant g-r mechanisms (Auger, radiative, SRH and TAT) and detector noise sources (Johnson-Nyquist, g-r and $1/f$). The level of detail incorporated into the simulator, as well as the calculations carried up to the sensor detectivity level yield important observations enlightening some critical issues that should be taken into consideration by the detector designer. Therefore, we believe that the results presented in this thesis will complement the relevant information in the literature toward establishing the guides for the design of HgCdTe sensors.

As to our knowledge, this work is one of the most comprehensive simulation based investigations of the HgCdTe detector performance providing important results that can be used as a guide for optimization of the detector performance in order to meet the demanding requirements of the third generation thermal imagers.

Modeling approach used in our solver is explained in the next Chapter.

CHAPTER 3

MODELING APPROACH

Our objective in this study is to investigate the detector performance and sensitivity limiting mechanisms excluding the fabrication process related (generated) dark current/noise contributions. Therefore, the recombination-generation mechanisms incorporated into the simulation under dark conditions are SRH, Auger, radiative and TAT which are all directly related with the intrinsic material properties. The SRH and TAT mechanisms, resulting from the interaction of the charge carriers with the defect/impurity levels within the energy gap of the material, are not truly intrinsic processes. However, these levels are generally unavoidable and they are observable in the HgCdTe material at some level whatever the growth technique is. Therefore, we treat these mechanisms as unavoidable intrinsic processes affecting the ultimate detector performance and include them in the simulations with the commonly observed trap levels and densities (10^{13} - 10^{15} cm⁻³). Assuming that device processing steps such as hybridization with the read-out circuit do not introduce additional defects, the sensor performance is governed by the defects/impurities introduced during the growth of the device epilayer structure.

It should be noted that exact calculation of the HgCdTe detector performance under a specific combination of material composition and operating conditions is not possible even with numerical techniques due to insufficient and scattered information on some material parameters such as the trap levels, capture cross sections and carrier lifetimes, as well as field dependent transport properties. Therefore, the simulator of this work is constructed with the objective of observing the trends and the relations which would serve as a design guide for these sensors. While the geometrical effects can be modeled through 2D and 3D simulations, the main objective of this paper is to identify the relation between the intrinsic material parameters and the processes and the detector characteristics. Therefore, we

constructed a 1 D simulation which is reasonably compatible with the above described objectives

3.1. Introduction to Semiconductor Modeling and Simulation

Semiconductor modeling and simulation can be classified into three different branches which are inter-related: process, device and circuit simulation as in Fig. 3.1 [62]. *Process modeling/simulation* usually comes first and it refers to the simulation of the different fabrication steps such as implantation or diffusion [62]. Using the doping profile which is the output of the process modeling, the next level is employed which is *device modeling/simulation* [62]. In this case, we usually solve a set of fundamental physics equations in order to derive the electrical, optical or thermal properties of the device [62]. Using these device simulations, compact models for the devices can be created [62].

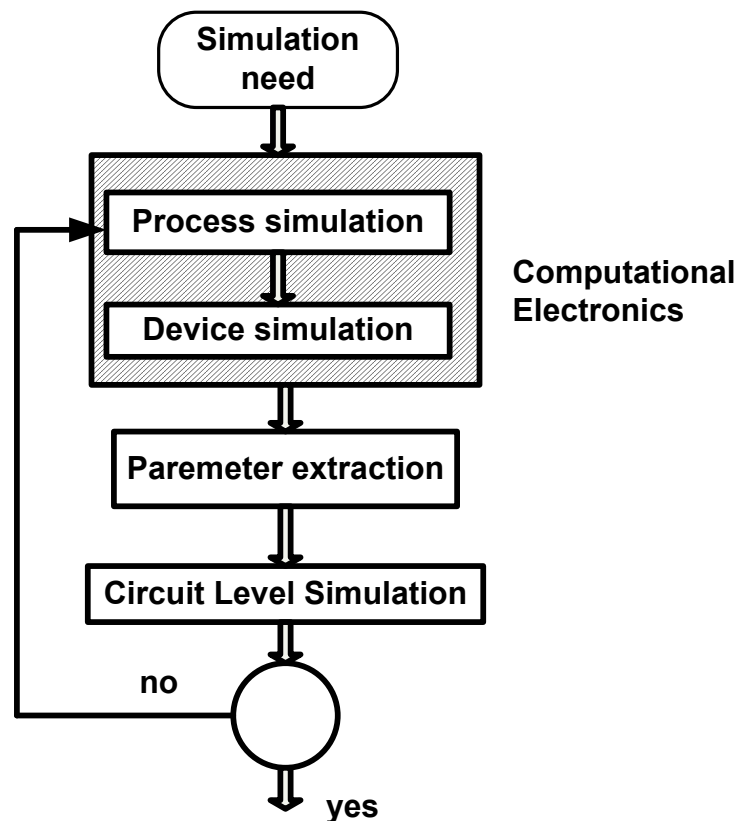


Figure 3.1 Design sequence to achieve simulation need [62]

The aim of *Computational Electronics* is to provide simulation tools with the necessary level of sophistication [63]. Fig. 3.2 shows the main components of semiconductor device simulation at any level [62]. There are two main parts, which must be solved self-consistently with one another, the transport equations governing charge flow, and the fields driving charge flow [62]. These are coupled strongly to one another, and must be solved simultaneously [62]. The fields originate from external sources, as well as the charge and current densities which act as sources for the time varying electric and magnetic fields obtained from the solution of Maxwell's equations [62]. Under appropriate conditions, only the quasi-static electric fields arising from the solution of Poisson's equation are necessary [62].

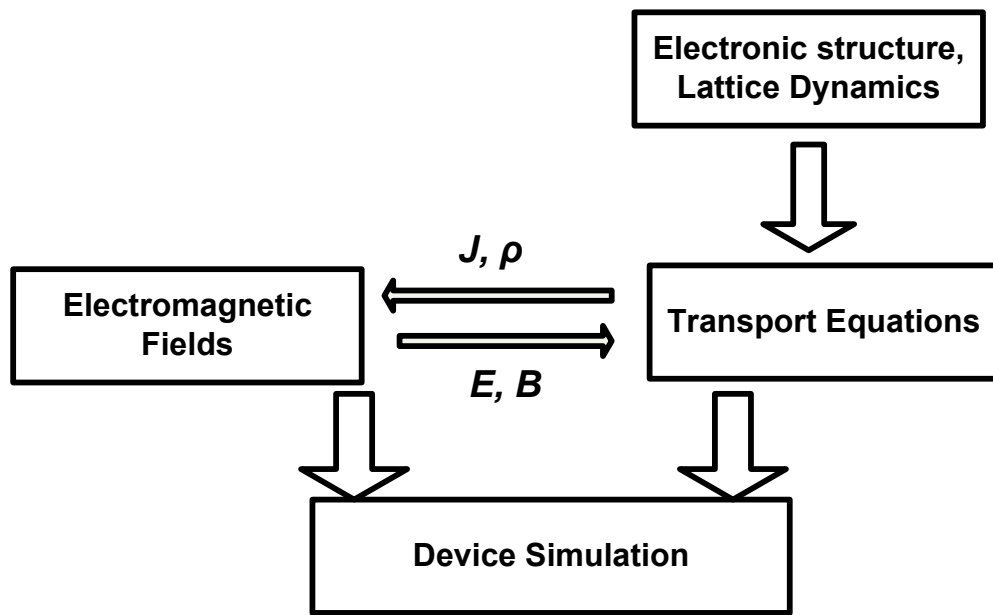


Figure 3.2 Description of the device simulation sequence [62]

The fields, in turn, are driving forces for charge transport as shown in Fig. 3.3 for the various levels of approximation within a hierarchical structure ranging from compact modeling at the top to an exact quantum mechanical description at the bottom [62].

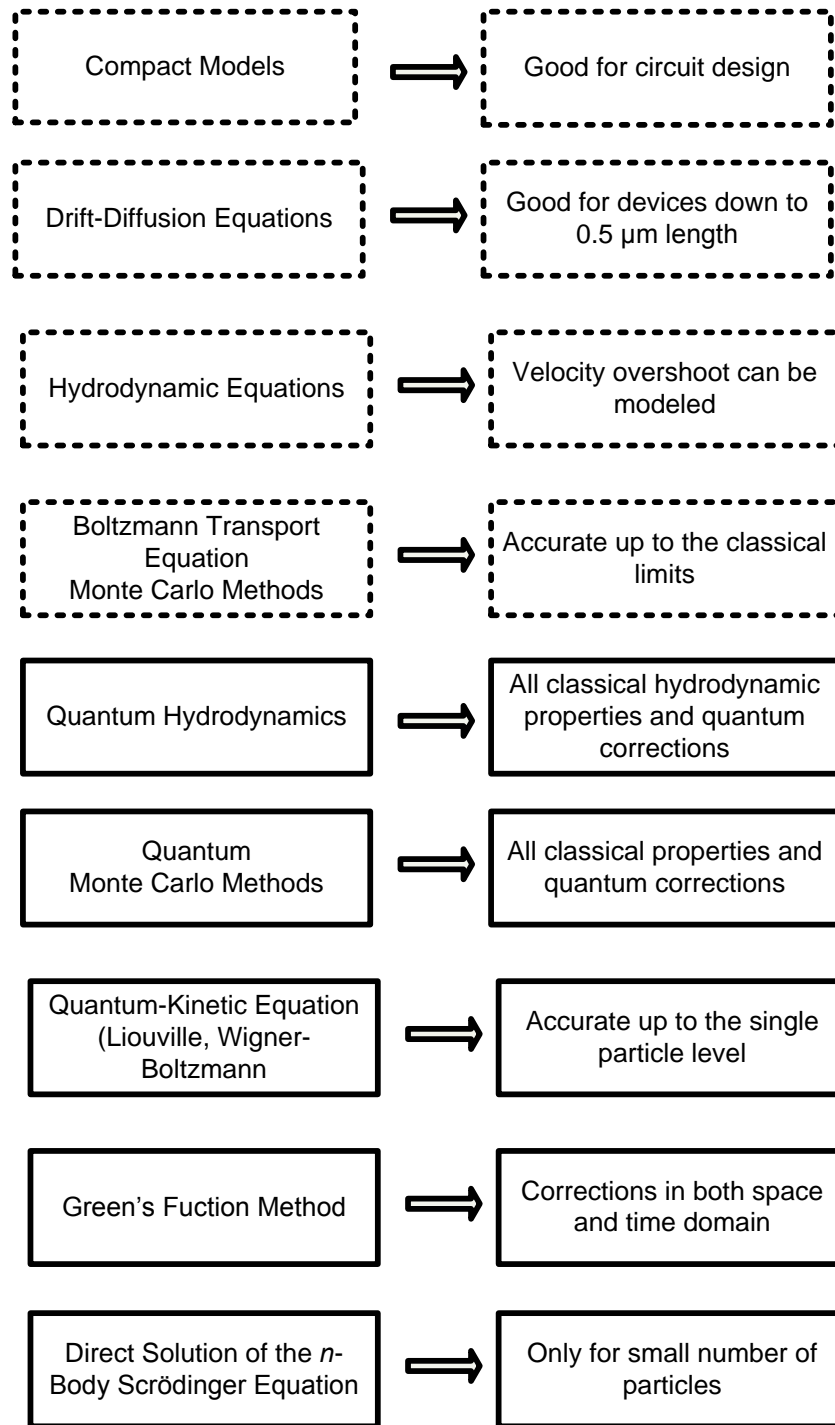


Figure 3.3 Transport models (the dotted-boxes are the semi-classical approaches and the solid-boxes are the quantum approaches) [62]

In this study, we are interested in device modeling and simulation applied to HgCdTe using Drift-Diffusion model.

3.2 Drift-Diffusion (DD) Model

Drift-diffusion (DD) model is widely used for the simulation of carrier transport in semiconductors. The complete drift-diffusion model is based on the following set of equations in 3 dimensional space and time.

3.2.1 Poisson's Equation

Electro-static behavior of the semiconductor devices are described by

$$\vec{\nabla} \cdot \epsilon \vec{\nabla} V = -q(p - n + N_d^+ - N_a^-) \quad (3.1)$$

where V is the electrostatic potential (volt), ϵ is the permittivity of the semiconductor (F/cm), p is the hole density (cm^{-3}), n is the electron density (cm^{-3}), N_d^+ is the ionized donor density (cm^{-3}) and N_a^- is the ionized acceptor density (cm^{-3}).

3.2.2 Continuity Equations

The continuity equations govern the conservation laws for the charge carriers, which are derived from the time dependent Boltzmann Transport Equation (BTE).

$$\begin{aligned} \frac{\partial n}{\partial t} &= \frac{1}{q} \nabla \cdot \vec{J}_n + (G - R), \\ \frac{\partial p}{\partial t} &= -\frac{1}{q} \nabla \cdot \vec{J}_p + (G - R) \end{aligned} \quad (3.2)$$

where $J_{n(p)}$ is the total electron (hole) current density and $G-R$ is the net generation minus recombination rate which will be discussed later.

As seen in Fig. 3.4, macroscopic water flow can be considered to resemble the microscopic drift-diffusion continuity equations illustrated in Fig. 3.5. The rate of increase of the water level in the lake corresponds to the partial time derivative of the carrier concentrations in the semiconductor device [62]. The speeds of these concentrations are dependent upon the rain, the evaporation and the net inflow of the water [62].

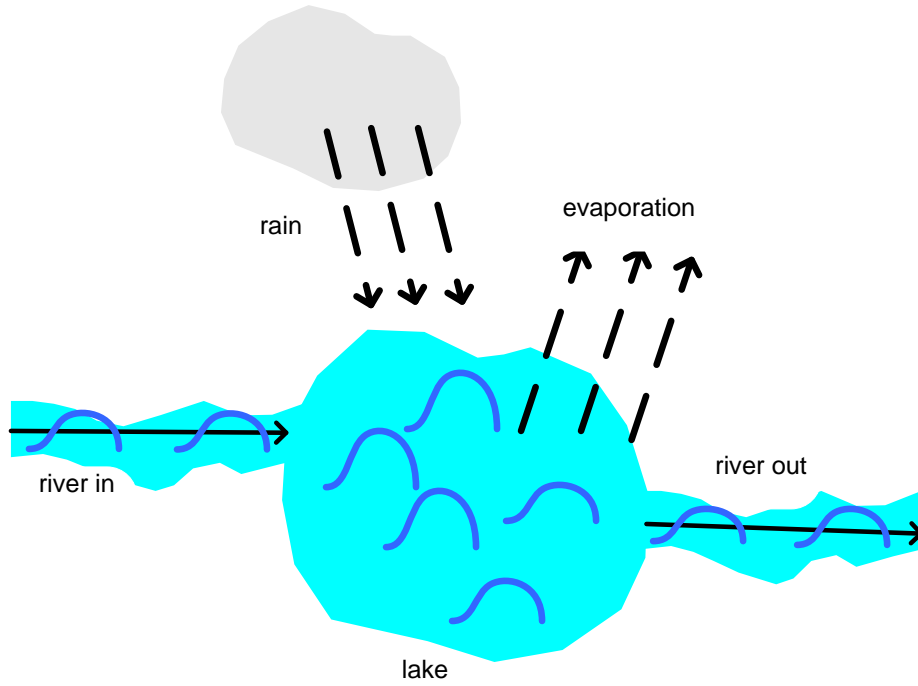


Figure 3.4 Macroscopic water flow similar to microscopic drift-diffusion continuity equations [62]

Rate of increase of the water level in the lake $\frac{\partial p}{\partial t}$	=	(inflow-outflow)+rain-evaporation $-\frac{1}{q} \vec{\nabla} \cdot \vec{J}_p + G - R$
---	---	---

Figure 3.5 Analogy of water flow [62]

3.2.3 Current Equations

Electron and hole current densities are separated into their components, which are drift part due to the Electric field and diffusion part due to the carrier concentration gradient as follows

$$\begin{aligned} \vec{J}_n &= \vec{J}_{n\text{drift}} + \vec{J}_{n\text{diffusion}} = q\mu_n n \vec{E} + qD_n \vec{\nabla} n, \\ \vec{J}_p &= \vec{J}_{p\text{drift}} + \vec{J}_{p\text{diffusion}} = q\mu_p p \vec{E} - qD_p \vec{\nabla} p \end{aligned} \quad (3.3)$$

where $\mu_{n,p}$ electron (hole) mobility, E is the Electric field (V/cm), and $D_{n,p}$ is the electron and hole diffusivity.

$$\vec{E} = -\vec{\nabla}V. \quad (3.4)$$

Einstein's relation is given by

$$D_{n,p} = \frac{k_b T}{q} \mu_{n,p} \quad (3.5)$$

where k_b is the Boltzmann's constant and T is the absolute temperature (K).

3.3 Transport Equations and Material Parameters for HgCdTe Device Modeling

In this study, one dimensional space and steady-state conditions are used for HgCdTe device modeling. In steady-state, time derivatives of $n(x)$ and $p(x)$ are zero. In these cases, following coupled nonlinear equations are obtained

Poisson's equation is

$$\frac{d^2V(x)}{dx^2} = V''(x) = -\frac{q}{\epsilon} [C(x) + p(x) - n(x)]. \quad (3.6)$$

Electron continuity equation is

$$\frac{dJ_n(x)}{dx} = q [R(x) - G(x)]. \quad (3.7)$$

Hole continuity equation is

$$\frac{dJ_p(x)}{dx} = -q [R(x) - G(x)]. \quad (3.8)$$

The unknowns are as follows

$n(x)$ is the electron concentration along the device (cm^{-3}),

$p(x)$ is the hole concentration along the device (cm^{-3}),

$V(x)$ is the electrostatic potential along the device (Volt).

The auxiliary equations are presented below.

Total electron current density (A/cm²) is

$$J_n = J_{ndrift} + J_{ndiffusion} = q\mu_n nE + qD_n \frac{dn}{dx}. \quad (3.9)$$

Total hole current density (A/cm²) is

$$J_p = J_{pdrift} + J_{pdiffusion} = q\mu_p pE - qD_p \frac{dp}{dx}. \quad (3.10)$$

Total current density is

$$J = J_n + J_p. \quad (3.11)$$

Doping profile (cm⁻³) is net donor (N_d) minus acceptor (N_a) doping density and given by

$$C(x) = N_d(x) - N_a(x). \quad (3.12)$$

μ_n and μ_p are electron and hole mobilities in $\left(\frac{cm^2}{V.s}\right)$. Theoretical hole mobility is

taken proportional to electron mobility, $\mu_p = 0.01\mu_n$ [52]. Theoretical expression of the electron mobility by Rosbeck *et al.* [64] is used as follows

$$\mu_n = \frac{9 \times 10^8 b}{T^{2a}} \quad (3.13)$$

where $a = (0.2 / x)^{0.6}$, $b = (0.2 / x)^{7.5}$.

The calculated mobilities at $x=0.226$ and $T=77K$ using these equations are 112,000 cm²/(V.s) for electrons and 1,120 cm²/(V.s) for holes, and are not consistent with the experimental data [65] which shows that μ_n is between 50,000 and 100,000 cm²/(V.s). Therefore, electron and hole mobilities in HgCdTe are scaled based on the experimental data [65] by keeping the electron to hole mobility ratio fixed at 166.5 as follows

$$\mu_{n,\text{modified}} = (0.446)\mu_n, \quad (3.14)$$

$$\mu_{p,\text{modified}} = (0.2678)\mu_p. \quad (3.15)$$

Now, μ_n is $50,000 \text{ cm}^2/(\text{V.s})$ and μ_p is $300 \text{ cm}^2/(\text{V.s})$ at 77 K and $x=0.226$ (i.e. $\lambda_c=10 \text{ }\mu\text{m}$).

ε , which equals to $\varepsilon_0.\varepsilon_r$, is the permittivity (dielectric constant) of the semiconductor (F/cm). ε_0 is the free-space permittivity and ε_r is the relative permittivity of the HgCdTe material. There are two relative dielectric constants for our study: Static (ε_r) and high frequency (ε_{r_hf}). Static one is used in the Poisson equation and the hf one is used in the radiative and Auger rate expressions. The expressions for the dielectric constants are given by [66], [67]

$$\varepsilon_r = 20.5 - 15.5x + 5.7x^2, \quad (3.16)$$

$$\varepsilon_{r_hf} = 15.2 - 13.7x + 6.4x^2. \quad (3.17)$$

3.4 Recombination-Generation Mechanisms

In continuity equations, $R(x)$ is total net recombination rate and $G(x)$ is total net generation rate. In HgCdTe p-n structure, applicable recombination-generation processes include Shockley-Read Hall (SRH), Auger, radiative, trap-assisted tunneling (TAT) and photogeneration. Description and mathematical modeling of these processes are introduced as follows.

3.4.1 SRH Recombination

The Shockley-Read-Hall (SRH) recombination mechanism emerges from the recombination of electron-hole pairs via defect levels within the energy band-gap of the material. Therefore, SRH is not an intrinsic process. The excess energy is released via phonon emission. Such defect levels in HgCdTe could be a result of vacancies, substitutional impurities, interstitial impurities, dislocations or grain boundaries [41]. They can be generated during HgCdTe growth, post-growth annealing treatments or during device processing [30]. The effect of this mechanism

on detector noise and detectivity can therefore be decreased as HgCdTe processing improves. However, considering state-of-the-art HgCdTe material and device processing, SRH is currently an essential recombination mechanism to take into account [66].

The SRH model uses non-degenerate statistics and assumes that there is a single localized recombination center located at an energy level E_t with the trap density N_t (cm^{-3}) [30]. The basic mechanisms are shown in Fig. 3.6 [68]. Four possible transitions may occur via the localized recombination center by which electrons and holes can be captured and emitted [40]. The localized trap state could either be empty or full. When it is empty, it can either capture an electron from the conduction band, as is shown in Fig. 3.6 (a) or it can emit a hole to the valence band, as is shown in Fig. 3.6 (d). When it is filled, there exist two possibilities. It can either emit the electron to the conduction band with an emission rate, as is shown in Fig. 3.6 (b), or capture a hole from the valence band, as is shown in Fig. 3.6 (c).

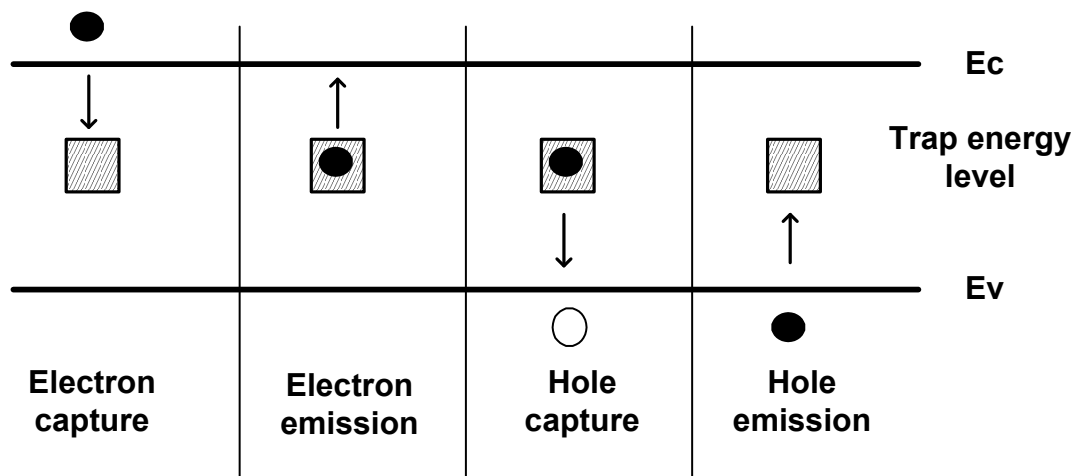


Figure 3.6 Schematic of SRH recombination [68]

The net SRH recombination rate is given by [41], [51]

$$R_{SRH}(x) = \frac{[n \cdot p - n_i^2]}{[\tau_p [n + n_1] + \tau_n [p + p_1]]} \quad (3.18)$$

where τ_n and τ_p are minority carrier lifetimes due only to SRH processes.

n_1 and p_1 are the electron and the hole concentrations respectively when the Fermi level is coincident with the trap level as follows

$$\begin{aligned} p_1 &= N_v \exp[-E_t / kT], \\ n_1 &= N_c \exp[-[E_g - E_t] / kT]. \end{aligned} \quad (3.19)$$

E_t is measured from the top of the valence band. N_c is the density of states of electrons in the conduction band and N_v is the density of states of heavy holes in the valence band given by [47], [48]

$$\begin{aligned} N_c &= 2 \left[3E_g kT / (8\pi P^2) \right]^{1.5} [1 + 4kT / E_g], \\ N_v &= 10^{-6} [2\pi m_{hh} kT]^{1.5} / [4(\pi\hbar)^3] \end{aligned} \quad (3.20)$$

where m_{hh} is the heavy hole effective mass, which equals to $0.55m_0$ [39] with m_0 being the electron mass in vacuum. The interband transition matrix element (P) is taken to be 0.83 eVnm (0.83×10^{-7} eVcm) [47].

3.4.2 Radiative Recombination

It is an intrinsic process which involves the direct band to band recombination of an electron in the conduction band with a hole in the valence band [30]. Photon is emitted during the recombination as shown in Fig. 3.7. This process is of central significance in direct band-gap semiconductors such as HgCdTe and is the basis of light emitting diodes [41]. In a non-degenerate semiconductor, the rate at which the electrons and holes are recombined depends simultaneously on the concentration of electrons in the conduction band and the availability of holes in the valence band [41].

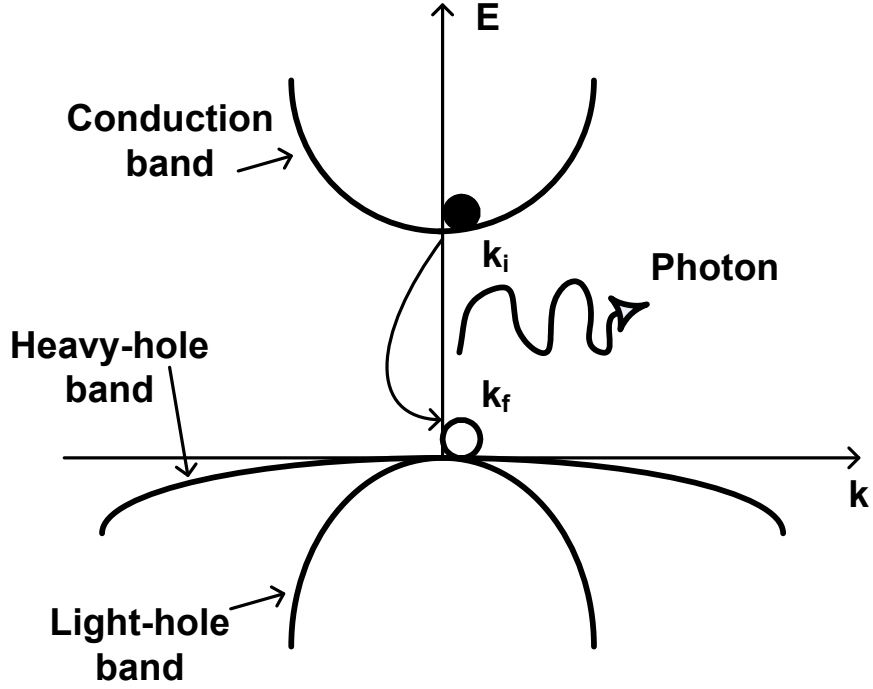


Figure 3.7 Illustration of radiative recombination [66]

The theoretical study of radiative recombination has been developed by van Roosbroeck and Shockley [69]. In our study, the radiative recombination rate in the HgCdTe photodiode is modeled by [41]

$$R_{rad}(x) = G_R [n \cdot p - n_i^2] \quad (3.21)$$

where G_R is the radiative recombination coefficient. G_R is expressed as [66], [67]

$$G_R = 5.8 \times 10^{-13} \epsilon_{r-hf}^{1/2} \left(\frac{m_0}{m_e + m_{hh}} \right)^{3/2} \left(1 + \frac{m_0}{m_e} + \frac{m_0}{m_{hh}} \right) \times \left(\frac{300}{T} \right) [E_g^2 + 3kTE_g + 3.75k^2T^2] \quad (3.22)$$

where m_e is the electron effective mass. Electron effective mass is modeled by [66]

$$m_e = \frac{m_0}{-0.6 + 6.333 \left(\frac{2}{E_g} + \frac{1}{E_g + 1} \right)}. \quad (3.23)$$

3.4.3 Auger Recombination

It is a nonradiative recombination process, which involves three particles. Typically, an electron and a hole will recombine in a band-to-band transition and will give off the resulting energy to another electron or hole [19]. Energized particle will lose energy through phonon emission within the atomic lattice. There are several Auger processes, but two Auger processes are important for HgCdTe [19]. These are Auger-1 process which is dominant in n-type HgCdTe and Auger-7 process which is dominant in p-type HgCdTe. Both processes are illustrated in Fig. 3.8 [41].

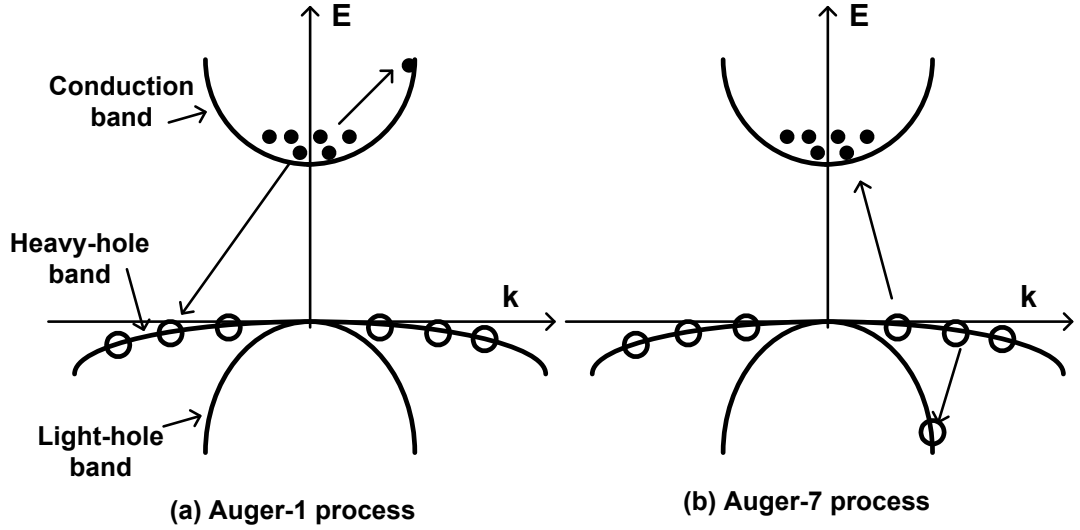


Figure 3.8 Dominant Auger processes in HgCdTe [41]

Auger recombination is modeled within this study as [41]

$$R_{Aug}(x) = [G_{Ae} \cdot n + G_{Ah} \cdot p] \cdot [n \cdot p - n_i^2] \quad (3.24)$$

where G_{Ae} and G_{Ah} are electron and hole Auger coefficients respectively. These coefficients are given by [66], [67]

$$G_{A_e} = \frac{\left(\frac{m_e}{m_0}\right) |F_1 F_2|^2}{2n_i^2 3.8 \times 10^{-18} \epsilon_{r_{hf}}^2 \left(1 + \frac{m_e}{m_{hh}}\right)^{\frac{1}{2}} \left(1 + 2 \frac{m_e}{m_{hh}}\right)} x \left(\frac{E_g}{kT}\right)^{-\frac{3}{2}} e^{\left[\frac{1 + 2 \frac{m_e}{m_{hh}} \frac{E_g}{kT}}{1 + \frac{m_e}{m_{hh}}}\right]}, \quad (3.25)$$

$$G_{A_h} = G_{A_e} \left[\frac{1 - \frac{3E_g}{kT}}{6 \left(1 - \frac{5E_g}{4kT}\right)} \right] \quad (3.26)$$

where $|F_1 F_2|$ is the overlap integral and is in the range 0.1-0.3 [50].

3.4.4 Mathematical Modeling of Trap Assisted Tunneling (TAT)

Traps in the depletion region play important role in degrading low-band gap detector (such as HgCdTe) performance. As shown in Fig. 3.9, the existence of electric field in the depletion region causes two non-thermal (horizontal) transitions: tunneling of electrons from the valence band to the traps and tunneling from the traps to the conduction band.

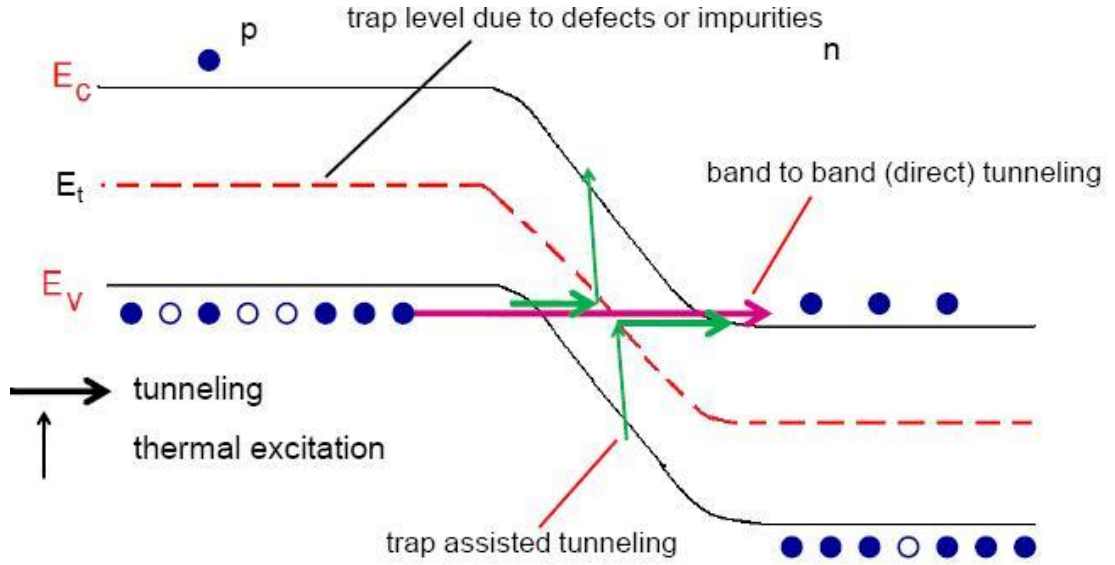


Figure 3.9 Schematic of tunneling mechanisms [3]

Tunneling from valence band to conduction band is called direct or band-to-band tunneling (BTB), which is dominant in large reverse bias voltages [19]. Since our study involves low and moderate reverse-bias of HgCdTe, we did not include BTB in our model. Trap-assisted tunneling (TAT), shown in green color in Fig. 3.9, is the dominant dark current mechanism under large and moderately large reverse bias voltages [70]. Also, TAT current may be the dominant dark current component in low bandgap diodes (especially LWIR and VLWIR) at low temperatures where the thermally generated current components (diffusion and g-r) are small [3]. Since there is a correlation between TAT current and $1/f$ noise, even negligible TAT current due to traps may degrade detector performance [71]. Therefore, modeling the TAT rate is extremely important for HgCdTe.

In the literature, limited amount of work [47], [48] has been performed for detailed mathematical modeling of the TAT rate, which can be embedded into the continuity equations for numerical analysis. We adapt following expressions for TAT rate [47], [48], [71]

$$R_2 = N_t \left[n \cdot p - n_i^2 \right] \left[W_v \cdot W_c \cdot e^{\frac{E_g}{kT}} + W_c \cdot \gamma_v \cdot e^{\frac{(E_g - E_t)}{kT}} + W_v \cdot \gamma_c \cdot e^{\frac{E_t}{kT}} + \gamma_c \cdot \gamma_v \right], \quad (3.27)$$

$$R_3 = [p(x) + p_1] \cdot \gamma_v + [n(x) + n_1] \cdot \gamma_c + \left[n(x) e^{\frac{(E_g - E_t)}{kT}} + N_c \right] \cdot W_c + \left[p_{lh}(x) e^{\frac{E_t}{kT}} + N_{vlh} \right] \cdot W_v, \quad (3.28)$$

$$R_{TAT} = \frac{R_2}{R_3} \quad (3.29)$$

where N_{vlh} is the density of states of light holes in the valence band (cm^{-3}) which is taken approximately equal to N_c [47]. E_t is the trap energy measured from the valence band in eV. N_t is the trap density. $p = p_{hh} + p_{lh}$ (hh: heavy hole, lh: light hole). Light holes are responsible for tunneling since mass of light hole is small and tunneling rate is large. In our study, p_{lh} is taken approximately to be $(N_{vlh}/N_{vhh})p$.

Tunnel capture constants are given by [71]

$$W_c = \frac{6 \times 10^5 E}{N_c (E_g - E_t)} \cdot \exp \left[\frac{-1.7 \times 10^7 E_g^{1/2} (E_g - E_t)^{3/2}}{E} \right], \quad (3.30)$$

$$W_v = \frac{6 \times 10^5 E}{N_v E_t} \cdot \exp \left[\frac{-1.7 \times 10^7 E_g^{1/2} E_t^{3/2}}{E} \right]. \quad (3.31)$$

Thermal capture constants are expressed as [48]

$$\gamma_c = \frac{1}{\tau_n N_t}, \quad (3.32)$$

$$\gamma_v = \frac{1}{\tau_p N_t}.$$

In our study, $q(V_{bi} - V_a) > E_g$ is almost satisfied in the range of all reverse biases and the Cd mole fractions taken into consideration. Therefore, the TAT/SRH R-G mechanism can be separated into three different mechanisms in the depletion region ($0 < x < W$) as shown in Fig. 3.10. These mechanisms are modeled as follows [71]

$$U_c = \frac{R_2}{R_3} | W_c = 0, \quad 0 < x < x_1, \quad (3.33)$$

$$U_d = R_{TAT} = \frac{R_2}{R_3}, \quad x_1 < x < x_2, \quad (3.34)$$

$$U_a = \frac{R_2}{R_3} | W_v = 0, \quad x_2 < x < W \quad (3.35)$$

where x_1 and x_2 are the turning points of the tunneling [47]. These points are expressed by [71]

$$x_1 = W \left(\frac{E_g - E_t}{q(V_{bi} - V_a)} \right) \quad (3.36)$$

$$x_2 = W \left(1 - \frac{E_t}{q(V_{bi} - V_a)} \right) \quad (3.37)$$

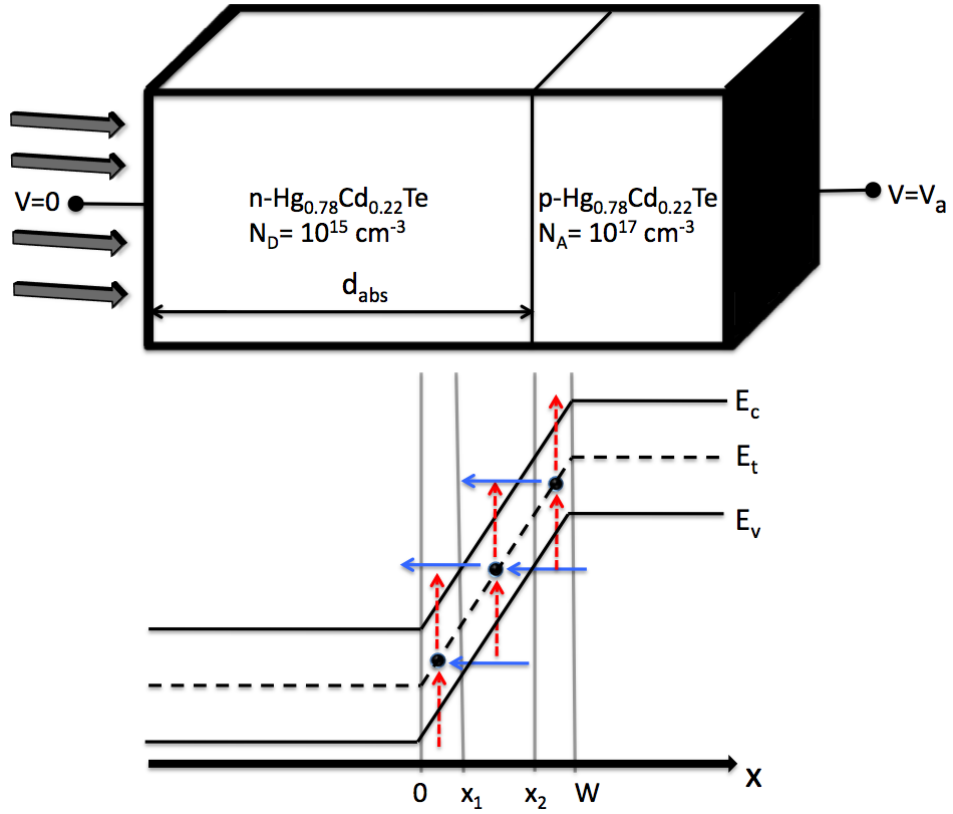


Figure 3.10 Simulated structure and the possible thermal and thermal assisted tunneling transitions [71] in different portions of the depletion region of the device. Dashed and solid arrows represent thermal and tunnel transitions, respectively

3.4.5 Lifetime Modeling

Minority carrier lifetime is an important parameter for HgCdTe device modeling and simulation. In our study, lifetime is incorporated into the SRH and TAT R-G expressions. Electron (hole) lifetime is modeled as follows [72]

$$\tau_{n(p)} = \frac{1}{\gamma_{n(p)} N_t}, \quad (3.38)$$

$$c_{n(p)} \text{ or } \gamma_{n(p)} = \sigma_{n(p)} v_{th,e(p)}, \quad (3.39)$$

$$v_{th,e(p)} = \sqrt{\frac{3kT}{m_{e(h)}^*}} \quad (3.40)$$

where N_t is the trap density, c_n or γ_n is the electron capture coefficient, c_p or γ_p is the hole capture coefficient, v_{th} is the electron/hole thermal velocity and σ_n and σ_p are the electron and hole capture cross-sections.

Deep levels may be related to the impurities, dislocations and defects during the fabrication of the p-n junction. These levels are called ‘traps’. Traps affect the photodiode performance. Especially, SRH and TAT R-G mechanisms are changed according to these trap characteristics. Traps are characterized by three parameters: trap density (N_t), trap energy level with respect to top of the valence band (E_t) and electron/hole capture cross sections (σ_n/σ_p).

In the literature, there is very limited deep level transient spectroscopy (DLTS) data for p on n HgCdTe ($x \approx 0.2$) detector [72], [73]. Most works have been focused on extraction of these trap parameters by analytical fitting using the experimental data [74], [75]. In our study, we examine the effects of varying trap parameters on the performance of HgCdTe photodiode by numerical method which is more reliable and exact over analytical methods. Measured trap capture cross sections in HgCdTe are ranged from 10^{-18} to 10^{-14} cm^2 [73]. We fix both electron and hole capture cross sections to 10^{-16} cm^2 , and change E_t and N_t in the simulations in order to observe their effects on the performance.

3.4.6 Mathematical Modeling of Photogeneration Rate

The photogeneration rate is given by [41]

$$G_f(x) = F_f \alpha \eta e^{-\alpha x} \left[\frac{\# \text{ of } EHP}{(cm^3 .s)} \right] \quad (3.41)$$

where x is the distance, F_f is the incident photon flux, α is the absorption coefficient and η is the quantum efficiency. In HgCdTe, η is approximately 1 [41].

3.5 MCTsim Numerical Solver for HgCdTe Photodiode Simulation

3.5.1 Boundary Value Problem

Ordinary differential equations (ODEs) describe physical phenomena changing continuously [63]. They are used in models throughout mathematics, science and engineering [63]. A system of ODEs has many solutions. A solution of interest is generally determined by specifying the values of all its components at a single point $x=a$. This describes initial value problem (IVP) [62]. But, in many applications a solution is determined in a more complicated way. Boundary Value Problem (BVP) involves values or equations for solution components at more than one x . Unlike IVP problems, a BVP may not have a solution, or may have a finite number, or may have infinitely many [76].

To solve a BVP, we need to provide an initial guess for the solution. The quality of our initial guess can be critical to the solver performance, and to being able to solve the problem at all. However, coming up with a sufficiently good guess can be the most challenging part of solving a BVP [63]. Certainly, we should apply the knowledge of the problem's physical origin. Often a problem can be solved as a sequence of relatively simpler problems, i.e., a *continuation* [62].

In our study, one dimensional Poisson and continuity equations form a BVP for investigation of HgCdTe photodiode. We use MATLAB language to solve numerically the coupled nonlinear Poisson and continuity equations. As shown in Fig. 3.11, we have developed a numerical solver named as 'MCTsim', which will be introduced in the next sections.

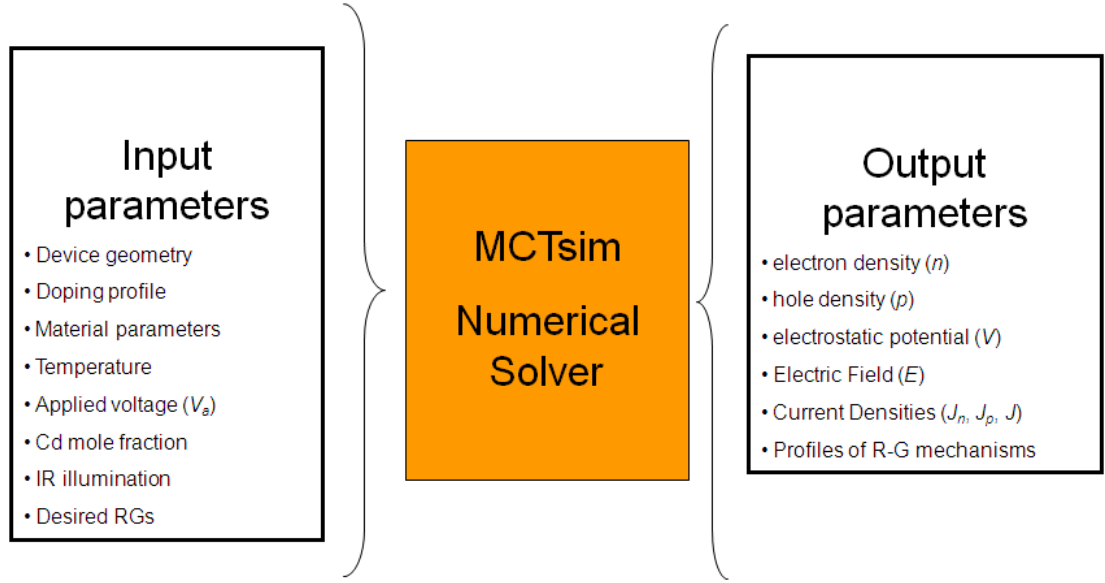


Figure 3.11 MCTsim numerical solver

3.5.2 Scaling Transport Equations for MCTsim

Main expressions (Poisson and electron/hole continuity) are given in Eqs. (3.6) to (3.8). Auxiliary equations are presented in Eqs. (3.9) to (3.12). In the continuity equations, $R-G$ represents net SRH, radiative, Auger, TAT and photogeneration rates which are mathematically modeled in the previous sections. We see that there are three nonlinear second order coupled ODEs (Poisson and electron/hole continuity). There are also three unknowns, which are n , p and V .

Since photodiode unknowns (n , p , V) may vary by many orders of magnitude from one to another (as well as throughout the solution domain), these variables should be appropriately scaled in order to aid in the numerical analysis of semiconductor equations [63]. In order for the scaling to be useful, the variables (parameters) should be scaled according to their intrinsic or characteristic values given in Table 3.1. After scaling using following scaling constants, the dimensionless variables are typically of the order of unity [63].

Table 3.1 Scaling values [63].

Value	Parameter
$x_0=D$	distance scaling (cm)
$T_0=T$	temperature scaling (K)
$V_0=V_t=k_b T/q$	electrostatic-potential scaling (V)
$C_0=\max(N_a, N_d)$	concentration scaling (cm ⁻³)
$D_0=6.6$	diffusion-coefficient scaling (cm ² /s)
$u_0=D_0/V_0$	mobility-coefficient scaling (cm ² /V/s)
$R_0=D_0*C_0/(x_0^2)$	recomb./gen. rate scaling (cm ⁻³ /s)
$GR_0=D_0/(x_0^2*C_0)$	radiative recomb. coeff. scaling (cm ³ /s)
$GA_0=D_0/(x_0^2*C_0^2)$	Auger e/h coeff. scaling (cm ⁶ /s)
$t_0=(x_0^2)/D_0$	time scaling (s)
$E_0=V_0/x_0$	electric-field scaling (V/cm)
$J_0=q*D_0*C_0/x_0$	current-density scaling (A/cm ²)
$L_0=V_0*\epsilon_0/(q*(x_0^2)*C_0)$	Laplacian scaling constant

If we substitute Eqs. (3.9) to (3.12) into the main equations, Eq. (3.6) to (3.8), and make scaling, we obtain the following scaled coupled ODEs. Note that all unknowns and R - G s are varying in one dimensional space (x). “'” represents the first derivative w.r.t x and “''” represents the second derivative w.r.t x .

Scaled Poisson's equation is

$$\frac{d^2V}{dx^2} = V'' = \frac{n - p - C}{L_0 \epsilon_r} \quad (3.42)$$

where L_0 is the Laplacian scaling constant. $C=C(x)=N_d(x)-N_a(x)$ is the scaled net doping profile.

Scaled electron continuity equation is as follows

$$J_n' = R - G = \left[\mu_n \left[-nV' + n' \right] \right]', \quad (3.43)$$

$$n'' - n'V' - nV'' = \frac{R - G}{\mu_n} \quad (3.44)$$

where μ_n is the scaled electron mobility.

Scaled hole continuity equation is as follows

$$J_p' = -[R - G] = [\mu_p [-p^* V' - p']]', \quad (3.45)$$

$$p'' + p' V' + p V'' = \frac{R - G}{\mu_p} \quad (3.46)$$

where μ_p is the scaled hole mobility.

3.5.3 Ordinary Differential Equations of MCTsim

If we arrange scaled equations, we obtain the following coupled, nonlinear, second-order and scaled three ODEs with three scaled unknowns (n, p, V)

$$V'' = \frac{n - p - C}{L_0 \epsilon_r}, \quad (3.47)$$

$$n'' = n' V' + n V'' + \frac{R - G}{\mu_n}, \quad (3.48)$$

$$p'' = -p' V' - p V'' + \frac{R - G}{\mu_p}. \quad (3.49)$$

To solve above ODEs in the MATLAB environment with finite difference code, we need to reduce them to the first order ODEs as follows

$$\begin{aligned} n' &= r, \\ p' &= s, \\ V' &= w, \\ w' &= \frac{n - p - C}{L_0 \epsilon_r}, \\ r' &= n' V' + n V'' + \frac{R - G}{\mu_n}, \\ s' &= -p' V' - p V'' + \frac{R - G}{\mu_p}. \end{aligned} \quad (3.50)$$

Now, we have coupled, nonlinear, first-order and scaled six ODEs with six unknowns (n, p, V, r, s, w). MCTsim solver is implemented to solve this equation set in the MATLAB environment.

3.5.4 Program Architecture of MCTsim

As shown in Fig. 3.12, MCTsim consist of a main programme and 3 sub-programs to solve the scaled ODEs.

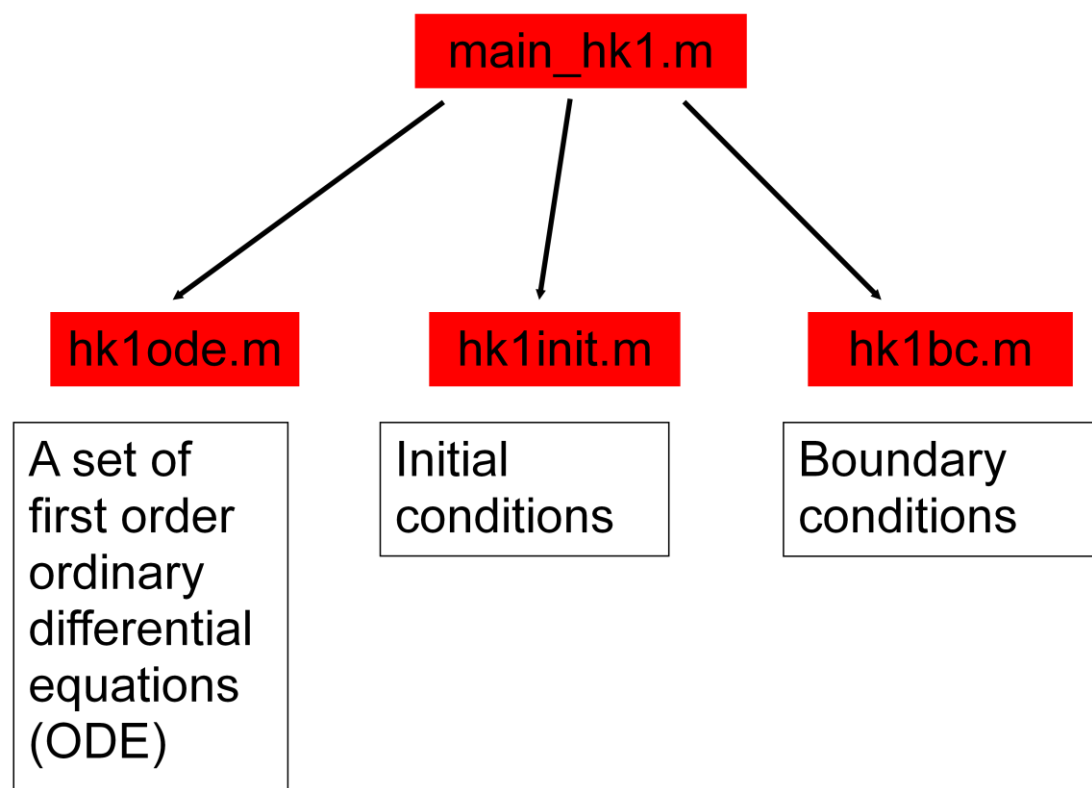


Figure 3.12 MCTsim architecture

3.5.5 Purpose of hk1ode

Purpose of this program is to obtain the discretized ODE set as shown in Fig. 3.13.

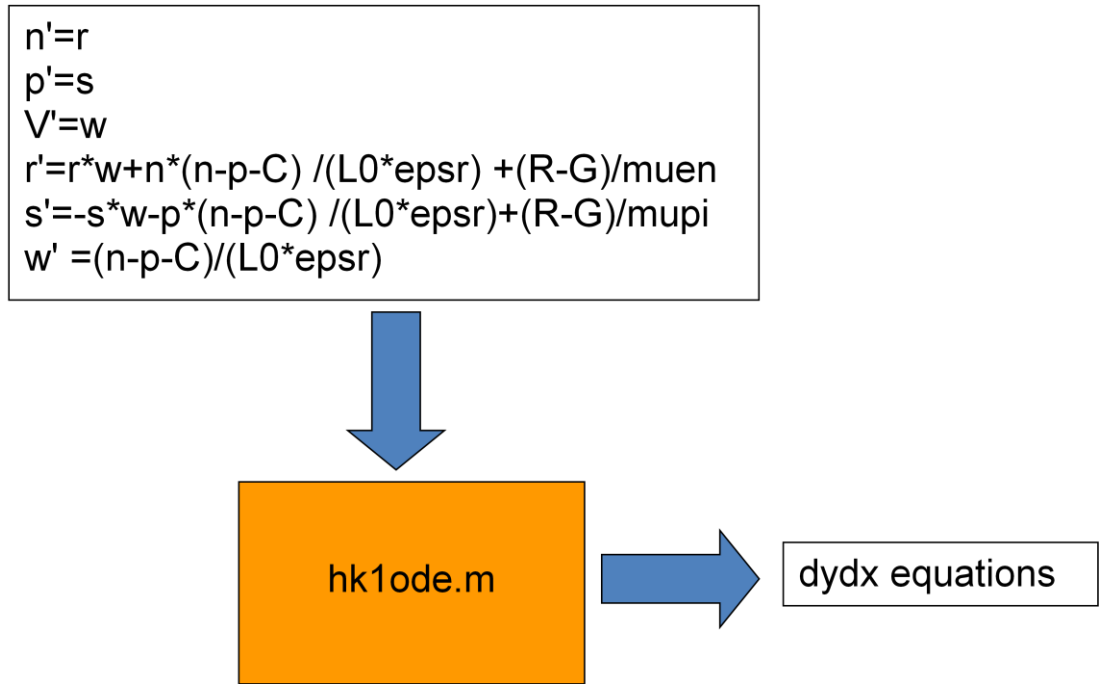


Figure 3.13 Purpose of hk1ode

3.5.6 Purpose of hk1init

Initial conditions (ICs) are very important for numerical solution of nonlinear ODEs [63]. The more close ICs to the true solution, the fast, the more stable and the more exact is the solution [67]. However, for complex BVP problems like in this study, expressing good ICs is not so easy. Therefore, we used continuation method. As seen in Fig. 3.14, the rough ICs are obtained with sine and cosines, and MCTsim is run. Then, the output of MCTsim is fed as an input until desired accuracy and stability is reached.

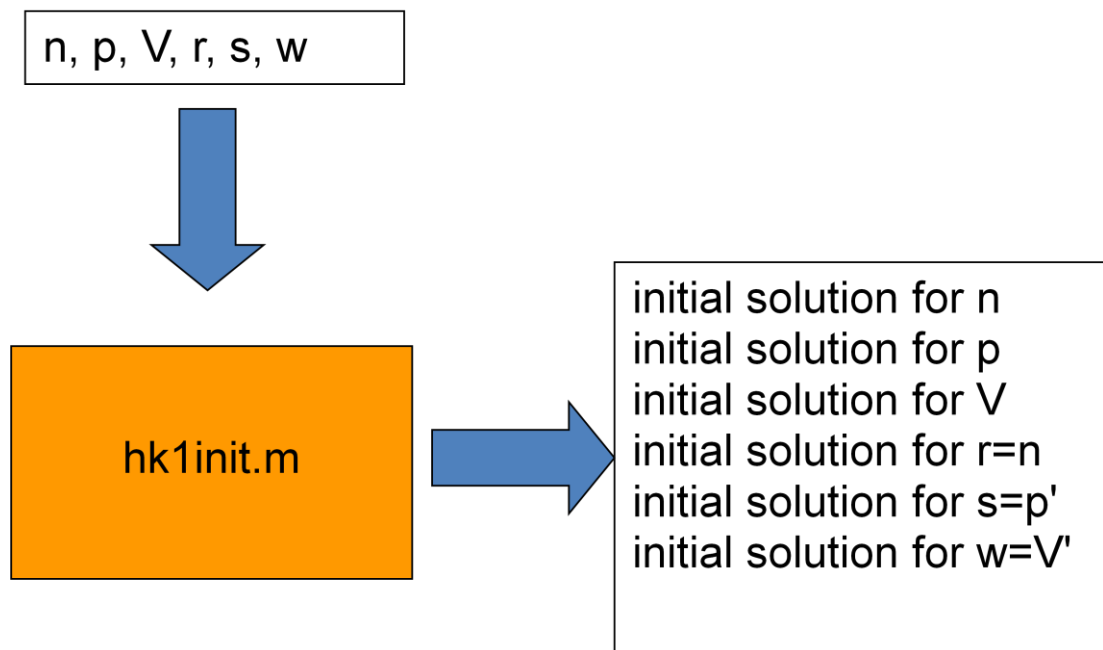


Figure 3.14 Purpose of `hk1init`

3.5.7 Study of Boundary Conditions for MCTsim

Since our study involves BVP as modeled in Fig. 3.15, there are two boundaries in a photodiode, which are the device end points, or terminals, or contacts as in Fig 3.16. These are at $x=0$ and $x=D$ (device length). These contacts are supposed to show ohmic behavior.

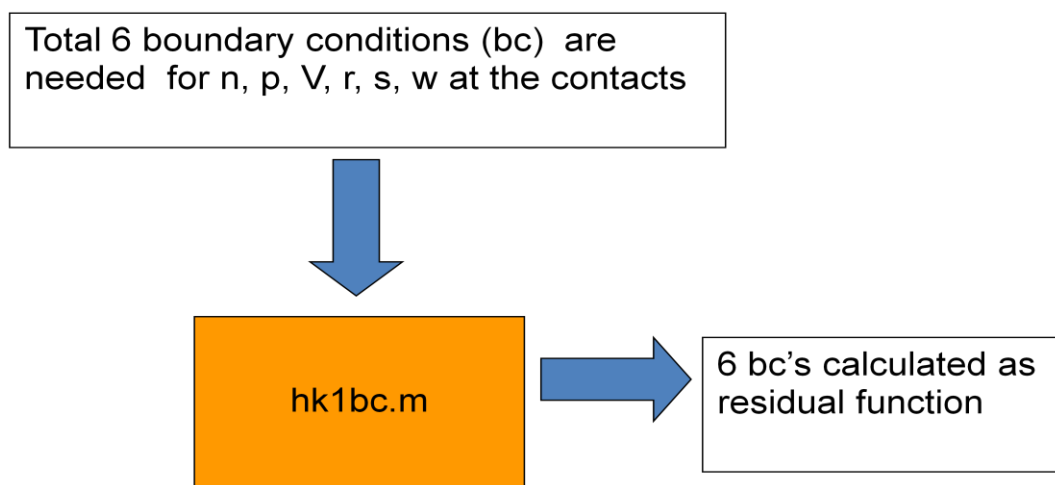


Figure 3.15 Purpose of `hk1bc`

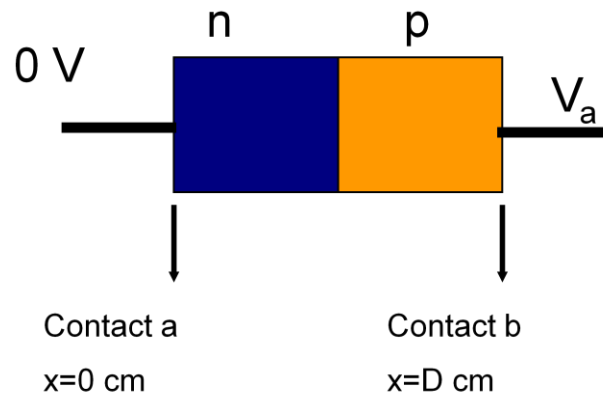


Figure 3.16 Boundaries of photodiode (V_a is the applied bias voltage)

For six unknowns, six boundary conditions (bcs) are needed. These are obtained by applying charge neutrality at the contacts. The potential at contact ‘a’ is set equal to zero. The ohmic contacts have been considered to be abrupt with infinitely large surface recombination velocity.

3.5.8 Program Validation

During the code development of the MCTsim, the simulation code has been checked by simulating silicon diodes and comparing the results with those of the commercial software [63] as well as comparing the outputs of the HgCdTe photodetector simulations with those of the analytical approaches.

Next Chapter uses our numerical solver to deeply investigate and optimize the photo-electrical properties of p^+n homojunction HgCdTe LWIR and VLWIR photodiodes operating at 77 K.

CHAPTER 4

SIMULATION RESULTS AND DISCUSSION

p⁺-n HgCdTe photodiode performance at 77 K needs to be investigated in a more comprehensive way. In this Chapter, we perform several simulations to understand the behavior of p⁺-n HgCdTe photodiode performance at 77 K in the LWIR and VLWIR bands.

4.1 Material Parameters and Simulation Strategy

The main objective of the simulations is to identify the individual and combined effects of various material/detector parameters on the sensitivity of HgCdTe detectors.

The simulation parameters are given in Table 4.1. The detector structure utilized in this work is shown in Fig. 4.1. The simulated structure is a homojunction p on n pixel with dimensions of 25x25 μm^2 which is typical for a LWIR focal plane array. The sensor is exposed to the IR radiation with an optical aperture of f/2 through a filter with a cut-in wavelength of 8 μm in order to account for atmospheric attenuation of the radiation. The detector is assumed to have perfect anti-reflection coating. The p-type doping density (N_a) is not expected to have significant effect on the sensor performance as long as it is kept in the range typically utilized for LWIR HgCdTe detectors. Therefore, we keep this parameter fixed at $1 \times 10^{17} \text{ cm}^{-3}$. We have used Hougen formulation [77] for the absorption coefficient given as $\alpha = 100 + 5000x$ (cm^{-1}). The electron and hole mobilities are scaled based on the experimental data [65].

Table 4.1 Simulation parameters.

Parameter	Value
Pixel dimensions	25 μm x 25 μm
d_{abs}	variable in the range of 2 to 20 μm
λ_c (cut-off wavelength)	variable in the LWIR and VLWIR bands
Cut-in wavelength of the detector filter	8 μm
N_d	10^{15} cm^{-3}
N_a	10^{17} cm^{-3}
T	77 K
N_t	variable in the range of 10^{13} to 10^{15} cm^{-3}
E_t	variable in the range of $0.5E_g$ to $0.8E_g$
σ_n, σ_p	10^{-16} cm^2
τ_n	1.63 μs @ $N_t=10^{14} \text{ cm}^{-3}$
τ_p	12.5 μs @ $N_t=10^{14} \text{ cm}^{-3}$
μ_n	50,000 $\text{cm}^2/(\text{V.s})$ @ $\lambda_c=10 \text{ }\mu\text{m}$ and $T=77\text{K}$
μ_p	300 $\text{cm}^2/(\text{V.s})$ @ $\lambda_c=10 \text{ }\mu\text{m}$ and $T=77\text{K}$
L_n	232.8 μm @ $\lambda_c=10 \text{ }\mu\text{m}$ and $T=77\text{K}$
L_p	50 μm @ $\lambda_c=10 \text{ }\mu\text{m}$ and $T=77\text{K}$
n_i	$5.34 \times 10^{12} \text{ cm}^{-3}$ @ $\lambda_c=10 \text{ }\mu\text{m}$ and $T=77\text{K}$
α	1230 cm^{-1} @ $\lambda_c=10 \text{ }\mu\text{m}$
$f/\#$	2
Background Temp.	300 K

The ohmic contacts have been considered to be abrupt with infinitely large surface recombination velocity. While there exist approaches to decrease the recombination at the contacts by utilizing minority carrier repelling structures [44], this issue is beyond the scope of the discussion in this thesis.

Thermal (Johnson), g-r (including photon noise) and $1/f$ noise mechanisms are included in the calculation of the specific detectivity. It has been assumed that the noise measurement frequency is 1 kHz unless stated otherwise. While $1/f$ noise was usually ignored in the previous work, this noise mechanism is generally one of the dominant sensitivity degrading mechanisms [71] and it should be taken into account in the assessment of the LWIR HgCdTe detectors. The empirical data provided by Nemirovsky and Unikovsky [20] for HgCdTe detectors is useful to establish the relation between the trap assisted tunneling current and the $1/f$ noise current spectral density as follows

$$i_{n1/f} = \alpha \frac{I_{TAT}^\beta}{\sqrt{f}} \quad (4.1)$$

where $\alpha=1 \times 10^{-6}$, $\beta=0.5$ and I_{TAT} is the TAT component of the sensor current [20]. The above relation between the TAT current and $1/f$ noise with similar α and β values was also observed in InSb and InAsSb photodiodes on alternative substrates [78], [79]. The expressions for the other noise currents, which are presented in section 1.4, are well known.

The simulations performed in this work can be classified into three groups. The first group of the simulations includes those on varying cut-off wavelength (9-14 μm sensors) with N_t , E_t and d_{abs} fixed at typical levels. The target of this simulation group is to identify the degree of variation in the sensor performance with the cut-off wavelength including the effects of the TAT mechanism which have usually been ignored in the previous numerical work.

The second group includes near-zero bias (slight-reverse bias) simulations carried out with the cut-off wavelength fixed at 10 and 14 μm and the absorber layer thickness (d_{abs}) at 8 μm . In this group of simulations, we have varied the trap density (N_t) and the trap level (E_t) in the ranges of 10^{13} - 10^{15} cm^{-3} and 0.5 - $0.8E_g$, respectively.

The objective of these simulations is to extract the dependence of LWIR and VLWIR sensor performance on the characteristics of the traps observed in the HgCdTe material. Unfortunately, there exists very limited amount of deep level transient spectroscopy (DLTS) data for p on n HgCdTe ($x \approx 0.2$) detectors [73]. Capture cross section measurements in a very wide range (10^{-18} to 10^{-11} cm²) have been reported [73]. We fixed both electron and hole capture cross sections at 10^{-16} cm² in the simulations of this work. Due to some lacking experimental information on the material properties related with the trapping and trap assisted tunneling characteristics of HgCdTe, this work targets qualitative rather than quantitative conclusions in this sense. However, noting that there is very limited amount of data in the literature relating the sensor performance to N_t and E_t , the amount of detail incorporated into this numerical work is expected to yield some useful conclusive observations, especially for the sensors grown under lattice mismatched conditions.

The third simulation group targets the identification of the effect of the absorber layer thickness and Auger mechanism on the sensor performance.

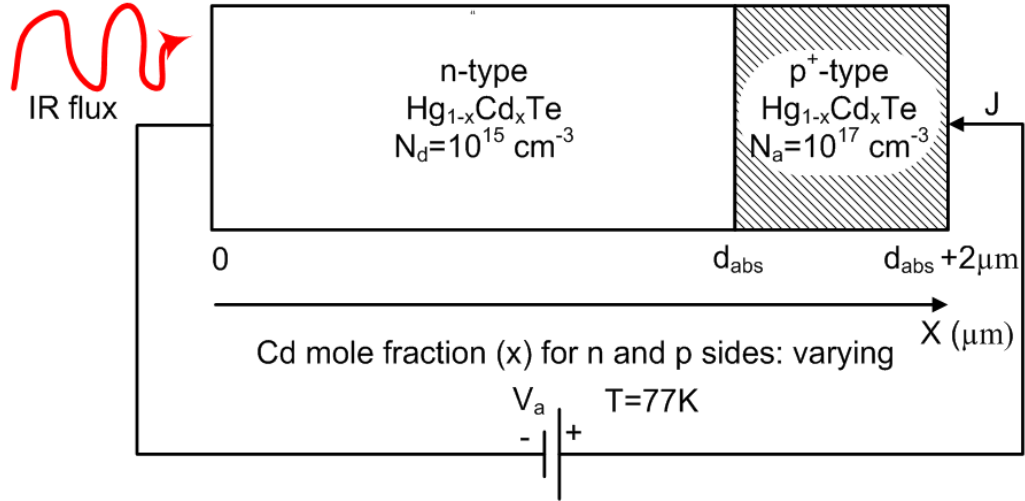


Figure 4.1 Simulated device geometry

As seen in Fig. 4.2, the solver (MCTsim) is run with different trap parameters, cut-off wavelength, temperature, and applied bias as input under dark and illuminated conditions using the simulation parameters. R-G mechanisms may be totally applied or selectively applied to see the effects and interactions of these mechanisms. Output of the solver is post-processed using another code written in MATLAB and desired performance parameters are visualized which will be presented in the next sections.

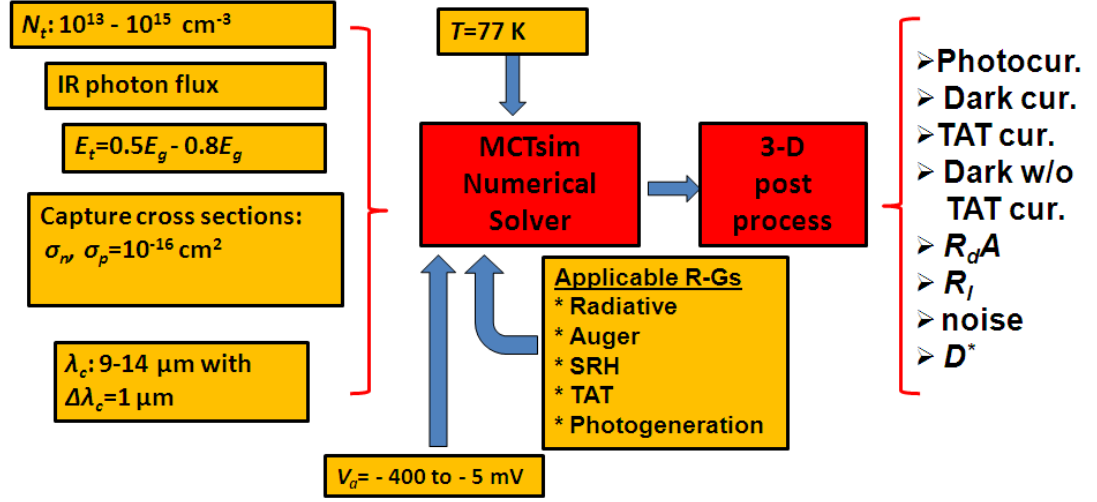


Figure 4.2 Workflow of the simulations

4.2 Effects of G-R Mechanisms versus Cut-Off Wavelength

Fig. 4.3 shows the contribution of various G-R mechanisms to the dark current of a $25 \times 25 \text{ } \mu\text{m}^2$ pixel under 25 and 100 mV reverse bias voltages. Each current component is extracted by calculating the difference between the sensor dark currents when the corresponding G-R mechanism is turned on and off in the simulation. This approach facilitates the comparison of the relative importance of each mechanism in determining the sensor dark current level. Auger mechanism establishes the most significant component of the dark current under all material compositions of interest. The obtained results in the case of Auger limited diodes deviate from the prediction of Rule 07 [80] by a factor varying in the range 2-4 which is acceptable since this rule is extracted from the measurements on diodes with presumably more advanced structures and somewhat different material properties.

As seen in Fig. 4.3, relative contribution of the TAT mechanism to dark current increases faster than that of the Auger process with increasing cut-off wavelength. However, TAT related component of the dark current remains insignificant throughout the entire cut-off range under low reverse bias. On the other hand, the relative contribution of the SRH mechanism to the dark current increases at a slower rate (with respect to Auger process) with increasing sensor cut-off wavelength making this G-R mechanism a more significant dark current contributor at the low cut-off end of the LWIR imaging band under the simulation conditions.

It should be noted that the contribution of the TAT mechanism to the dark current may not be visible through dark current fitting process at low reverse bias resulting in a conclusion that the diode performance is diffusion limited. However, the TAT mechanism establishes the most significant noise contributor at a frequency as high as 1 KHz for cut-off wavelengths above $11 \text{ } \mu\text{m}$ as demonstrated in Fig. 4.4 showing the squared magnitude of the noise current spectral density due to TAT and other g-r (including photon noise with $f/2$ aperture) mechanisms under 25 mV reverse bias. Therefore, it seems that exceptionally trap-free material is required to achieve desirable imaging performance in the VLWIR band. Longer cut-off sensors are usually utilized for low background (cold target) applications in order to receive substantial photon flux from the target. Noting that trap densities below 10^{14} cm^{-3} are

rarely reported for HgCdTe material, increasing the cut-off wavelength of the sensor with this objective does not seem to provide advantage unless the (exceptional) purity of the material is confirmed. As an example, the spectral photon exitance of a 77 K target at 14 μm is larger than that at 12 μm by a factor of ~ 5 . Considering the significant difference (by more than a factor of 3 under the simulation conditions) between the detectivities of the 12 and 14 μm cut-off sensors (mostly due to TAT induced I/f noise), an apparent increase in the sensitivity may not be expected when the cut-off wavelength is increased to maximize the photon irradiance from a cold target at least with the trap densities around the value utilized in these simulations (10^{14} cm^{-3}). It should also be noted that operating the longer cut-off sensor at lower temperatures may result in significant dark current reduction, however it may not provide considerable detectivity improvement due to the relative temperature insensitivity of the tunneling currents.

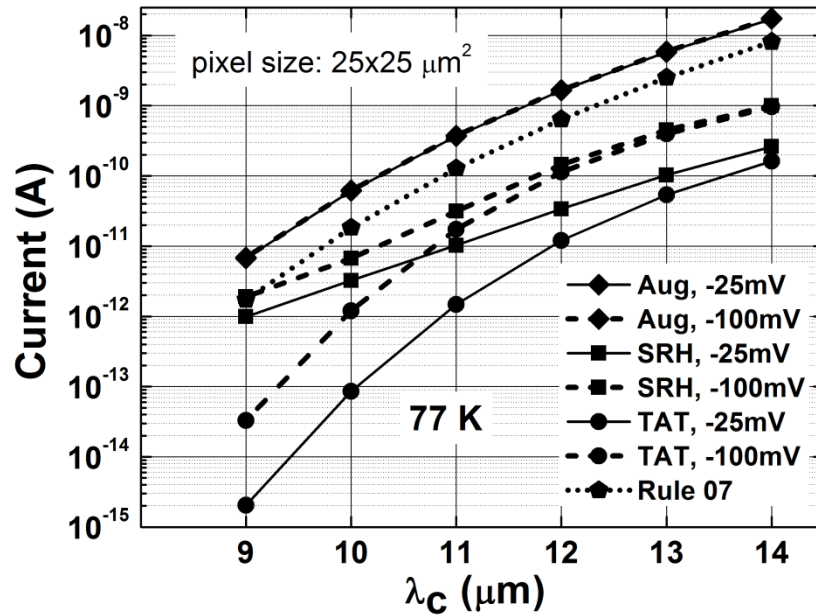


Figure 4.3 Contribution of various G-R mechanisms to the dark current under reverse bias voltages of 25 and 100 mV ($\lambda_c=10 \mu\text{m}$, $N_I=10^{14} \text{ cm}^{-3}$, $d_{abs}=8 \mu\text{m}$, $T=77 \text{ K}$)

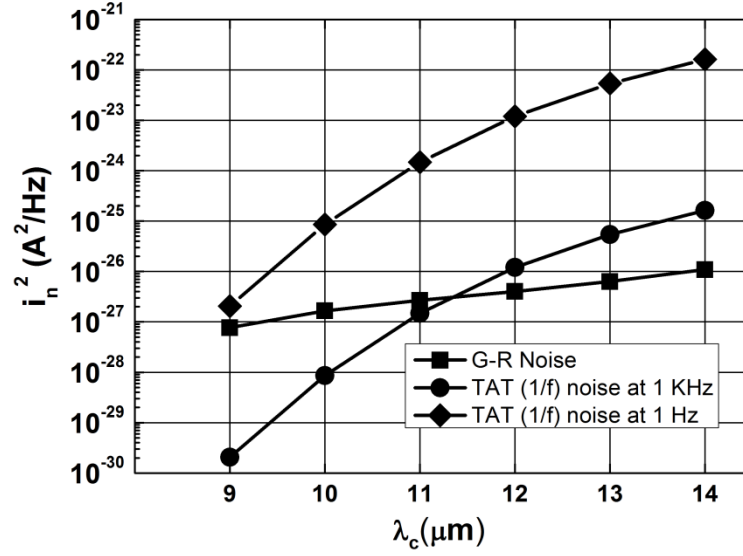


Figure 4.4 Squared magnitude of the noise current spectral density due to TAT and other g-r (including photon noise) mechanisms under 25 mV reverse bias ($N_i=10^{14} \text{ cm}^{-3}$, $E_i=0.5E_g$, $d_{abs}=8 \mu\text{m}$, $T=77 \text{ K}$, f/2 optics, 300 K background)

It should be noted that tunneling may not be the only component of the dark current introducing $1/f$ noise. However, experiments have indicated that tunneling introduced $1/f$ noise is considerably larger than that contributed by the other leakage mechanisms [81].

R_dA (dynamic resistance-area product) is shown in Fig. 4.5. At $\lambda_c=10 \mu\text{m}$ and $V_a=-25 \text{ mV}$, we obtain $R_dA=759.1 \Omega\cdot\text{cm}^2$ which is in the order of the experimental observations [73], [49]. If we approach to $V_a=-10 \text{ mV}$ at the same cut-off wavelength, we reach a reduced value of $R_dA=203.2 \Omega\cdot\text{cm}^2$ since diffusion and other intrinsic recombination processes (radiative, Auger) start to dominate. For LWIR p⁺-n HgCdTe diodes at 77 K, experimental R_dA at zero bias (R_0A) is around 100-200 $\Omega\cdot\text{cm}^2$ [73], [82], [49]. Our numerical R_dA is compatible with the experiment showing the accuracy and reliability of our modeling and simulation.

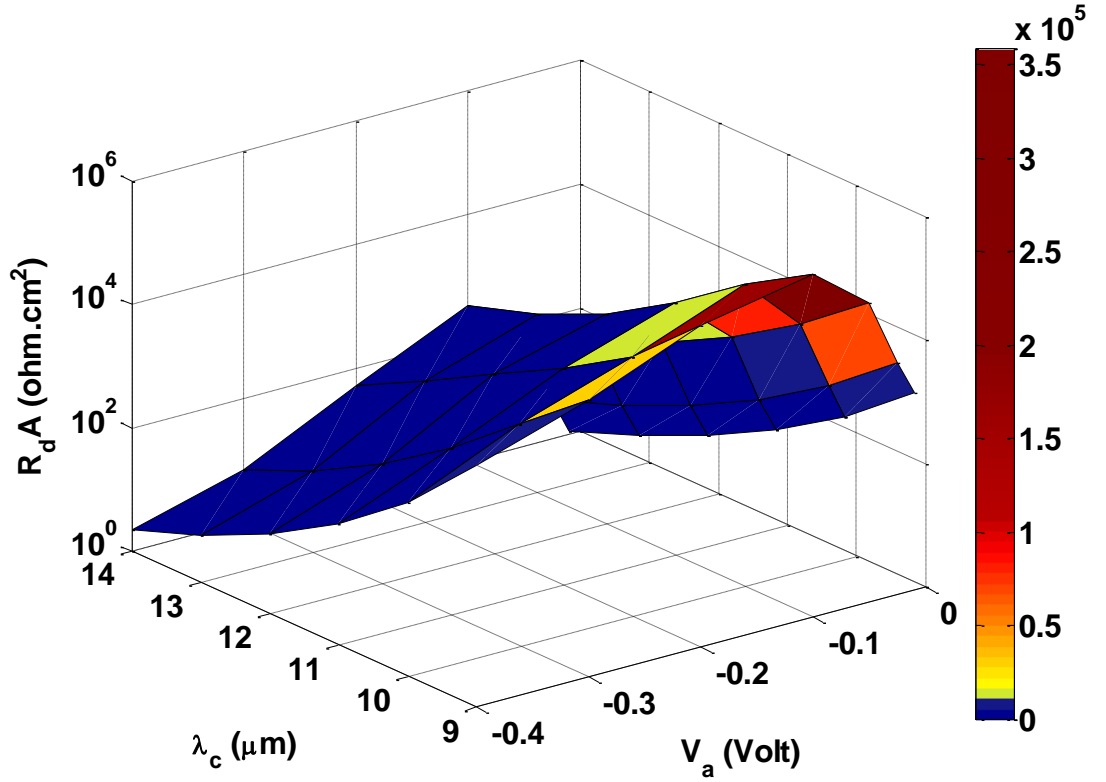


Figure 4.5 $R_d A$ with respect to cut-off wavelength (λ_c) and applied bias (V_a) voltage ($N_t=10^{14} \text{ cm}^{-3}$, $E_t=0.5E_g$, $d_{abs}=8 \text{ μm}$, $T=77 \text{ K}$)

Fig. 4.6 indicates that the current responsivity increases towards the VLWIR region. p-n HgCdTe photodiodes fabricated in VLWIR are anticipated to have 14-15 % higher current responsivity in comparison to the LWIR ones.

In our study, the specific detectivity (D^*) is computed by considering thermal (Johnson-Nyquist), generation-recombination including photon (g-r) and $1/f$ noises extracted from the simulations according to the noise current expressions presented in section 1.4.

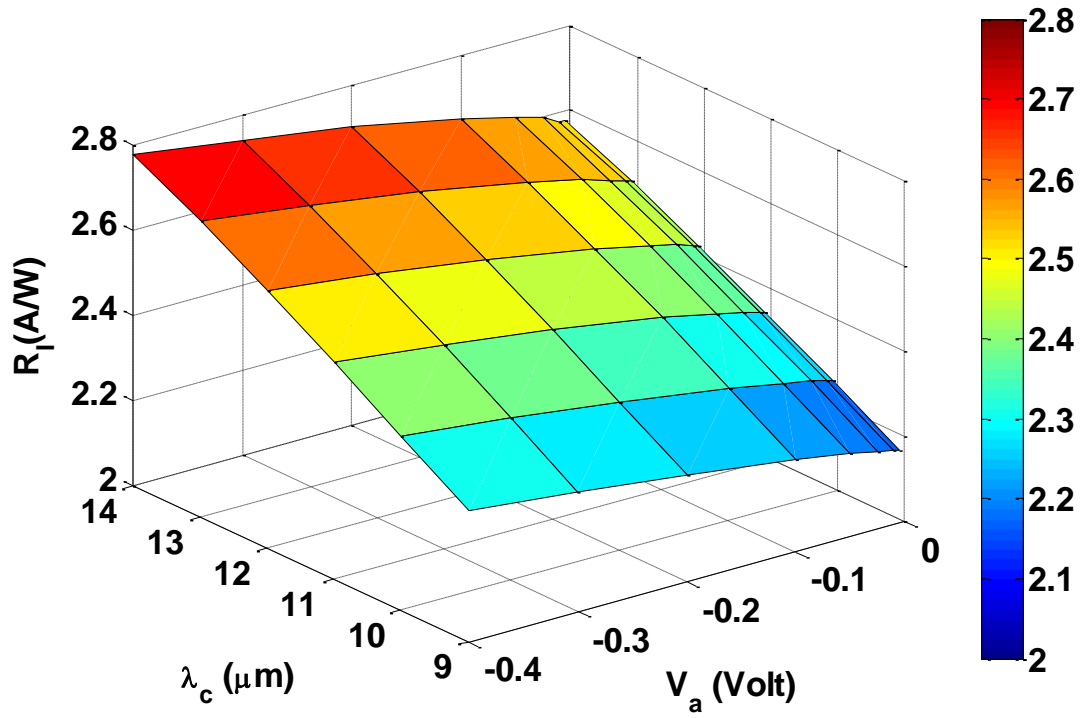


Figure 4.6 Current responsivity with respect to cut-off wavelength (λ_c) and applied bias (V_a) voltage ($N_i=10^{14} \text{ cm}^{-3}$, $E_i=0.5E_g$, $d_{abs}=8 \text{ } \mu\text{m}$, $T=77 \text{ K}$, $f/2$ optics, 300 K background)

As seen in Fig. 4.7, the maximum achievable specific detectivity under the simulation conditions is $1.91 \times 10^{11} \text{ cm.Hz}^{1/2}/\text{W}$ at $9 \text{ } \mu\text{m}$ cut-off and at the slight reverse bias of -10 mV . D^* is $1.12 \times 10^{11} \text{ cm.Hz}^{1/2}/\text{W}$ at the same bias and $10 \text{ } \mu\text{m}$ cut-off. As the cut-off wavelength and the magnitude of the reverse bias increase, D^* decreases due to the increase in the total noise current. With our simulation parameters and the wavelength/bias range, we have found that minimum D^* of $2.39 \times 10^8 \text{ cm.Hz}^{1/2}/\text{W}$ occurs at $14 \text{ } \mu\text{m}$ cut-off and -0.4 V bias. The simulations enlighten the facts that if the magnitude of the reverse bias voltage is switched from near-zero bias ($\approx 10 \text{ mV}$) to 0.4 V , the specific detectivity is significantly deteriorated (more than 90 %) in the LWIR and VLWIR p-n HgCdTe photodiodes. Similar performance loss is observed if we prefer to use VLWIR HgCdTe diode instead of the LWIR diode at a fixed reverse bias.

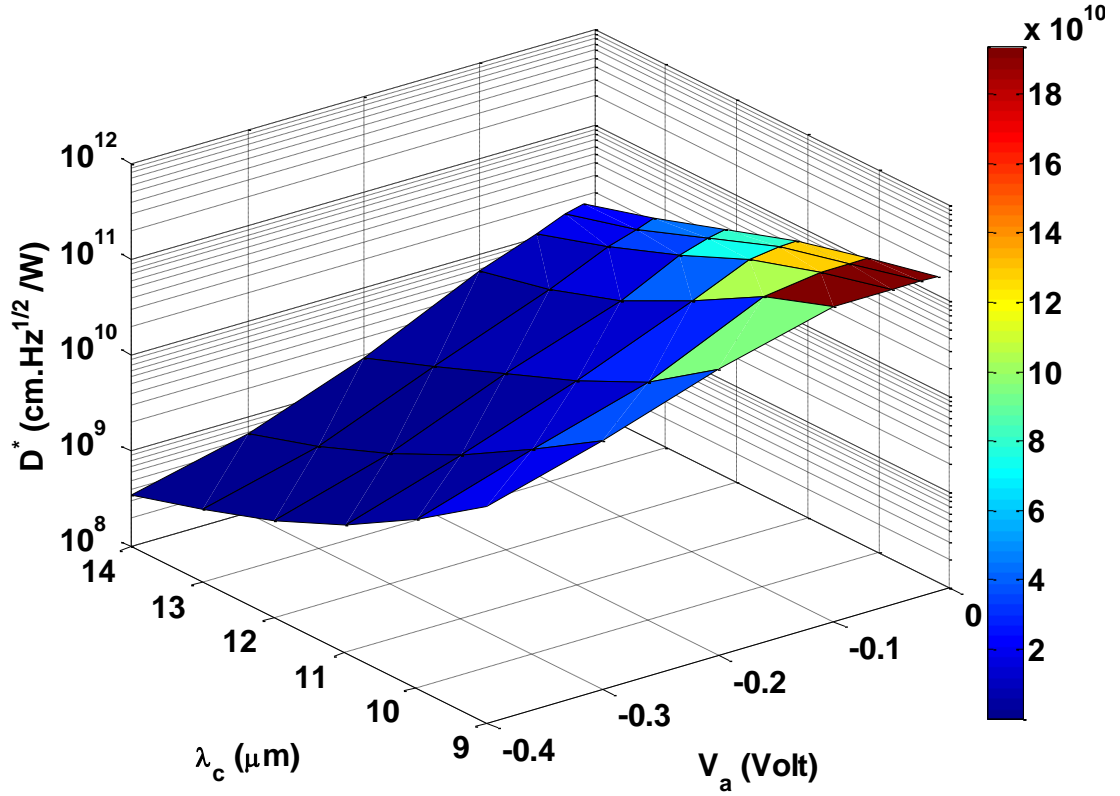


Figure 4.7 Specific detectivity (D^*) with respect to cut-off wavelength (λ_c) and applied bias (V_a) voltage ($N_t=10^{14} \text{ cm}^{-3}$, $E_t=0.5E_g$, $d_{abs}=8 \mu\text{m}$, $T=77 \text{ K}$, f/2 optics, 300)

4.3 Dependence on Trap Characteristics

In this part, effect of the trap density and the trap energy level is investigated with LWIR and VLWIR cut-off wavelengths. Cut-off wavelengths are fixed at 10 μm and 14 μm , respectively. Numerical simulations are performed at near-zero reverse bias (i.e. -10 mV and -5 mV). Dark, TAT and photocurrents are extracted at -10 mV. R_dA at -10 mV bias is computed using numerical dark currents of -10 mV and -5 mV. N_t is varied in the range of 10^{13} and 10^{15} cm^{-3} . E_t is varied in the range of $0.5E_g$ to $0.8E_g$ from the top of the valence band.

Figs. 4.8 and 4.9 show the specific detectivity of 10 and 14 μm cut-off sensors ($d_{abs}=8 \mu\text{m}$) biased near zero (10 mV reverse) bias. The degradation in the detectivity is much more significant with increasing trap density for the 14 μm cut-off detector. An important observation is that the trap level (E_t) resulting in maximum degradation depends on the cut-off wavelength. It is generally assumed that midgap ($0.5E_g$) traps

are the most effective g-r centers. While this is true for 14 μm cut-off sensor, the dominant trap level is $\sim 0.7E_g$ for the LWIR detector with the cut-off wavelength of 10 μm . The change in the responsivity of the detector is insignificant (less than 2 %) when the trap density is increased by two orders of magnitude. It should be noted that 10 μm cut-off HgCdTe sensors with $E_t=0.7E_g$ is observed to have 30-40 % smaller detectivity with respect to other trap levels when $N_t=1 \times 10^{15} \text{ cm}^{-3}$. Considering the fact that traps with $E_t \sim 0.7E_g$ have been reported in LWIR HgCdTe material [34], our results suggest that the trap density should be kept significantly below $1 \times 10^{15} \text{ cm}^{-3}$ in order to avoid degraded sensitivity in LWIR HgCdTe sensors even under small reverse bias voltages. Another important observation is the very strong reduction in the detectivity of the 14 μm sensor with the increasing trap density as E_t approaches $0.5E_g$. Even trap densities as low as 10^{14} cm^{-3} result in considerable degradation in the sensitivity. This seems to be the major limitation of VLWIR HgCdTe sensor technology along with the difficulty in achieving uniform growth over a substantially large area for staring focal plane arrays.

Fig. 4.10 shows the variation of the dominant sensitivity degrading trap level versus the sensor cut-off wavelength with $N_t=1 \times 10^{15} \text{ cm}^{-3}$. While the dominant trap level is $0.5E_g$ for 14 μm cut-off throughout the entire bias range, this level is shifted from $0.7E_g$ to $0.5E_g$ as the bias voltage is increased for the 10 μm cut-off sensor. This variation in the dominant trap level with the bias voltage can be explained as follows. Since the density of states of holes (N_v) is much more higher (around 1000 times) than the electrons (N_c), the tunneling rate of electrons (W_c) is higher than the tunneling rate of holes (W_v) given in Eqs. (3.30) and (3.31). Fig. 4.11 shows that as the reverse bias increases, the width of the region where electron/hole tunneling are possible (middle region) enlarges, so dominant degrading trap level shifts to the midgap. On the other hand, near-zero bias causes this region to vanish, as a result, degrading trap level occurs at $E_t=0.7E_g$.

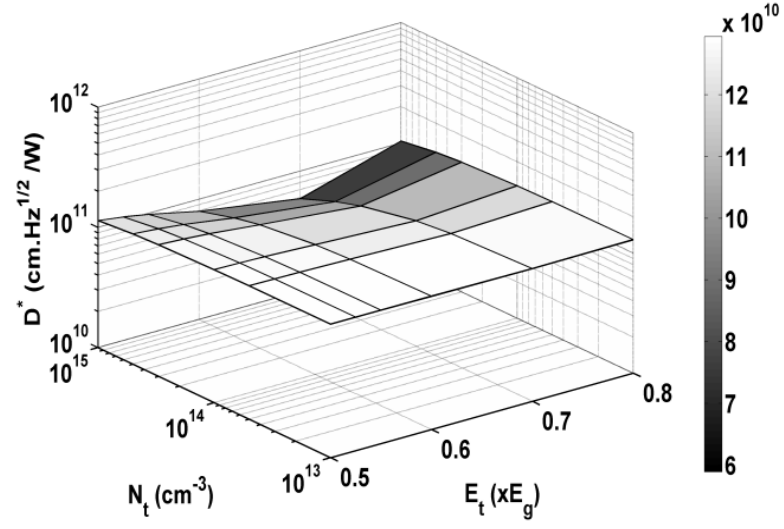


Figure 4.8 Specific detectivity of 10 μm cut-off sensor ($d_{abs}=8 \mu\text{m}$) biased near zero (10 mV reverse) bias

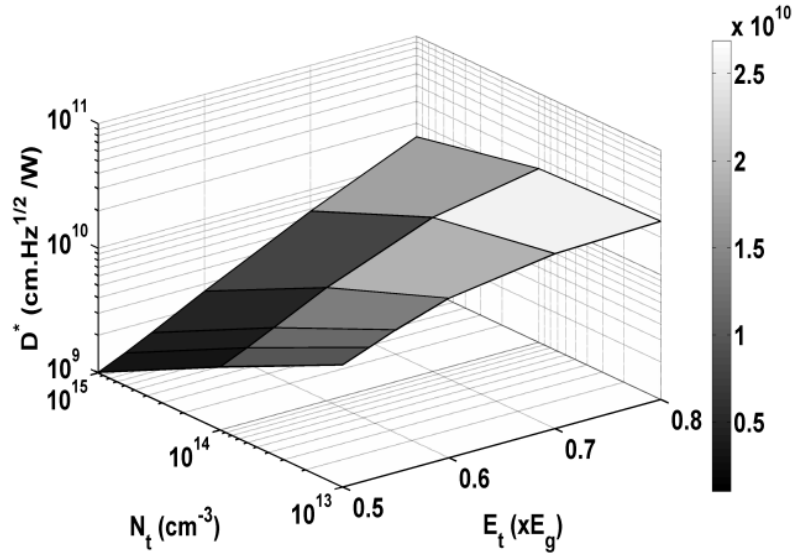


Figure 4.9 Specific detectivity of 14 μm cut-off sensor ($d_{abs}=8 \mu\text{m}$) biased near zero (10 mV reverse) bias

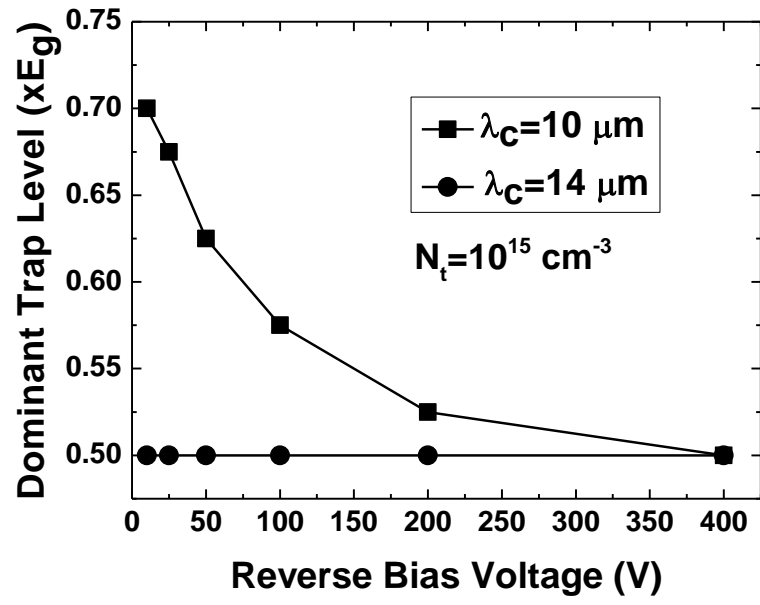


Figure 4.10 Variation of the dominant detectivity degrading trap level with the bias voltage on the detector ($T=77$ K)

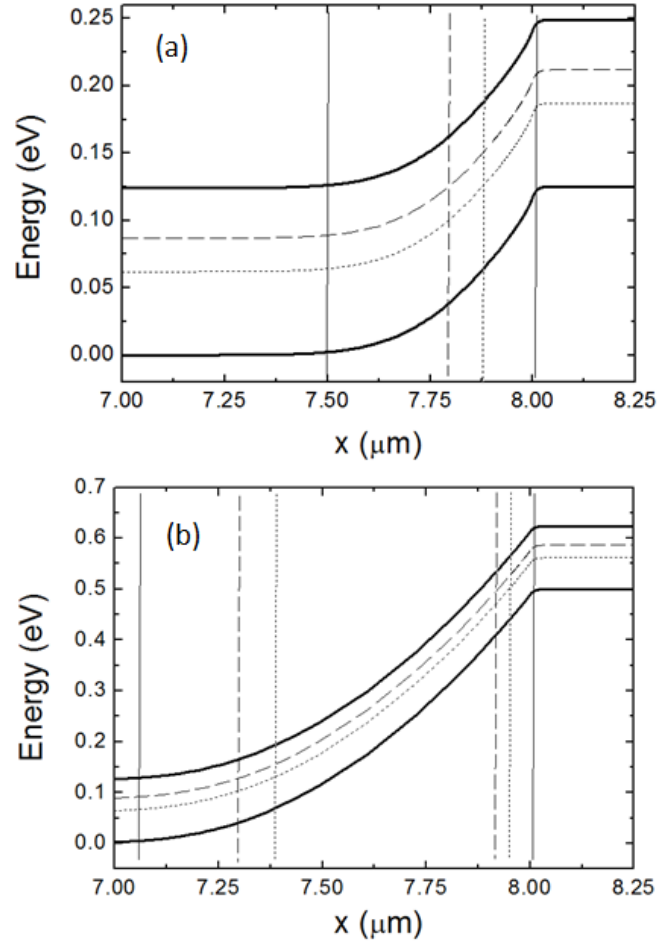


Figure 4.11 Energy band diagram of the 10 μm cut-off sensor under (a) small and (b) large reverse bias. The dashed and dotted lines show the traps at $E_t = 0.7E_g$ and $0.5E_g$, respectively

4.4 Effects of the Auger R-G Mechanism

Fig. 4.12 shows the variation of the responsivity of the sensor on the absorber layer thickness. The absorber layer thickness of the sensor is varied in the range of 2-20 μm while fixing the other parameters as $\lambda_c=10 \mu\text{m}$, $N_t=10^{14} \text{ cm}^{-3}$, $E_t=0.5E_g$, $V_a=-0.1 \text{ V}$ and $T=77 \text{ K}$. The responsivity is maximized at an absorber layer thickness of 10 μm in agreement with the typically utilized absorber layer thickness in LWIR HgCdTe detectors. In our study, the hole diffusion length (L_p) is 50 μm , which is much greater than the d_{abs} satisfying the requirement for a narrow diode. The absorber layer should be thick enough to absorb all the incoming radiation while being shorter than the hole diffusion length in order to minimize the volume where the dark current is generated. In other words, Eq. (4.2) must be fulfilled for optimal performance [52]. The absorption coefficient (α) at the material composition of interest is 1230 cm^{-1} yielding a penetration depth ($1/\alpha$) of 8.13 μm .

$$\frac{1}{\alpha} \langle d_{abs} \rangle L_p. \quad (4.2)$$

We observe this characteristic apparently in the numerical simulation results presented in Fig. 4.12. When $d_{abs} < 8 \mu\text{m}$, responsivity monotonously increases with the increase of d_{abs} due to the increase in the photon absorption (in a single pass detector). It should be noted that the dark current decreases in this range due to the narrow diode behavior in the case of high recombination velocity at the contacts. The optimum d_{abs} yielding the maximum photocurrent to dark current ratio is $\sim 10 \mu\text{m}$ under the simulation conditions. Absorber layer thicknesses below 6 μm result in considerably degraded performance. However, it should be noted that the performance can further be improved using double-pass structures with recombination barriers and smaller d_{abs} [83].

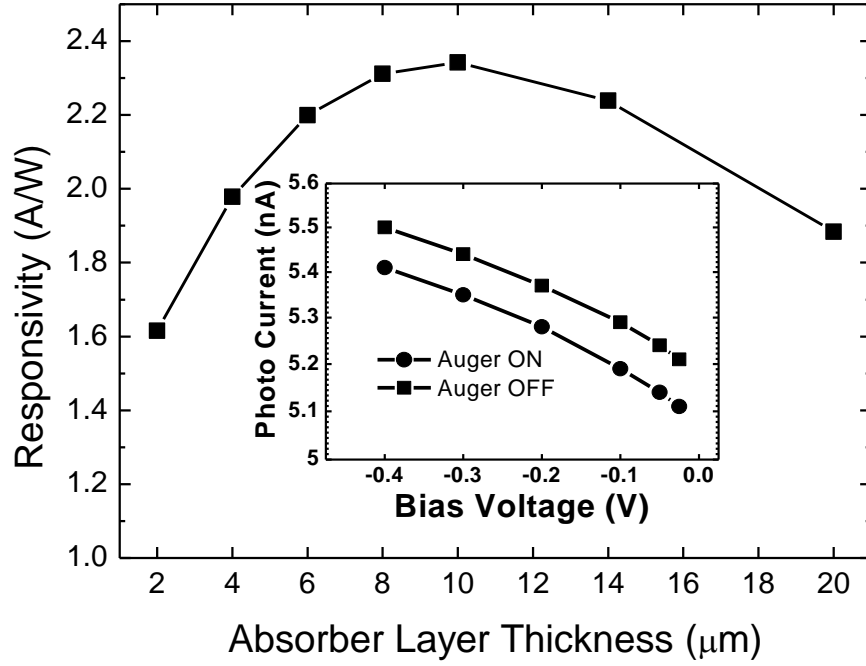


Figure 4.12 Responsivity versus absorber layer thickness (10 μm cutoff, $N_t=10^{14} \text{ cm}^{-3}$, $E_t=0.5E_g$, $V_a=-0.1 \text{ V}$, $T=77 \text{ K}$). The inset shows the variation of the photocurrent when the Auger mechanism is turned on and off in the simulation ($|F_1F_2|=0.2$, $d_{abs}=8 \mu\text{m}$)

The inset of Fig. 4.12 shows the variation of the photocurrent when the Auger mechanism is turned on and off in the simulation. There have been efforts such as using a wide-gap cap layer to suppress the Auger mechanism in HgCdTe detectors in order to decrease the dark current of the sensor. In order to assess the level of improvement that can be achieved by Auger suppression, we have made simulations at two different cut-off wavelengths of 10 and 12 μm by turning the Auger mechanism on and off. The Auger rate is directly proportional to the value of the overlap integral ($|F_1F_2|$) which is expected to be in the range of 0.1-0.3 [50]. Due to the lack of information on the exact value of the overlap integral, we carried out simulations with different $|F_1F_2|$ values (0.2 and 0.3) in order to identify the range of improvement in the sensor performance when the Auger mechanism is suppressed. As seen in the inset of Fig. 4.16, the existence of Auger process (with $|F_1F_2|=0.2$) slightly reduces the photocurrent of the 10 μm cut-off sensor. At -25

mV bias, photocurrent decreases by 2 % and 4.3 % when $|F_1 F_2| = 0.2$ and 0.3, respectively. For the 12 μm cut-off sensor, the photocurrent decreases by 2.6 % and 5.6 % with $|F_1 F_2| = 0.2$ and 0.3 under same bias voltage. In other words, the Auger mechanism has a twofold effect on the sensitivity of the sensor by decreasing the photocurrent and increasing the dark current.

Physical reason for this behavior can be explained with the help of further numerical simulations. Profiles of R-Gs under IR illumination and dark conditions are exhibited in Figs. 4.13 and 4.14, respectively. If we compare these figures, we observe that Auger mechanism behaves in recombination mode along the active n layer then it changes to the generation mode in p side under IR photon illumination case.

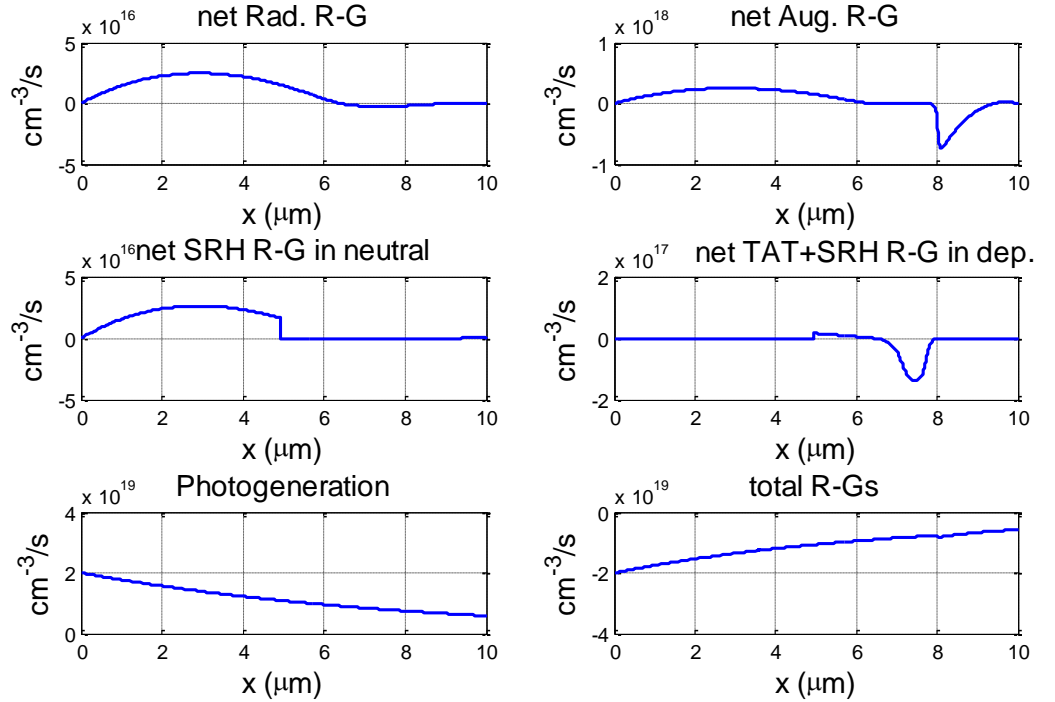


Figure 4.13 R-Gs under IR photon illumination ($V_a = -25$ mV)

On the other hand, under dark case in Fig. 4.14, Auger behaves always as generation mechanism. This behavior is better understood by the help of numerically extracted profiles of $np-n_i^2$ under IR light and dark conditions in Figs. 4.15 and 4.16, respectively. Since Auger R-G mechanism is modeled by Eq. (3.24), some parts of photogenerated electrons and holes are removed due to Auger recombination process

and we obtain a loss in the photocurrent when the Auger mechanism exists. On the other hand, under dark condition, Auger process always behaves as generation mode which increases dark current. This characteristic of the Auger mechanism over the device could not be explained in analytical methods emphasizing the advantage of numerical simulation.

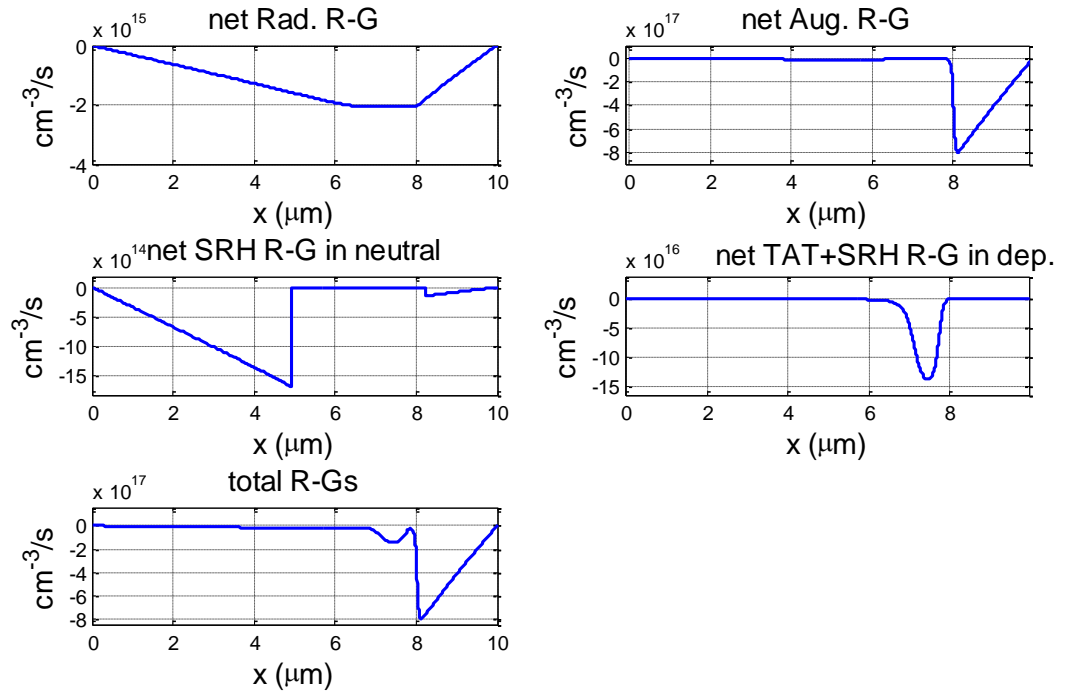


Figure 4.14 R-Gs under dark condition ($V_a = -25$ mV)

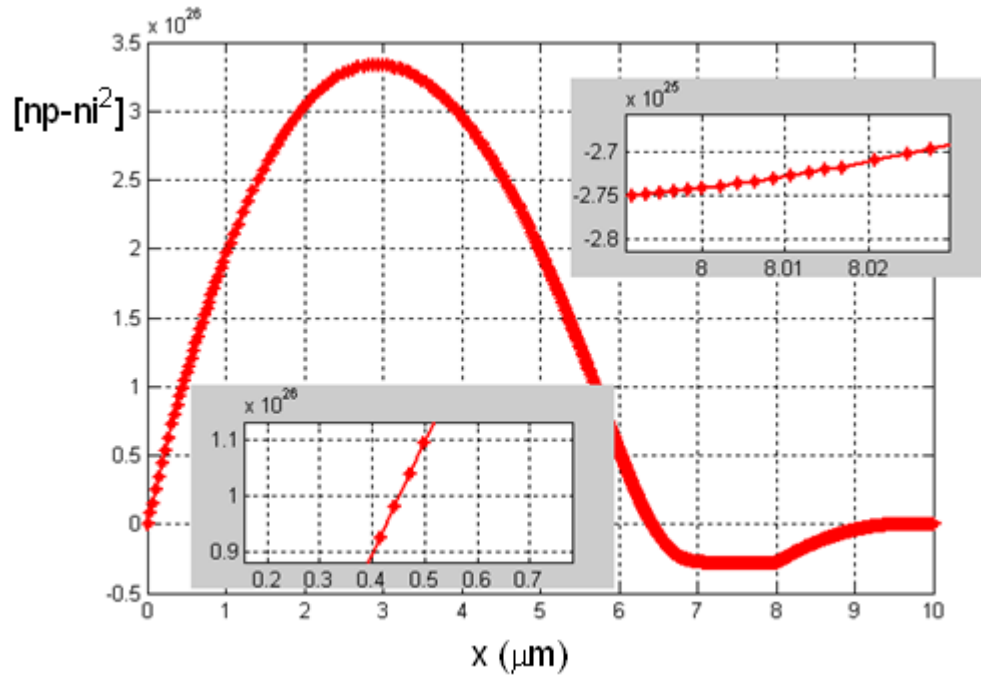


Figure 4.15 Profile of $np-n_i^2$ under IR photon illumination ($V_a=-25$ mV)

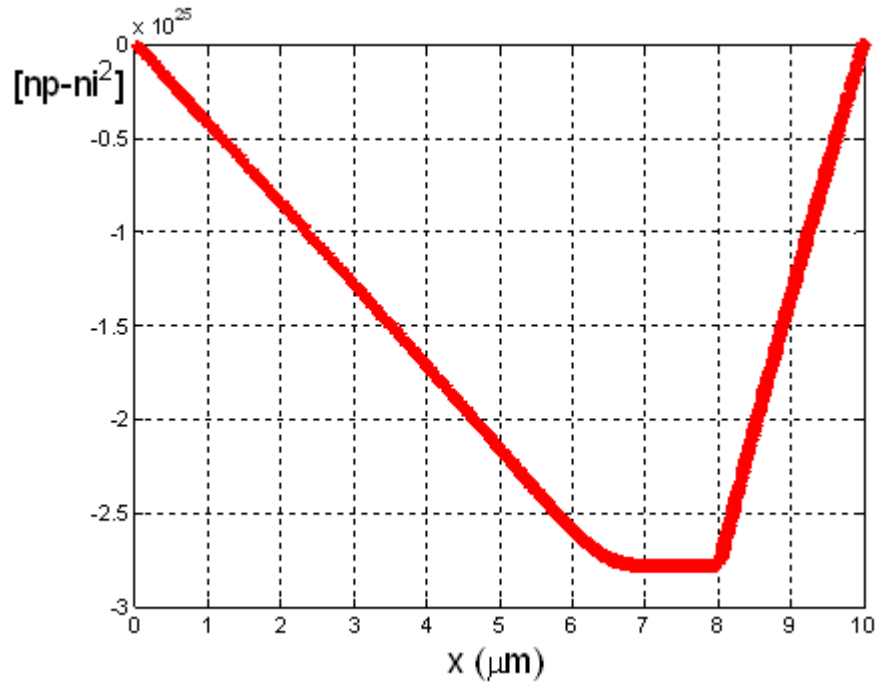


Figure 4.16 Profile of $np-n_i^2$ under dark condition ($V_a=-25$ mV)

As a conclusion, numerical investigation of the Auger rate profiles through the device structure under illumination reveals that while the Auger mechanism behaves

in recombination mode along the n-type absorber layer, it acts as a generation mechanism in the p side. On the other hand, Auger behaves as a generation mechanism throughout the device under dark conditions. The reduction in the photocurrent due the presence of the Auger process results from the partial loss in the density of the photogenerated carriers due to Auger recombination.

4.5 Numerical Fit to the Experimental Data

In order to compare the results of our numerical simulations with experimental data, we used the I-V data measured on a p⁺-n HgCdTe ($x=0.222$) photodetector. The solver has been run several times by changing N_t , E_t and and the capture cross sections until matching of the simulation to the experimental data has been achived. Experimental and numerical fit results under dark and illuminated conditions are given in Figs. 4.17.

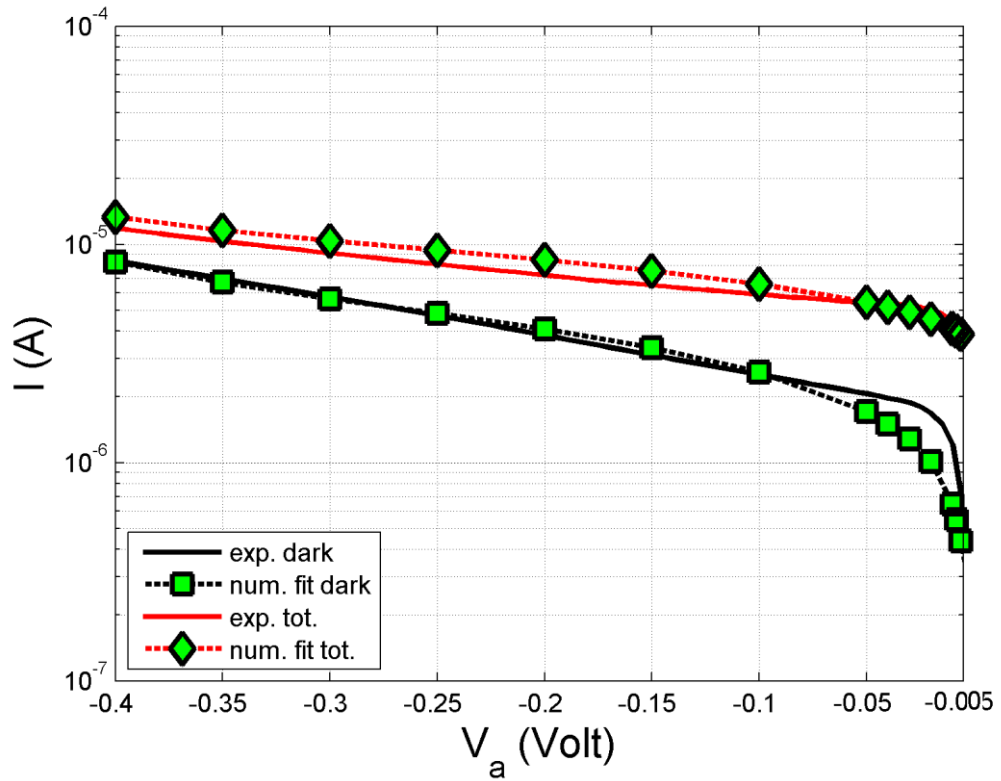


Figure 4.17 Experimental and numerical fit currents under dark and illuminated conditions

Fitted results are $N_i=5 \times 10^{15} \text{ cm}^{-3}$, $E_i=0.65E_g$, $\sigma_n=2.1 \times 10^{-13} \text{ cm}^2$, and $\sigma_p=3.1 \times 10^{-13} \text{ cm}^2$. Resulting electron and hole lifetimes are 15.1 ps and 80.9 ps.

In conclusion, numerical simulations have been completed with all possibly dominant g-r mechanisms (Auger, radiative, SRH and TAT) and detector noise sources (Johnson, g-r and $1/f$). The simulations uncover significant observations enlightening some critical issues that should be taken into consideration by the detector designer.

CHAPTER 5

CONCLUSION AND FURTHER WORK

This thesis presents a detailed investigation of LWIR p on n HgCdTe detectors through numerical simulations at 77 K incorporating all considerable R-G mechanisms including trap assisted tunneling (TAT), Shockley-Read-Hall (SRH), Auger and radiative processes. The ohmic contacts have been considered to be abrupt with infinitely large surface recombination velocity. Considering the fact that the TAT mechanism is one of the most dominant sensitivity limiting mechanisms, this process was incorporated into the numerical simulator in detail. While the provided information can be used as a guide for optimizing the device processing conditions and detector structure, it also enlightens the importance of various intrinsic mechanisms on the detector sensitivity.

As to our knowledge, this work is one of the most comprehensive simulation-based investigations of the HgCdTe detector performance providing important results that can be used as a guide for optimization of the detector performance in order to meet the demanding requirements of the third generation thermal imagers.

The most important conclusions that can be extracted from this work can be summarized as follows.

- 1) The results show that the dominant sensitivity degrading trap level depends on the detector cut-off wavelength being $0.7E_g$ for a 10 μm cut-off sensor instead of $0.5E_g$ which is generally believed to be the most efficient R-G level. On the other hand, the detectivity of a 14 μm sensor degrades very rapidly with the increasing trap density as E_t approaches $0.5E_g$. Even trap densities as low as 10^{14} cm^{-3} result in considerable degradation in the sensitivity.

- 2) The TAT related $1/f$ noise dominates the sensor noise throughout the entire reverse biasing voltage range at a trap density as low as $1 \times 10^{14} \text{ cm}^{-3}$ for sensors with cut-off wavelengths above $11 \text{ }\mu\text{m}$. Considering the fact that trap densities below this level is rarely reported for HgCdTe material, exceptionally pure material is required to achieve desirable performance for these sensors. This seems to be one of the major limitations of VLWIR HgCdTe sensor technology.
- 3) Simulation results show that Auger suppression has a twofold effect on the sensitivity of the sensor by increasing the dark current and decreasing the photocurrent.

Further work on the above issues can be listed as follows.

- 1) In this thesis, mathematical modeling of the contacts has been based on infinitely large surface recombination velocity. In reality, surface recombination velocity is finite and its value depends on the surface characteristics of the contacts. Therefore, performance and capability of the numerical simulations can be further improved with embedding finite surface velocity as a variable material parameter to the solver at the boundary of the contacts.
- 2) It should be kept in mind that infinitely large surface recombination velocity can still be used if we change our simulation geometry to $p^+-n^-n^+$ configuration instead of p^+-n one. In the $p^+-n^-n^+$ device, abrupt removal of the minority carriers at the contact-edge of the active layer is prevented. Therefore, numerical simulations will have capability to overcome the limitations due to the infinite contact recombination velocity without changing the contact modeling.
- 3) Finally, mathematical modeling of the simulator can be extended to cover the effects of heterojunction cap layer and multi-spectral capabilities. With increased simulation capability of the solver, the material and device requirements for the next generation HgCdTe IR sensors may be more realistically simulated and optimized.

REFERENCES

- [1] A. Rogalski, "Infrared Detectors: an overview," *Infrared Physics & Technology*, vol. 43, pp. 187-210, 2002.
- [2] H. Koçer, *Kızılötesi Dedektör Teknolojileri.*: K.K.Loş.K.lğı EOSBM.Md.lüğü, 2006.
- [3] C. Beşikci, "EE755 Infrared Devices and Systems," METU, Lecture Notes 2008.
- [4] S. Özer, "InSb And InAsSb Infrared Photodiodes on Alternative Substrates and InP/InGaAs Quantum Well Infrared Photodetectors: Pixel and Focal Plane Array Performance," METU, Ph.D. Thesis 2005.
- [5] B. Aşıcı, "Long Wavelength Infrared Mercury Cadmium Telluride Photodiodes and Focal Plane Arrays," METU, MS Thesis 2005.
- [6] A. Rogalski and K. Chrzanowski, "Infrared devices and techniques," *Opto-Electronics Review*, vol. 10, pp. 111-136, 2002.
- [7] S. U. Eker, "Single and Dual Band Quantum Well Infrared Photodetector Focal Plane Arrays on InP Substrates," METU, PhD. Thesis 2010.
- [8] M. Marquis, *Handouts on Thermal Imaging Systems Theory.*: Texas Instruments Incorporated Defense Systems, 1996.
- [9] I. Moir and A. Seabridge, *Military Avionics Systems.*: John Wiley & Sons, 2006.
- [10] H. M. Runciman, *Thermal Imaging.*: CRC Press LLC, 2000.
- [11] A. Rogalski, *Infrared Photon Detectors.*: SPIE, 1995.

- [12] T. P. Sun, S. C. Lee, and S. J. Yang, "The current leakage mechanisms in InSb p+n diodes," *Journal of Applied Physics*, vol. 67, pp. 7092-7097, 1990.
- [13] Ö. Ersagun, "Dark Current Mechanisms and Passivation of InAsSb Infrared Photodiodes on Alternative Substrates," METU, MS Thesis 2005.
- [14] L. Esaki and R. Tsu, "Superlattice and negative differential conductivity in semiconductors," *IBM Journal of Research and Development*, vol. 14, pp. 62-65, 1970.
- [15] S. D. Gunapala et al., "1024 × 1024 pixel mid-wavelength and long-wavelength infrared QWIP focal plane arrays for imaging applications," *Semiconductor Science and Technology*, vol. 20, pp. 473-480, 2005.
- [16] A. Rogalski, "Insight on quantum dot infrared photodetectors," *Journal of Physics: Conference Series*, vol. 146, pp. 012030-012038, 2009.
- [17] H.C. Liu, "Quantum dot infrared photodetector," *Opto-Electronics Review*, vol. 11, pp. 1-5, 2003.
- [18] R. Rehm et al., "InAs/GaSb superlattice focal plane arrays for high-resolution thermal imaging," *Opto-Electronics Review*, vol. 14, pp. 19-24, 2006.
- [19] P. Capper and J. W. Garland, *Mercury Cadmium Telluride Growth, Properties and Applications.*: Wiley, 2011.
- [20] Y. Nemirovsky and A. Unikovsky, "Tunneling and 1/f noise in HgCdTe photodiodes," *Journal of Vacuum Science & Technology*, vol. 10, pp. 1602-1610, 1992.
- [21] Alper Aksoy, "Termal İz Azaltıcı Teknolojiler/Yöntemler Eğitimi," ASELSAN, SATEM kurs sunusu 2010.
- [22] M.A. Fauci et al., "Medical infrared imaging-differentiating facts from fiction, and the impact of high precision quantum well infrared photodetector camera

systems, and other factors, in its reemergence," *Infrared Physics & Technology*, vol. 42, pp. 337-344, 2001.

[23] S. E. Lyshevski, *Handbook of Nanoscience Engineering and Technology*.: CRC Press LLC, 2003.

[24] A. Goldberg and K. K. Choi, "Recent progress in the application of large format multispectral QWIP IRFPAs," *Proceedings of SPIE*, vol. 5406, pp. 624-638, 2004.

[25] R. S. Allgaier, "History of narrow-gap semiconductors and semimetals, 1945 - 1965," *Semiconductor Science and Technology*, vol. 5, pp. S326-S333, 1990.

[26] A. Rogalski, "Infrared detectors: status and trends," *Progress in Quantum Electronics*, vol. 27, pp. 59-210, 2003.

[27] J. Piotrowski and F. Perry, "Designers still choose mercury cadmium telluride," *Laser Focus World*, vol. 3, pp. 20-30, 1997.

[28] A. Rogalski, K. Adamiec, and J. Rutkowski, *Narrow-Gap Semiconductor Photodiodes*.: SPIE Press, 2000.

[29] P. Norton, "HgCdTe detectors," *Opto-Electronics Review*, vol. 10, pp. 159-174, 2002.

[30] P. Capper, *Narrow-gap II-VI Compounds for Optoelectronic and Electromagnetic Applications*.: Chapman & Hall, 1997.

[31] P. Capper, *Properties of Narrow Gap Cadmium-Based Compounds*.: INSPEC, 1994.

[32] A. Cho, "Film deposition by molecular beam techniques," *Journal of Vacuum Science and Technology*, vol. 8, pp. S31-S38, 1971.

[33] MBE Growth. [Online].

http://projects.ece.utexas.edu/ece/mrc/groups/street_mbe/mbechapter.html

- [34] S. Kasap, *Handbook of Electronic and Photonic Materials.*: Springer, 2006.
- [35] W. D. Hu et al., "Simulation and design considerations of photoresponse for HgCdTe infrared photodiodes," *Optical and Quantum Electronics*, vol. 40, pp. 1255-1260, 2008.
- [36] G. M. Williams and R. E. De Wames, "Numerical simulation of HgCdTe detector characteristics," *Journal of Electronic Materials*, vol. 24, pp. 1239-1248, 1995.
- [37] W. Hu et al., "Accurate simulation of temperature-dependent dark current in HgCdTe infrared detectors assisted by analytical modeling," *Journal of Electronic Materials*, vol. 39, pp. 981-985, 2010.
- [38] P. K. Saxena, "Modeling and simulation of HgCdTe based p+-n-n+ LWIR photodetector," *Infrared Physics & Technology*, vol. 54, pp. 25-33, 2011.
- [39] P. K. Saxena and P. Chakrabarti, "Computer modeling of MWIR single heterojunction photodetector based on mercury cadmium telluride," *Infrared Physics & Technology*, vol. 52, pp. 196-203, 2009.
- [40] P. Y. Emelie et al., "Modeling of LWIR HgCdTe Auger-suppressed infrared photodiodes under nonequilibrium operation," *Journal of Electronic Materials*, vol. 37, no. 9, pp. 1362-1368, 2008.
- [41] C. J. Summers and B. Darling, "Computer modeling of carrier transport in (Hg,Cd)Te photodiodes," *Journal of Applied Physics*, vol. 59, pp. 2457-2466, 1986.
- [42] A. Rogalski, A. Jozwikowska, K. Jozwikowski, and J. Rutkowski, "Performance of p+-n HgCdTe photodiodes," *Semiconductor Science and Technology*, vol. 8, pp. 289-292, 1993.

- [43] M. Karimi, M. Kalafi, and A. Asgari, "Numerical optimization of an extracted HgCdTe IR-photodiodes for 10.6-um spectral region operating at room temperature," *Microelectronics Journal*, vol. 38, pp. 216-221, 2007.
- [44] J. Wenus, J. Rutkowski, and A. Rogalski, "Two-dimensional analysis of double-layer heterojunction HgCdTe photodiodes," *IEEE Transactions on Electron Devices*, vol. 48, pp. 250-260, 2001.
- [45] K. Jozwikowski, "Computer simulation of non-cooled long wavelength multi-junction (Cd,Te)Te photodiodes," *Infrared Physics & Technology*, vol. 41, pp. 353-359, 2000.
- [46] S.D. Yoo et al., "Numerical simulations for HgCdTe realated detectors," *Opto-Electronics Review*, vol. 7, pp. 347-356, 1999.
- [47] J. V. Gumenjuk-Sichevskaja, F. F. Sizov, V. N. Ovsyuk, V. V. Vasil'ev, and D. G. Esaev, "Charge transport in HgCdTe-based n+-p photodiodes," *Semiconductors*, vol. 35, pp. 800-806, 2001.
- [48] J. V. Gumenjuk-Sichevskaya and F. F. Sizov, "Currents in narrow-gap photodiodes," *Semiconductor Science Technology*, vol. 14, pp. 1124-1131, 1999.
- [49] K. Jozwikowski, M. Kopytko, A. Rogalski, and A. Jozwikowska, "Enhanced numerical analysis of current-voltage characteristics of long wavelength n-on-p HgCdTe photodiodes," *Journal of Applied Physics*, vol. 108, pp. 074519-1-074519-11, 2010.
- [50] E. Bellotti and D. D'orsogna, "Numerical analysis of HgCdTe simultaneous two-color photovoltaic infrared detectors," *IEEE Journal of Quantum Electronics*, vol. 42, pp. 418-426, 2006.
- [51] P. K. Saxena and P. Chakrabarti, "ATLAS simulation of LWIR photodetector based on mercury cadmium telluride," in *Proceeding of IEEE IWPSD*, 2007, pp.

778-781.

- [52] T. Niedziela and R. Ciupa, "Optimization of parameters of (Hg,Cd)Te n+-p photodiodes for 10.6-um spectral region operating at near-room temperatures," *Electron Technology*, vol. 33, pp. 542-547, 2000.
- [53] G. V. Chekanova, A.A. Drugova, V. Kholodnov, and M.S. Nikitin, "Simulation of MWIR and LWIR photodiodes based on n+-p and p-n junctions formed in HgCdTe heterostructures," *Proceeding of SPIE*, vol. 6737, pp. 673714-673718, 2007.
- [54] K. Kosai, "Status and application of HgCdTe device modeling," *Journal of Electronic Materials*, vol. 24, pp. 635-640, 1995.
- [55] W. D. Hu et al., "Numerical analysis of two-color HgCdTe infrared photovoltaic heterostructure detector," *Optical and Quantum Electronics*, vol. 41, pp. 699-704, 2010.
- [56] V. Gopal and V. Dhar, "Resistance-area product of diodes in a long-wavelength infrared HgCdTe mosaic array," *Infrared Physics & Technology*, vol. 43, pp. 51-59, 2002.
- [57] C. A. Keasler, M. Moresco, D. D'orsogna, P. Lamarre, and E. Bellotti, "3D numerical analysis of As-diffused HgCdTe planar pixel arrays," *Proceeding of SPIE*, vol. 7780, pp. 77800J-1-77800J-6, 2010.
- [58] V. Dhar, R. K. Bhan, R. Ashokan, and V. Kumar, "Quasi-2D analysis of the effect of passivant on the performance of long-wavelength infrared HgCdTe photodiodes," *Semiconductor Science and Technology*, vol. 11, pp. 1302-1309, 1996.
- [59] V. Ariel and G. Bahir, "Modeling of heterojunction HgCdTe photodiodes using approximate k.p approach," *Journal of Electronic Materials*, vol. 26, pp. 673-677, 1997.

- [60] A. Jozwikowska, K. Jozwikowski, J. Antonsewski, and Z. Orman, "Generation-recombination effects on the dark currents in CdTe-passivated midwave infrared HgCdTe photodiodes," *Journal of Applied Physics*, vol. 98, pp. 014504-1-014504-11, 2005.
- [61] A. Jozwikowska, K. Jozwikowski, J. Rutkowski, Z. Orman, and A. Rogalski, "Generation-recombination effects in high temperature HgCdTe heterostructure photodiodes," *Opto-Electronics Review*, vol. 12, pp. 417-428, 2004.
- [62] D. Vasileska. (2009) nanoHUB.org.
- [63] K. M. Kramer, W. Nicholas, and G. Hitchon, *Semiconductor Devices A Simulation Approach.*: Prentice Hall PTR, 1997.
- [64] R. E. Star, S. L. Price, K. J. Riley, and J. P. Rosbeck, "Background and temperature dependent current-voltage characteristics of Hg_{1-x}Cd_xTe photodiodes," *Journal of Applied Physics*, vol. 53, pp. 6430-6444, 1982.
- [65] D. H. Mao, "Optical and Electrical Characterization of Mercury Cadmium Telluride and Performance Simulation of Infrared Photodetectors," Stanford University, PhD Thesis 1998.
- [66] P. Y. Emelie, "HgCdTe Auger-Suppressed Infrared Detectors Under Non-Equilibrium Operation," The University of Michigan, PhD Thesis 2009.
- [67] D. D'orsogna, "Numerical Simulation Models and Stress Measurements for HgCdTe Infrared Detectors," Boston University, PhD Thesis 2010.
- [68] R. Kiran, "Optimization of the Hg_{1-x}Cd_xTe Surface and Its Characterization by Electrical and Optical Techniques," University of Illinois, PhD Thesis 2008.
- [69] W. Shockley and W.T. Read, "Statistics of the recombinations of holes and electrons," *Phys. Rev.*, vol. 87, pp. 835-842, 1952.

- [70] Y. Nemirovsky, R. Fastow, M. Meyassed, and A. Unikovsky, "Trapping effects in HgCdTe," *Journal of Vacuum Science & Technology*, vol. B9, pp. 1829-1839, 1991.
- [71] D. Rosenfeld and G. Bahir, "A model for the trap-assisted tunneling mechanism in diffused n-p and implanted n+-p HgCdTe photodiodes," *IEEE Transactions on Electron Devices*, vol. 39, pp. 1638-1645, 1992.
- [72] D. L. Polla and C. E. Jones, "Deep level studies of HgCdTe. I: narrow band-gap space-charge spectroscopy," *Journal of Applied Physics*, vol. 52, pp. 5118-5131, 1981.
- [73] J. Yoshino, J. Morimoto, and H. Wada, "Study of deep levels in mesa-type HgCdTe device," *Japanese Journal of Applied Physics*, vol. 37, pp. 4027-4031, 1998.
- [74] Z.F. Ivasiv, F.F. Sizov, and V.V. Tetyorkin, "Noise spectra and dark current investigations in n+-p-type Hg_{1-x}Cd_xTe photodiodes," *Semiconductor Physics, Quantum Electronics & Optoelectronics*, vol. 2, pp. 21-25, 1999.
- [75] V. Gopal, S. K. Singh, and R. M. Mehra, "Analysis of dark current contributions in mercury cadmium telluride junction diodes," *Infrared Physics & Technology*, vol. 43, pp. 317-326, 2002.
- [76] L.F. Shampine, J. Kierzenka, and M. W. Reichlet, "Solving Boundary Value Problems for Ordinary Differential Equations in MATLAB with bvp4c," Math. Dept., SMU, Tutorial 2000.
- [77] C. A. Hougen, "Model for infrared absorption and transmission of liquid-phase epitaxy HgCdTe," *Journal of Applied Physics*, vol. 66, pp. 3763-3767, 1989.
- [78] S. Ozer and C. Besikci, "Assessment of InSb photodetectors on Si substrates," *Journal of Physics D: Applied Physics*, vol. 36, pp. 559-563, 2003.

- [79] C. Besikci et al., "Characteristics of InAs_{0.8}Sb_{0.2} photodetectors on GaAs substrates," *Semiconductor Science and Technology*, vol. 16, pp. 992-996, 2001.
- [80] W. E. Tennant, "W. E. Rule 07" revisited: still a good heuristic predictor of p/n HgCdTe photodiode performance?," *Journal of Electronic Materials*, vol. 39, pp. 1030-1035, 2010.
- [81] A. I. D'souza, M.G. Stapelbroek, P. S. Wijewarnasuriya, R. E. Dewames, and G. M. Williams, "1/f noise in very-long-wavelength infrared Hg_{1-x}Cd_xTe detectors," *Journal of Electronic Materials*, vol. 31, pp. 699-703, 2002.
- [82] M. Razeghi, *Handbook of Infrared Detection Technologies.*: SPIE, 2002.
- [83] J. Piotrowski, P. Brzozowski, and K. Jozwikowski, "Stacked multijunction photodetectors of long-wavelength radiation," *Journal of Electronic Materials*, vol. 32, pp. 672-676, 2003.

CURRICULUM VITAE

PERSONAL INFORMATION

Surname, Name: Koçer, Hasan
Nationality: Turkish (TC)
Date and Place of Birth: 14 April 1974, Ereğli-KONYA
Marital Status: Married
Phone: +90 312 4175190-(Int. 4356)
Fax: +90 312 210 23 04
e-mail: hkocer@kho.edu.tr

EDUCATION

Degree	Institution	Year of Graduation
M.Sc.	Boğaziçi University EE Eng.	1998
B.Sc.	Boğaziçi University EE Eng.	1995

WORK EXPERIENCE

Year	Place	Enrollment
2008-Present	Turkish Military Academy	Electronics Instructor
2006-2008	Turkish Army Aviation Factory	Avionics Group Manager
1995-2006	Turkish Army Electro-Optical Systems Maintenance Center (EOSBM.Md.lüğü)	Dept. Manager of Fire Control Systems Dept. Manager of Missile Systems Dept. Manager of Electronic, Mechanical and Optical Calibration Dept. Manager of Thermal, Night Vision and Laser Systems

FOREIGN LANGUAGES

Advanced English

PUBLICATIONS

1. H. Koçer, *Kızılötesi Dedektör Teknolojileri*. Ankara: K.K.Loş.K.lğı Elektro-Optik Sistemler Bakım Merkezi Md.lüğü, Ocak 2006.
2. H. Koçer, Ö. H. Tekbaş and G. Bulu "Comparison of night vision goggles and FLIR systems in airborne applications," *Journal of Defence Sciences*, vol. 8, Number: 2, pp. 1-21, 2009.
3. H. Kocer, Y. Arslan and C. Besikci, "Numerical analysis of long wavelength infrared HgCdTe photodiodes as a design guide," *in preperation to be submitted*.

HOBBIES

Cinema, sightseeing, reading